A Phase-field Model Embedded in the Theory of Porous Media with Application to Hydraulic Fracturing

Chenyi Luo
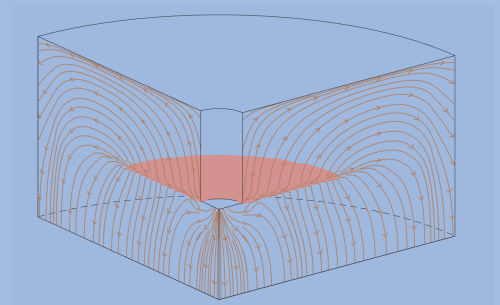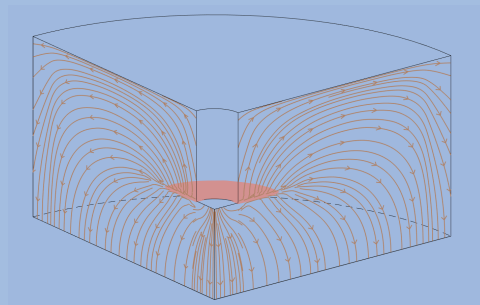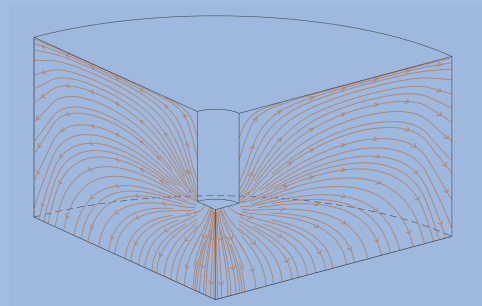
A Phase-field Model Embedded in the Theory of Porous Media with Application to Hydraulic Fracturing

Von der Fakultät Bau- und Umweltingenieurwissenschaften und
dem Stuttgart Research Centre for Simulation Technology
der Universität Stuttgart zur Erlangung der Würde
eines Doktor-Ingenieurs (Dr.-Ing.)
genehmigte Abhandlung

vorgelegt von

Chenyi Luo, M. Sc.

aus
Shanghai

Editor:
Prof. Dr.-Ing. Dr. h. c. W. Ehlers

Acknowledgements

This dissertation is based on the work done between the years 2013 and 2018 when I worked as a research associate and a PhD student at the Chair of Continuum Mechanics of the Institute of Applied Mechanics (Civil Engineering) at the University of Stuttgart in Germany. Considering this work would not be done without the support of many people, I would like to hereby express my deepest gratitude to them.

First of all, I would like to appreciate my supervisor, Professor Wolfgang Ehlers, for providing me such a challenging and meaningful project as well as sharing his vast extent of knowledge and experience. Not only his brilliant mind but the pursuit of precision and perfection always motivates me during the study. In addition, his successful leadership of the research group creates a positive and dynamic scientific atmosphere from which I have benefited.

Next, I wish to thank my officemates Dr.-Ing. David Koch, Sami Bidier and Patrick Schröder for many meaningful discussions and open-minded visions. Besides, I owe my gratitude to Dr.-Ing. Arndt Wagner, Dr.-Ing. Said Jamei, Dr.-Ing. Maik Schenke for their continuous support, particularly, their supervision at the early stage of my research. Furthermore, my appreciations also go to Dr.-Ing. Joffrey Mabuma, Dr.-Ing. Kai Häberle, Davina Fink, Lukas Böger and Alixa Sonntag for the warm and friendly working atmosphere as well as for the selfless help, either private or public.

Finally, I would like to dedicate the very special thanks to my family, especially, my parents for their unconditional love and constant encouragement, my husband, Lin, for his firm trust and boundless support which passes all tough and delightful moments, and my son, Yuanqiao, for his being my baby and lightening my life.

Stuttgart, August 2018   Chenyi Luo

Per aspera ad astra.

Through hardship to the stars.

Contents

List of Figures

List of Tables

Nomenclature

Conventions

Kernel conventions

$(\,\cdot\,)$	place holder for arbitrary quantities
$s,\ t,\ \dots$ or $\phi,\ \psi,\ \dots$	scalars (0th-order tensors)
$\mathbf{s},\ \mathbf{t},\ \dots$ or $\boldsymbol{\phi},\ \boldsymbol{\psi},\ \dots$	vectors (1th-order tensors)
$\mathbf{S},\ \mathbf{T},\ \dots$ or $\boldsymbol{\Phi},\ \boldsymbol{\Psi},\ \dots$	2th-order tensors, exception for $\mathbf{X}$ denoting the referential position vector, $\mathrm{d}\mathbf{A}$ representing a referential area element, $\mathrm{d}K^{\alpha}$ expressing the constituent force element in the referential configuration
$\overset{N}{\mathbf{S}},\ \overset{N}{\mathbf{T}},\ \dots$ or $\overset{N}{\boldsymbol{\Phi}},\ \overset{N}{\boldsymbol{\Psi}},\ \dots$	N^{th}-order tensors

Index and suffix conventions

$i,\ j,\ k,\ l,\ \dots$	indices as super- or subscripts ranging from 1 to N, where $N = 3$ in the usual three-dimensional space of our physical experience
$(\,\cdot\,)_k(\,\cdot\,)^k = \sum_k (\,\cdot\,)_k(\,\cdot\,)^k$	*Einstein*'s summation convention yields a summation over indices that appear twice unless stated otherwise
$(\,\cdot\,)_S,\ (\,\cdot\,)_F$	capital subscripts indicate kinematical quantities of a constituent within porous–media or mixture theories
$(\,\cdot\,)^S,\ (\,\cdot\,)^F$	capital superscripts indicate non-kinematical quantities of a constituent within porous–media or mixture theories
$(\,\cdot\,)_0^{(\cdot)}$	initial value of a non kinematical quantity
$(\,\cdot\,)_{0S}^{(\cdot)}$	initial value of a non kinematical quantity with respect to the referential configuration of the solid
$(\,\cdot\,)_\alpha'$	material time derivative following the motion of a constituent α with the solid and fluid constituents $\alpha = \{S,\ F\}$
$(\,\cdot\,)^{\alpha R}$	effective or real non-kinematical quantity of a constituent α
$\mathrm{d}(\,\cdot\,)$	differential operator

$\partial(\,\cdot\,)$	partial differential operator
$(\,\cdot\,)^T$, $(\,\cdot\,)^{-1}$	transposed and inverse forms of a tensor
$(\,\cdot\,)^{-T}/(\,\cdot\,)^{T-1}$	inverse of a transposed tensor
$\delta(\,\cdot\,)$	test function of the respective degrees of freedom
$(\,\cdot\,)^h$	spatially discretised quantity
$(\,\cdot\,)_{t_n}$, $(\,\cdot\,)_{t_{n+1}}$	temporally discretised quantities in time steps n and $n+1$
$(\,\cdot\,)^{i_m}$, $(\,\cdot\,)^{i_{m+1}}$	quantities in iteration steps m and $m+1$

Symbols

Greek letters

Symbol	Unit	Description
α	-	constituent identifier in super- and subscript $\alpha = \{S,\, F\}$
δ_i^j, δ_{ij}	-	*Kronecker* symbol or *Kronecker* delta
ϵ	m	length-scale parameter measuring the smeared crack width
ε, ε^α	J/kg	mass-specific internal energies of φ and φ^α in Chapter 2, linearised strain in Section 3.5
$\hat{\varepsilon}^\alpha$	J/(m^3 s)	volume-specific direct energy production term of φ^α
η, η^α	J/(K kg)	mass-specific entropies of φ and φ^α
η_r	-	residual stiffness coefficient
$\hat{\eta}$, $\hat{\eta}^\alpha$	J/(K m^3 s)	volume-specific total entropy production terms of φ and φ^α
θ, θ^α	K	absolute temperatures of φ and φ^α
λ^S	N/m^2	2$^{\text{nd}}$ *Lamé* constant of φ^S
λ_{Si}	-	eigenvalue of the linearised solid strain

Λ	-	constant of the solution for an ordinary different equation
μ^{FR}	N s/m^2	effective dynamic fluid viscosity
μ^S	N/m^2	1$^{\text{st}}$ *Lamé* constant of ϕ^S
ρ	kg/m^3	density of the overall aggregate φ
ρ^α, $\rho^{\alpha R}$	kg/m^3	partial and effective (real) densities of φ^α
ρ_0^α	kg/m^3	initial partial density
$\hat{\rho}^\alpha$	kg/(m^3 s)	volume-specific mass production of φ^α
σ, σ^α, $\boldsymbol{\sigma}$, $\boldsymbol{\sigma}^\alpha$	TBD	scalar- and vector-valued supply terms of thermomechanical quantities for φ and φ^α
σ_c	N/m^2	critical stress
σ_η, σ_η^α	J/(K m^3 s)	volume-specific external entropy supply terms of φ and φ^α
φ, φ^α	-	overall aggregate model and specific constituent α
$\boldsymbol{\phi}_{geo}^j$, $\boldsymbol{\phi}^j$	-	global basis functions
ψ, ψ^α	J/kg	mass-specific *Helmholtz* free energies of φ^α
$\psi^{S\pm}$	J/kg	mass-specific tensile/compression energies of the solid
ψ_0	J/kg	linearised elastic stored energy
ψ_c	J/kg	critical energy
Ψ, $\boldsymbol{\Psi}$, Ψ^α, $\boldsymbol{\Psi}^\alpha$	TBD	volume-specific densities of scalar and vectorial thermomechanical quantities for φ and φ^α
$\hat{\Psi}$, $\hat{\boldsymbol{\Psi}}$, $\hat{\Psi}^\alpha$, $\hat{\boldsymbol{\Psi}}^\alpha$	TBD	volume-specific production terms of scalar and vectorial thermomechanical quantities for φ and φ^α
Ω, $\partial\Omega$	-	spatial domain and boundary of the aggregate body $\mathcal{B}$
Ω_e, Ω^h	-	a finite element and the discretised finite-element domain
Ω_e^ξ	-	a reference finite element described in local coordinates
$\boldsymbol{\xi}$	-	local coordinates of a reference element
ϕ, ϕ^S	-	phase variable and solid phase variable
$\boldsymbol{\phi}$, $\boldsymbol{\phi}^\alpha$, $\boldsymbol{\Phi}$, $\boldsymbol{\Phi}^\alpha$	TBD	general vector- and tensor-valued thermomechanical quantities for φ and φ^α in Chapter 2
$\boldsymbol{\phi}_\eta$, $\boldsymbol{\phi}_\eta^\alpha$	J/(m^2 K)	entropy efflux terms for φ and φ^α
$\boldsymbol{\chi}_\alpha$, $\boldsymbol{\chi}_\alpha^{-1}$	m	motion and inverse motion function of the constituent φ^α

$\boldsymbol{\varepsilon}_S$	-	linearised contravariant *Green-Lagrange*an solid strain tensor
$\boldsymbol{\varepsilon}_S^{\pm}$	-	linearised solid strain tensor containing only the positive/negative eigenvalues
$\boldsymbol{\sigma}^S$	N/m^2	linearised stress tensor of φ^S
σ_c	N/m^2	critical stress
$\boldsymbol{\tau}^{\alpha}$	N/m^2	*Kirchhoff* stress tensor of φ^{α}
γ_s	J/m^2	surface energy per unit surface area
γ^{FR}	N/m^3	effect unit weight of the fluid
π	-	a mathematical constant defined as the ratio of a circle's circumference to its diameter
Γ	-	surface, boundary condition
Γ^S	/m	fracture energy of the solid per critical energy release rate, boundary conditions in Section 5.2
Υ_t^S	J/m^2	solid triggering strain energy

Latin letters

Symbol	Unit	Description
$\mathbf{a}_{\alpha}$	m/s^2	acceleration vector of φ^{α}, $\mathbf{a}_{\alpha} = \overset{\prime\prime}{\mathbf{v}}_{\alpha}$
$\mathbf{A}_{\alpha}$	-	contravariant *Almansi*an strain tensor of φ^{α}
$\mathbf{b}$, $\mathbf{b}^{\alpha}$	m/s^2	mass-specific body force vectors for φ and φ^{α}
$\mathbf{B}_{\alpha}$	-	covariant left *Cauchy-Green* deformation tensor of φ^{α}
$\overset{4}{\mathbf{B}}_S$	N/m^2	consistent tangent tensor of the solid
$\mathbf{C}_{\alpha}$	-	contravariant right *Cauchy-Green* deformation tensor of φ^{α}
$\overset{4}{\mathbf{C}}$	N/m^2	linearised elastic stiffness tensor
$\mathbf{d}_{\alpha}$	m/s	diffusion/barycentric velocity vector of φ^{α}
d$\mathbf{a}$	m^2	oriented current area element
d$\mathbf{A}_{\alpha}$	m^2	oriented reference area element of φ^{α}
d$\mathbf{k}_{\alpha}$, d$\mathbf{K}_{\alpha}$	N/m^2	traction force elements in the current and referential configurations

$\mathrm{d}m^\alpha$	kg/m^3	local mass element of φ^α
$\mathrm{d}v$, $\mathrm{d}v^\alpha$	m^3	current volume elements of φ and φ^α
$\mathrm{d}V_\alpha$	m^3	volume element of the aggregate at the referential position of φ^α
$\mathrm{d}\mathbf{x}$	m	current line element
$\mathrm{d}\mathbf{X}_S$	m	reference line element of the solid
d	-	damage variable in Section 3.5, spatial dimension of the physical problem for other else
$\mathbf{D}_\alpha$	·/s	symmetric deformation velocity tensor of φ^α
$\hat{e}^\alpha$	J/(m^3 s)	volume-specific total energy production of φ^α
E	-	number of non-overlapping finite elements Ω_e in Chapter 5, *Young*'s modulus for other else
E'	N/m^2	Young's modulus for plane-strain cases
E^*	-	finite element attached to a respective node P^j
E_b	J	bond energy
$\mathbf{e}_i$	-	basis vector of a Cartesian coordinate system
$\mathbf{E}_\alpha$	-	contravariant *Green-Lagrange*an strain tensor of φ^α
f	TBD	function identifier or integration constant
$\bar{f}$	N	inter-atomic force between two atoms
f_c	N	maximum tensile force between two atoms
$\mathbf{F}_\alpha$	-	material deformation gradient of φ^α
g	-	degrading function of a phase-field model
g	m/s^2	scalar value of the gravitational force vector
$\mathbf{g}$	m/s^2	gravitational force vector
G_c	N/m	critical energy release rate
$\overset{4}{\mathbf{G}}{}^\pm$	-	positive/negative mapping tensor between the solid positive/negative strain and the solid linearised strain
I_{Si}	-	principal invariant of the linearised solid strain
$\hat{h}^\alpha$	N/m^2	volume-specific total angular momentum production of φ^α
$\mathbf{I}$	-	identity tensor (2$^\text{nd}$-order fundamental tensor)
J	J/m	J-integral
J_α, J_e	-	*Jacobi*an determinants of φ^α and of a reference element Ω_e^ξ

k	N/m	stiffness of a bond between two atoms
k^F	m/s	hydraulic conductivity
K^S	m^2	intrinsic permeability of the solid
K_G	-	integration point for the *Gauss*ian quadrature scheme
K_I, K_{II}, K_{III}	-	Stress Intensity Factors for Mode I, II and III
$\mathbf{L}_\alpha$	·/s	spatial velocity gradient of φ^α
m^α	kg	mass of φ^α
$\hat{\mathbf{m}}^\alpha$	N/m^2	volume-specific direct angular momentum production of φ^α
M	Pa/s	mobility parameter
$\mathbf{M}_{Si}$	-	eigentensors of the linearised solid strain
n^α	-	volume fraction of φ^α
n^F, n^S	-	porosity and solidity
$\mathbf{n}$	-	outward-oriented unit surface normal vector
$\mathbf{n}_{Si}$	-	eigenvector of the linearised solid strain
N, N_e	-	numbers of nodal points for Ω^h and Ω_e
N_b	/m^2	number of bonds per unit area
p	N/m^2	pore pressure
$\hat{\mathbf{p}}^\alpha$	N/m^3	volume-specific direct momentum production of φ^α
P^j	-	nodal point in a finite element Ω_e of the set $\mathcal{N}$
$\mathbf{P}^\alpha$	N/m^2	1$^{\text{st}}$ *Piola-Kirchhoff* stress tensor of φ^α
$Q_\mathcal{V}$	-	basis function for primary variables
r, r^α	J/(kg s)	mass-specific external heat supply terms of φ and φ^α
$\hat{\mathbf{s}}^\alpha$	N/m^3	volume-specific total momentum production of φ^α
s	-/m	second (unit of time), in Section 3.3 denoting the half size of a sharp crack
$\mathbf{S}^\alpha$	N/m^2	2$^{\text{nd}}$ *Piola-Kirchhoff* stress tensor of φ^α
t	s	time
t_0	s	$t = 0$
$\mathbf{t}$	N/m^2	traction force per unit surface
$\mathbf{t}_E^\alpha$	N/m^2	effective traction force of φ^α per unit surface

Symbol	Unit	Description
$\mathbf{T}$, $\mathbf{T}^\alpha$	N/m^2	overall and partial *Cauchy* (true) stress tensors of φ and φ^α
$\mathbf{u}_S$	m	solid displacement vector
U	J	total energy
U_{int}, U_{ext}, U_Γ	J	internal, external and surface energies
$\bar{v}$	m/s	fluid volume efflux
v^{ϕ^S}	/m	phase-variable efflux
$\mathbf{v}_\alpha$	m/s	velocity vector of φ^α, $\mathbf{v}_\alpha = \overset{'}{\mathbf{x}}_\alpha$
V, V^α	m^3	overall volume of $\mathcal{B}$ and partial volume of $\mathcal{B}^\alpha$
w	J/m^3	strain energy density
w_k	-	weight for the *Gauss*ian quadrature scheme
$\mathbf{w}_F$	m/s	seepage velocity
x_i	-	global coordinate
$\mathbf{x}$	m	current position vector of φ
$\dot{\mathbf{x}}$, $\overset{'}{\mathbf{x}}_\alpha$	m/s	velocity vectors of φ and φ^α
$\ddot{\mathbf{x}}$, $\overset{''}{\mathbf{x}}_\alpha$	m/s^2	acceleration vectors of φ and φ^α
$\mathbf{X}_\alpha$	m	reference position vector of φ^α

Calligraphic letters

Symbol	Description
$\mathcal{A}^\mathcal{V}$	ansatz (trial) function of the primary variables
$\mathcal{B}$, $\mathcal{B}^\alpha$	aggregate body and partial constituent body
$D\boldsymbol{\mathcal{F}}^k_{n+1}$	global residual tangent
$\boldsymbol{\mathcal{F}}$	vector containing the global and local system of equations
$\mathcal{G}_\mathcal{V}$	weak formulation of a governing equation related to a primary variable
$\boldsymbol{\mathcal{G}}_\mathcal{V}$	abstract vector containing the weak formulations
$\mathcal{H}^1(\Omega)$	*Sobolev* space
$\mathcal{I}$	Crack-Opening Indicator

$\mathcal{K}$	generalised stiffness matrix
$\boldsymbol{\mathcal{M}}$	generalised mass matrix
$\mathcal{N}$	set of all nodes for the FE discretisation
$\mathcal{O}$	higher-order terms in *Taylor*'s expansion
$\mathcal{P}, \mathcal{P}^\alpha$	material points of φ and φ^α
$\mathcal{R}$	set of response functions
$\boldsymbol{\mathcal{R}}$	generalised residual vector
$\mathcal{S}, \mathcal{S}^\alpha$	surfaces of the aggregate and constituent body
$\mathcal{T}^{\mathcal{V}}$	test (weighting) functions of the primary variables
$\mathcal{V}$	set of independent process variables
$\mathcal{V}_S$	subset of independent process variables
$\boldsymbol{y}$	abstract vector containing all nodal DOF

Selected acronyms

Symbol	Description
2-d	two-dimensional
3-d	three-dimensional
COI	Crack-Opening Indicator
DOF	degrees of freedom
FE-software	Finite-Element software
FEA	Finite-Element Analysis
FEM	Finite-Element Method
IBVP	initial boundary value problem
PANDAS	**P**orous media **A**daptive **N**onlinear finite-element solver based on **D**ifferential **A**lgebraic **S**ystem
PDE	partial differential equation
REV	representative elementary volume
SIF	Stress Intensity Factor

TBD	to be defined
TPM	Theory of Porous Media
XFEM	extended Finite-Element Method

Zusammenfassung

Hydraulic Fracturing, auch Fracking genannt, ist eine weit verbreitete Stimulationstechnologie in der Energiewirtschaft. Während des Prozesses wird eine Frackingflüssigkeit unter hohem Druck in eine Schicht mit geringer Permeabilität, wie beispielsweise Schiefer, gepresst. Dies erzeugt ein Vielzahl von Rissen, welche sich in diesem Bereich ausbreiten. Diese künstlich erzeugten Risse tragen zur Verbesserung der Permeabilität der Schicht bei und erhöhen dadurch die Öl- oder Gasproduktion signifikant. Trotz des offensichtlichen wirtschaftlichen Nutzens kann das hydraulische Fracturing auch schwerwiegende Umweltprobleme, wie die Instabilität der Schicht und die Verschmutzung des Wassers, mit sich bringen. Daher ist es erforderlich, den Fracking-Prozess zu verstehen und das potenzielle Risiko zu evaluieren. Es ist allgemein bekannt, dass das hydraulische Fracturing ein multiphysikalischer Prozess ist. Daher muss die Forschung mindestens zwei Hauptphänomene umfassen, nämlich den Riss des Festkörpers durch Fluidinjektion sowie die Kopplung zwischen dem Festkörper und dem Fluid.

Ziel der vorliegenden Monographie ist es, ein kontinuumsmechanisch basiertes, thermodynamisch konsistentes, dynamisches Zweikomponentenmodell durch Einbettung des Phasenfeldmodells in die Theorie Poröser Medien vorzuschlagen.

Zur Beschreibung von Bruchvorgängen ist die Phasenfeldmodellierung ein vielversprechender Ansatz, der seit zwanzig Jahren auf reine Feststoffe angewendet wird. Diese Methode hat sich als sehr brauchbar erwiesen, nicht nur wegen ihrer Einfachheit in der numerischen Implementierung, sondern auch wegen ihrer Fähigkeit, dreidimensionale Probleme zu bewältigen. Sie kann auch komplexe Rissbildungsphänomene, wie Rissverzweigung, ohne zusätzliche Behandlung simulieren. Hinsichtlich der Modellierung von mehrphasigen Materialien im Hinblick auf flüßigkeitsgesättigte porösen Feststoffe hat sich die Theorie Poröser Medien als ausgezeicheneter Modellansatz erwiesen. Die Einführung von Produktionstermen in die Bilanzgleichungen ermöglicht eine Beschreibung der Kopplung zwischen den Konstituierenden. Dadurch wird die Darstellung eines durch Fluiddruck initiierten Risses ermöglicht.

Das vorgeschlagene Modell basiert auf der Theorie Poröser Medien. Die notwendigen Restriktionen zur Herleitung der konstitutiven Gleichungen des Zweiphasenmaterials (Festkörper und Flüssigkeit) werden für isotherme Prozesse aus der *Clausius-Planck*-Ungleichung hergeleitet. Bevor thermodynamisch konsistente konstitutive Gleichungen vorgeschlagen werden, werden einige Merkmale des Fracking-Prozesses diskutiert.

Diesbezüglich sollte die freie Energie vom Festkörperskelett nicht nur von der Festkörperdeformation abhängen, sodern auch von einer Variablen, die den Zustand des Festkörpers im Hinblick auf das Risswachstum kennzeichnet. Diese Zustandsgröße (häufiger als Phasenvariable oder Order-parameter bezeichnet) kann den Einfluss beschreiben, der durch Risse eingeführt wird. Außerdem wird angenommen, dass die freie Energie des Festkörperskeletts von dem Gradienten dieser Phasenvariablen abhängig ist. Dieser Gradiententerm reguliert die Festkörperenergie und beseitigt den Größeneffekt, wenn die Materialparameter und die Elementgröße richtig gewählt werden.

Die Phasenvariable ϕ^S für den Festkörper ist durch zwei Grenzzustände (intakt und vollständig gebrochen) begrenzt. Normalerweise entwickelt sich diese Variable monoton von einem intakten Material ($\phi^S = 0$) zu einem vollständig gebrochenen ($\phi^S = 1$) Material. Dies beruht auf den Beobachtungen, dass sich Bodenmaterial wie Schiefer normalerweise nicht selbst heilt oder selbst versiegelt. Um diese Monotonie während der numerischen Behandlung einzubeziehen, wird in die Evolutionsgleichung eine History-Variable für einen robusten Algorithmus eingefügt. Diese Variable zeichnet den maximalen Wert der erreichten spannungsinduzierten Festkörperenergie auf.

Weiterhin hängt die Entwicklung dieser Phasenvariablen für einen druckgetriebenen Riss nur von der Akkumulation der Verzerrungsenergie des Festkörpers ab, nicht jedoch vom Fluiddruck. Dies liegt an der Tatsache, dass der Fluiddruck als äußere Belastung dient, die eine Festkörperverformung durch die Kopplung der Impulsproduktionsextragröße verursacht. Dies erhöht die Festkörperenergie und löst schließlich einen Riss aus. In diesem Sinne wurde der Einfluss des Fluiddrucks bereits durch die resultierende Festköperverformung und die Verzerrungsenergie des Festkörpers berücksichtigt.

Letzlich ist die Rissinitiierung und -ausbreitung ein Ergebnis von Zugspannung, jedoch nicht von Kompression. In dieser Hinsicht wird in dieser Monographie die spektrale Zerlegung der Festkörperdeformation und der entsprechenden Energie übernommen, vgl. Miehe et al. [155]. Diese Energie unterscheidet die Anteile, die durch die positiven Hauptverzerrrung und die negativen Hauptverzerrung verursacht werden. Der erste Anteil nimmt mit der Entwicklung der Phasenvariable ab, während die zweite konstant bleibt.

Diese Merkmale berücksichtigend wird eine geeignete Form für die von Miehe et al. [155] inspirierte freie Energie für das Festkörperskelett vorgeschlagen. Basierend auf dieser Form verringert die Entwicklung der Phasenvariablen die Spannungsenergie vom Festkörper, während die Oberflächenenergie erhöht wird. Darüber hinaus hat sich seine Anwendung auf Festkörper in einem quasi-statischen Zustand als konsistent mit der klassischen Griffith-Theorie erwiesen, wenn der Längenparameter den Grenzwert 0 erreicht.

Wenn ein durch einen Riss induzierter flüssigkeitsgefüllter Raum entsteht, wird dort die Kopplung zwischen dem Feststoff und dem Fluid aufgrund des Fehlens des Feststoffs und des entsprechenden Widerstands nicht länger dominieren. In dieser Hinsicht wird die konstitutive Gleichung der Impulsproduktionsextragröße des Fluids so vorgeschlagen, dass die Entwicklung der Phasenvariablen diese Produktion verringert. Darüber hinaus machen sich die Fluidextraspannungen bemerkbar und in einem Grenzfall (vollständig gebrochen) sind sie den Newtonschen Viskositätsspannungen gleich. Die spontanen Umwandlungen der Fluidimpulsproduktionsextragröße und der Fluidextraspannung führen dazu, dass der Flüssigkeitsdynamikausgleich von Darcyschem Gesetz in die Navier-Stokes-Gleichung umgewandelt wird. Somit ist das vorliegende Modell in der Lage, einen Druckriss und eine daraus folgende Zustandsänderung der Flüssigkeit zu simulieren.

Eine weitere wichtige Tatsache ist, dass die Schicht normalerweise unvollkommen ist und somit einige natürliche Risse vorhanden sind, bevor der hydraulische Frakturierungsprozess beginnt. In früheren Experimenten wurde bereits festgestellt, dass diese natürlich vorkommenden Risse die Ausbreitung der hydraulischen Risse beeinflussen. Wenn zum Beispiel unterschiedliche Druckspannungen angewendet werden, variieren die Muster des hydraulischen Bruches in Bezug auf die bereits existierenden Risse, die geschlossen bleiben

oder sich öffnen. Die vordefinierte Phasenvariable kann jedoch nur die Erzeugung von Rissen aufzeichnen. Darüber hinaus ändert die Phasenvariable den Flusstyp der Flüssigkeit monoton, allerdings können diese Risse unter den Druckspannungen wieder geschlossen werden. Im Genaueren folgt der Flüssigkeitsfluss in einem offenem Riss der Navier-Stokes-Gleichung, wohingegen der Fluss in einem wieder geschlossenem Riss durch eine Darcy-Stimmung bestimmt wird. Diese bidirektionale Transformation des Strömungstyps inspiriert ein neues Konzept, den Crack-Opening-Indicator, der die Möglichkeit einer Rissöffnung definiert. Durch die Kombination des Crack-Opening-Indicators und der Phasenvariablen können vier extremale Zustände poröser Materialien unterschieden werden, nämlich intaktes Material mit zunehmender / abnehmender Porosität und vollständig gebrochenes Material mit einem geschlossenen / offenen Riss. Nur wenn das Material vollständig gebrochen ist und der Riss sich öffnet, folgt die Flüssigkeit der Navier-Stokes-Gleichung. Für die übrigen Fälle ist der Fluss vom Darcy-Typ.

Schließlich werden mehrere numerische Beispiele durch das Finite-Elemente Programm PANDAS ausgeführt, um die Einsatzmöglichkeiten des entwickelten Modells zu präsentieren. Das erste Beispiel untersucht das Geschwindigkeitsprofil der Flüssigkeit im intakten und vollständig gebrochenen Bereich. Die Ergebnisse zeigen, dass die Strömung im intakten Bereich dem Darcy-Gesetz folgt, während sich die Flüssigkeit im offenen Rissbereich als Poiseuille-Fluss mit einer Gleitgeschwindigkeit auf der Rissoberfläche bewegt. Dieses Ergebnis stimmt mit der analytischen Lösung von Beavers & Joseph [18] überein. Das entwickelte Modell erweist sich somit als in der Lage, zwei Zustände des Strömungstyps zu beschreiben, einen Darcy-Typ im intakten Bereich und einen Navier-Stokes-Typ im vollständig gebrochenen Bereich. Das zweite Beispiel demonstriert die Leistung des entwickelten Modells bei der Simulation eines unter Druck stehenden Risses im zweidimensionalen Raum. Das dritte Beispiel konzentriert sich auf den hydraulischen Frakturierungsprozess mit zwei vorher existierenden Rissen unterschiedlicher Richtungen unter verschiedenen Einspannungen. In den numerischen Ergebnissen neigt der neu erzeugte Riss dazu, den vorher existierende Riss zu kreuzen, wenn die Druckspannung hoch genug ist um den vorher existierende Riss aufrechtzuerhalten. Andernfalls wird der neue in den vorher existierende Riss eingefügt. Diese Beobachtung wird auch im Experiment von Blanton [24] festgestellt. Im vierten Beispiel wird der hydraulische Bruchprozess in einer dreidimensionalen Umgebung mit dem entwickelten Modell simuliert, was die mögliche Anwendung des Modells auf realistische Probleme nahelegt.

Abstract

Hydraulic fracturing, also known as fracking, is a widely used stimulation technology in the energy industry. During the process, a fracking fluid is pressed under high pressure into a low-permeable stratum, for example, shale. A large number of cracks are then triggered and further propagate in that region. These artificially generated cracks improve the permeability of the stratum and as a result, dramatically increase oil or gas production. Despite the apparent economic benefit, hydraulic fracturing might also bring severe environmental problems such as the instability of the stratum and water contamination. Hence, it is desired to recognise the fracking process and assess the potential risk. As hydraulic fracturing is a multiphysics process, the ad-hoc research must deal with, at least, two main phenomena, namely the cracking of the solid driven by fluid injection and the coupling between the solid and the fluid.

The aim of this monograph is to develop a continuum-mechanics based, thermodynamically consistent, dynamic, two-component model by embedding the phase-field model into the Theory of Porous Media. The phase-field model has been proven to be a promising approach in tackling fracture problems of pure solids after almost thirty years of study. This method is very competitive not only because of its simplicity in numerical implementation but also due to its ability of handling three-dimensional problems without the need of predicting all possible crack modes in advance. Besides, it is able to simulate complex fracture phenomena such as crack branching. With regard to the modelling of multiphasic materials such as liquid-filled porous solids, the Theory of Porous Media (TPM) provides a systematic, general and rational framework. In particular, the TPM introduces production terms into the balance equations and hence allows the description of the coupling between the constituents, which further makes it feasible to depict a pressurised crack.

The integration of the phase-filed approach into the TPM framework starts with the basic setting and definitions of the TPM and proceeds with the reformulation of the *Clausius-Planck* inequality for an isothermal process. The sufficient conditions of the constitutive equations can then be derived by evaluating this inequality. Before appropriate constitutive equations are proposed, several features regarding the fracking process in saturated porous media are discussed as follows.

Firstly the solid *Helmholtz* free energy should depend not only on the solid strain but also on a variable denoting the state of the solid. This state variable (more often called phase variable or order parameter) is able to describe the influence introduced by fracture. Furthermore, this energy is assumed to be dependent on the gradient of that state variable. This gradient-type term regularises the solid energy and eliminates the size effect when the material parameters and the mesh size are properly chosen.

Secondly the phase variable ϕ^S is defined for the solid, which is bounded by two limit states (intact and fully broken). Usually, this variable evolves monotonically from an intact material (denoted by 0) to a fully broken one (denoted by 1). This is based on the observation that soil, like shale, usually does not self-heal or self-seal. In order to include this monotonic crack growth into the numerical treatment, a history variable is introduced

in the evolution equation for a robust algorithm. This variable records the maximum value of the tension-induced solid strain energy that has been achieved historically.

Thirdly, for a pressure-driven crack, the evolution of this phase variable only depends on the accumulation of the solid strain energy but not on the fluid pressure. This is owing to the fact that the fluid pressure serves as an external loading, causes the solid deformation by the coupling momentum production, increases the solid strain energy and finally triggers a crack. In this sense, the influence of the fluid pressure has already been accounted for by the resulting solid deformation and the solid strain energy.

Fourthly, the crack initiation and propagation is a result of tension but not of compression. In this regards, the monograph adopts the spectral decomposition of the solid strain and the corresponding solid strain energy, cf. Miehe et al. [155]. This energy distinguishes the energy caused by the positive principal strains and the negative principal strains. The first term decreases with the evolution of the phase variable while the second one stays constant.

After noticing these features, a proper form for the solid free energy inspired by Miehe et al. [155] is suggested. Based on this form, the evolution of the phase variable reduces the solid strain energy, while the surface energy increases. Furthermore, its application on pure solids has been proven consistency to the classical Griffith theory in a quasi-static state when the length-scale parameter approaches the limit value 0.

If there is a purely fluid-filled space induced by a crack, the coupling between the solid and the fluid will no longer be dominant there because of the absence of the solid and the corresponding resistance. In this regard, the constitutive equation of the fluid extra momentum production is proposed in such a way that the evolution of the phase variable will decrease this production. Moreover, the fluid extra stresses become apparent and in a limit case (fully broken) equal to the Newtonian viscous stresses. The spontaneous transformations of the fluid extra momentum production and the stresses result in the fluid momentum balance being converted from Darcy's Law to the Navier-Stokes equation. Thus, the present model is able to simulate a pressurised crack and the spontaneous state change of the fluid.

Another crucial fact is that the stratum is usually imperfect and some natural cracks exist before the hydraulic fracturing process starts. Previous experiments have already discovered the influence of these pre-existing cracks on the propagation of the hydraulic cracks. For example, when different confining stresses are applied, the pattern of the hydraulic fracture varies regarding the pre-existing cracks keep closed or start to open. However, the predefined phase variable is only able to record the generation of cracks. Moreover, it changes the flow type of the fluid monotonically as well, though these cracks might be closed again under the confining stresses. And when the fluid flows through a re-closed crack, it obeys Darcy's Law again. This bi-directional transformation of the flow type inspires a new concept, the Crack-Opening-Indicator, which defines the possibility of a crack opening. The combination of the Crack-Opening-Indicator and the phase variable makes it possible to distinguish four limit states of porous materials, namely intact material with increasing/decreasing porosity and broken material with a close/open crack. Only when the material is broken and the crack is opening, the fluid flow is governed by the Navier-Stokes equation. For the other cases, the flow is of the Darcy type.

At last, several canonical numerical examples are set up to demonstrate the performance of the established model. The first example examines the velocity profile of the flow in the unbroken and fully broken regions. The results confirm that the flow in the unbroken region obeys Darcy's law while the fluid in the open crack region moves as a Poiseuille flow with a slippery velocity on the crack surface. The result of the flow in an open crack is consistent to the analytical solution of Beavers & Joseph [18]. Thus, the proposed model proves to be capable of describing two states of the flow type, the Darcy type in the unbroken regions and the Navier-Stokes type in the fully broken regions. The second example demonstrates the performance of the proposed model in simulating a pressurised crack in a two-dimensional setting. The third example focuses on the hydraulic fracturing process with two pre-existing cracks with different directions under different confining stresses. The numerical results show that the hydraulic fracture tends to cross the pre-existing crack when the confining stress is high enough to keep the pre-existing crack closed. Otherwise, the hydraulic fracture is arrested by the pre-existing cracks. These two different propagation patterns of the hydraulic fracture in the presence of the pre-existing cracks were experimentally found by Blanton [24]. In the fourth example, the hydraulic fracture process is simulated in a three-dimensional setting using the developed model, suggesting the potential application of the model to large-scale realistic problems.

Chapter 1:
Introduction and overview

1.1 Motivation

Hydraulic fracturing, also shortened by "fracking", is a widely used stimulation technique in the oil and gas industry. In particular, it helps to dramatically increase the yield of shale gas, which exists in a low-permeable stratum and hardly flows in a natural state. In a hydraulic fracturing process, a number of fissures are generated by injecting a pressurised fracking fluid, cf. Figure 1.1, resulting in a much higher permeability and, finally, adequate outflow rates. This technique has also been applied to other engineering fields, such as deep geothermal energy plants and deep groundwater resources, cf. Adachi et al. [2], Bažant et al. [17] and Hattori et al. [109]. Although it has been over seventy years since the first hydraulic fracturing experiment conducted in southwest Kansas in 1947, the assessment of the potential environmental risks, including the leakage of contaminant and destabilisation of strata, remains a challenging topic. The main challenges come from
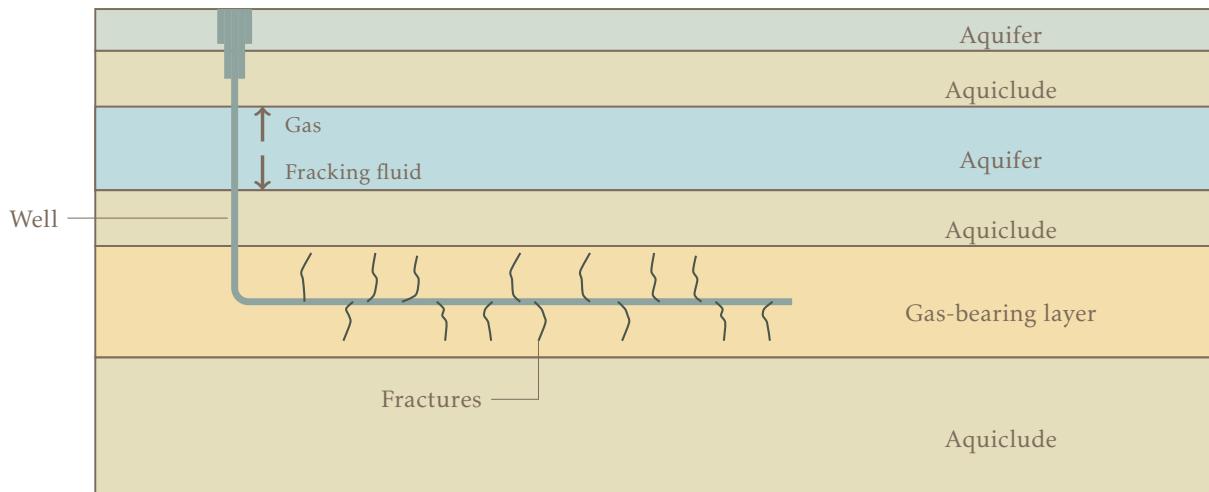
Figure 1.1: *Exemplary description of hydraulic fracturing.*

the fact that hydraulic fracturing involves at least two complex phenomena, the initiation and the propagation of cracks and the behaviour of a multi-component and multi-phasic material. Owing to a large number of experiments and the related theoretical researches, significant progress has been made in the theoretical interpretation and numerical simulation of the crack initiation and propagation. Nevertheless, the application in engineering fields requires a more efficient approach tackling complex crack patterns, such as curvilinear cracks and crack branching. Just recently, the phase-field approach has attracted intensive attention as a promising solution to crack simulations due to its simple implementation in numerics and successful applications in various fracture problems, such as

ductile fracture of solids at finite strains, cf. Aldakheel [3]. However, the fracking process usually occurs in a more complex environment including not only intact or fractured solids but also different types of fluids. Hence, special consideration has to be paid to describe such multi-component materials and the interaction therein. In this regard, Biot suggested a more or less intuitive theory, modelling the mechanical behaviour of a poroelastic medium in [22] and [23]. Despite the convenience in implementation, the initial deficiency in Biot's theory, namely the lack of individual description for the fluid, results in a further difficulty in explaining the transition from an in-pore fluid to a bulk flow and vice versa during a fracking process. In comparison, the Theory of Porous Media (TPM) proceeds from the roots of Rational Thermodynamics and provides each constituent with an individual motion function, as well as balance equations. Thus, a full description for an overall aggregate is available, where a transformation of the fluid state can also be included. Following this, the present work aims to postulate a thermodynamically consistent model in the framework of the TPM by combining it with a phase-field model to brittle fracture.

1.2   Scope, Aims and State of the Art

In the light of history, the effort of understanding and predicting the world or even the universe has never ceased. Owing to the limitation of the old-time techniques and devices, it is straightforward to assume that the material is continuous over the space, based on which the classical continuum mechanics is founded. The conventional theories of continuum mechanics homogenise the micro-structures of materials and postulate a set of axiomatic balance equations. The interested reader is referred to Chadwick [49], Gurtin [102], Haupt [110, 111], Maugin [150] and Malvern [144].

As an important failure mode in engineering and nature, the mechanism of brittle fracture has been studied for a long time, with topics ranging from the crack nucleation, initiation, propagation to crack branching, arrest and kinking. In the meantime, experimental investigations have been reported, for example, by Ravi-Chandar & Knauss [172–175], Ramulu & Kobayashi [171], and Kalthoff & Winkler [126]. However, solids like steel exhibit a large deformation before a macroscopic fracture occurs, which is then defined as ductile fracture. This transition from brittle to ductile fracture was firstly found in 1987 when Kalthoff & Winkler impacted a double pre-notched steel plate by a projectile, cf. [126] and [127]. Later on, similar experiments were conducted for a steel plate with a single notch, cf. Ravi-Chandar [176] and Zhou et al. [205–207].

The classical theory of brittle fracture in pure solids is elaborated in Griffith [96, 97], Irwin [120], and Barenblatt [14]. From an energetic point of view, Griffith suggested a surface energy which rises with the generation of the new surface induced by crack and in the meantime, absorbs the released stored energy. In addition, the crack propagation was related to a so-called critical energy release rate, which is responsible for creating new crack surfaces and governs the resistance to crack growth. If the released stored energy is greater than the increase in surface energy, the crack will propagate further. This innovative idea offers a general treatment when tackling a complex stress state around the crack tip.

Following his idea, Irwin [120] proposed the concept of the Stress Intensity Factor (SIF) instead of the critical energy release rate, which only requires the computation of the stress in the vicinity of the crack tip but not the energy of the whole system. In order to eliminate the stress singularity at the crack tip, the cohesive crack model was developed by Barenblatt [14] and Dugdale [59]. In this model, a cohesive potential is assumed by concluding the conservative stresses in the cohesive zone, cf. Gasser & Holzapfel [92]. As an extension of this approach, Rice [179] introduced the so-called J-integral which is path-independent and accounts for the energy influx into the crack tip. Besides, Eshelby [82, 83] reformulated the standard energy balance by introducing a new energy-momentum tensor, which represents a configurational force. Regarding a detailed interpretation of the configurational force applied to the crack problem, one may compare, for example, Eshelby [81–83] while Stumpf & Le [192] and Maugin & Trimarco [150] proposed a set of local formulations proceeding from the variational principle.

The aforementioned theories mainly focus on the mechanism of brittle fracture but fail to describe the behaviour of solids like steel which undergoes large irreversible (plastic) deformations around the crack tip. Irwin et al. [121] investigated the size of the crack process zone, based on which Dugdale [59] interpreted ductile fracture as macroscopic plasticity in the context of the cohesive zone model. In addition, the behaviour of ductile fracture can also be modelled by a decreasing stiffness. Following this idea, a varying crack resistance was introduced as the crack resistance curve concept in the work of Krafft et al. [133].

For the fundamentals of fracture mechanics within continuum mechanics, one may refer to Simo et al. [187], Hahn [105] and Oliver et al. [167, 168]. Additionally, an overview of the classical theories of dynamic fracture mechanics is available in Freund [91].

Although these theories explain the criterion for crack propagation, the mechanism of crack initiation in a defect-free ideal body remains unsolved. In order to overcome this drawback, one may turn to Braides [43] and Ambrosio et al. [7], who predicted the crack initiation by including additional incremental energy functionals, accounting for both volume and surface energies, in the standard variational formulation for fracture problems. Therein, the discontinuity surface was represented by a new variable, which causes singularities when computing the energy minimisation numerically. In order to regularise the derived formulation, Dal Malso [53] proposed the so-called Γ-convergence. The corresponding applications to brittle fracture can be found in, e. g. , Francfort & Marigo [88], Amor et al. [9], Bourdin [35], Dal Maso & Toader [54] and Buliga [46]. Following the idea of image segmentation by Mumford & Shah [163], Bourdin et al. [34, 36] applied Γ-convergence to the regularisation of the variational formulations. The details were further elaborated in, for example, Ambrosio & Tortorelli [6], Dal Maso [53], Braides [43, 44] and Bourdin et al. [37]. Almost contemporarily, a conceptually similar approach was applied to brittle fracture, cf. Hakim & Karma [106], Karma et al. [131] and Eastgate et al. [60]. This method was inspired by the Ginzburg-Landau theory, which phenomenologically describes the phase transition in superconductivity. A variable denoting different phases was used to distinguish the intact and fractured materials, thus leading to a phase-field model of brittle fracture, cf. Miehe et al. [155, 156] Kuhn & Müller [136], Borden et al. [33], and Schlüter et al. [185]. A review of phase-field models applied to brittle fracture

can be found in Ambati et al. [4].

Apart from the numerical regularisation, the discontinuity induced by a sharp crack can also be treated with other finite-element-based numerical methods. To name but a few, the adaptive interface element succeeds in dealing with complex three-dimensional crack scenarios, cf. Xu & Needleman [203], Camacho & Ortiz [47], Pandolfi & Ortiz [169], Geissler et al. [93], Kaliske et al. [125] and Miehe & Gürses [100, 101, 154], while the extended Finite-Element Method (XFEM), developed by Belytschko & Black [19] and Moës et al. [161], later enriched by Belytschko et al. [20] and Song & Belytschko [190], Moës & Belytschko [162] and Fagerström & Larsson [84], enhanced the standard Finite-Element Method (FEM) by introducing additional shape functions characterising newly generated cracks. Moreover, Armero & Linder [12, 140] proposed a FEM with embedded discontinuities, where a velocity-based branching criterion was suggested to simulate, especially, the branching problem.

In order to model brittle and ductile fractures simultaneously, Li et al. [139] offered a mesh-free *Galerkin* simulation regarding the failure mode transition, while Song et al. [189] enhanced the XFEM with phantom nodes. While applying the interface element, brittle fracture can be assumed dependent on the principal tensile stress, and ductile one occurs owing to the nucleation and coalescence of voids, cf. Batra & Jin [16]. In addition, an analysis of the crack growth in a double edge cracked model was reported in Needleman & Tvergaard [164].

Regarding the mutual effect between solid and fluid in a fracking process, the earliest study of multi-component and multi-phasic materials is referred to the work of Reinhard Woltman [201], who observed the significance of the volumetric portion of the soil and the water against the overall volume in a dike construction and defines this ratio as the volume fraction. However, the most famous equation does not come from him but is named after a French engineer, *Henry Philibert Gaspard Darcy*. *Darcy*'s law states that when a fluid passes through a porous solid, the velocity of the fluid is the product of the hydraulic conductivity (*Darcy* permeability) and the negative of the fluid pressure gradient. Although this relation was determined experimentally, it has been widely used in various engineering fields for its simplicity and later proved to be consistent with the *Navier-Stokes* equations after homogenisation, cf. Whitaker [200]. Another competitively significant finding, Fick's laws, was discovered by Adolf Eugen Fick, which focuses on the diffusion process in the multi-component materials, especially liquids with various solutes.

During the first several decades of the twentieth century, two theories focusing on a binary model of soil have formed with the increasing interest of geomaterials. From the perspective of an engineer, Karl von Terzaghi set up a practical theory that is, however, not continuum-mechanics-based while his opponent, Paul Fillunger, proposed an innovative model containing two interacting constituents. Regardless of a more modern basis at the very beginning, Fillunger still lost his conflict against Terzaghi, who pointed out a mistake in assuming the buoyancy force linearly dependent on the difference between the volume and surface porosity. The race ended with the suicide of Fillunger in 1937, and after fifty years, his brilliant idea again came up to the notice of Reint de Boer, who recovered his articles during the stay at Fillunger's university in Vienna in 1987. In 1956, Terzaghi's follower, Biot published his most famous work, [21–23], based on a more or less intuitive

idea. The main content has been concluded as Biot's theory and is nowadays widely used when solving porous-media problems.

A new era came in the 1950s after Truesdell presented his Theory of Mixtures, which is originated from "Rational Mechanics" [194]. In this work, he introduced "supply" terms[1] into the local balance equations for each constituent to describe the coupling mechanics between constituents while the rest of these equations were retained as the standard balance equations, cf. [195]. Besides, he proposed the metaphysical principles defining the thermodynamical requirements for arbitrary mixtures [196]. Lots of papers followed, to name but a few, Eringen and Ingram [79], Green and Naghdi [95], and Bowen [39, 40]. Extending the TPM with the concept of volume fractions, Bowen proposed two porous-media models regarding incompressible and compressible materials, respectively, in [41, 42]. For a historical review in this regard, one may compare, for example, de Boer [28] and Ehlers [72]. In addition, a detailed interpretation of the TPM, is available in, e. g. de Boer [29], de Boer & Ehlers [26, 27] and Ehlers [61–63, 68, 70] while the successful applications of the TPM have been reported in the works of Diebels & Ehlers [56], Ehlers et al. [66] and Ammann [8]. If applied to biology, the TPM is able to model biological tissues and their related medical treatment, for example, soft tissues [67], intervertebral disc [129, 130], hip joint [143], tumour growth [134] and drug infusion in the human brain [198]. According to the reports of Ehlers et al. [69], Heider [112], Avci [13], Koch [132], Schenke [184] and Häberle [104], various problems of geoconstructions such as responses to earthquake, CO_2 sequestration into deep aquifers, can also be solved in the framework of the TPM.

In order to achieve a better understanding of fracking processes, Rubin [182] studied the behaviour of hard rocks while Bohloli [30] carried out experiments on the unconsolidated soft rocks. Furthermore, experiments concerning the influence of confining stresses and natural fractures were conducted by Blanton [24], Warpinski & Teufel [197] and Zhou et al. [208]. Besides these experimental studies, the earlier theoretical investigation was usually based on very limited simple cases, cf. Rice & Cleary [180], Boone & Ingraffea [31], Boone & Detournay [32] and Detournay [55]. Thanks to the high-performance computers, more complicated and general scenarios have been under consideration. De Borst and Keschavarzi turned to the XFEM for a description of the fractured solid while Schrefler introduced a cohesive interface element. Proceeding from the successful application of the phase-field model to pure solid, some researchers attempted to combine it with Biot's theory in modelling saturated soil, cf. Bourdin et al. [38], Mikelic et al. [159, 160], Wheeler et al. [199] and Miehe et al. [157, 158]. However, owing to the missing individual fluid balance equation, the transition from an in-pore fluid to a bulk flow requires an alternative treatment, for example, a substitution by an enlarging permeability. On the other hand, researchers started from the TPM and embedded the phase variable diffusive crack, cf. Markert & Heider [113, 148] and Luo & Ehlers [141, 142]. In the work of Markert & Heider, the model was based partially on the standard form of the TPM, mainly for the balance equations, and partially on the variational formulations, mainly for the evolution of the

---

[1]The quantities, "supply" terms, are now more often called as "production" terms according to the suggestion by Ehlers [63] because the phrase, "supply" term, usually denotes a far-distance contribution of a balance equation in the framework of Continuum Mechanics.

phase variable. Furthermore, an artificial coefficient was introduced in the computation of the solid volume fraction, helping to eliminate the solid in the crack zone. Although this treatment makes the result "beautiful" in a certain sense, it does not obey the mass balance and results in an irreversible loss of weight in the crack zone. The problem becomes severe when a recycling load is applied, or natural cracks are considered. The first fully continuum-mechanical-based model dates back to the work of Ehlers & Luo [73]. This model is completely based on the TPM, where the evolution of the phase variable is re-interpreted accordingly. Recently, the second part has also been published, cf. [74], which proposed a concept of the so-called "Crack-Opening Indicator" (COI) to treat more complex crack scenarios including the confining stresses and pre-cracks.

1.3   Outline of the Thesis

Apart from the above introduction, the following content starts with a brief introduction of the fundamentals of the TPM in **Chapter 2**. Therein, the basic concept such as volume fraction, partial and real densities, together with the kinematic relations are given as a preliminary. Subsequently, the global and local balance equations are discussed, leading to the derivation of the entropy inequality which provides the necessary conditions for a thermodynamically consistent material model. Note that the conclusions within this chapter are always general and thus are valid for arbitrary porous-media problems.

In **Chapter 3**, the mechanism of crack from different scales are explained. Thereafter, several famous theories in this regard, including Griffith's theory, Irwin's theory, J-integral and the phase-field approach, are briefly reviewed. Notably, the last one is subsequently adopted as the method to tackle the crack phenomena in multi-constituent materials.

In order to simplify the derived model, **Chapter 4** focuses on a biphasic, solid-fluid material model and further applies several reasonable assumptions, for example, material incompressibility. After reformulating the balance equations and inserting them into the Clausius-Planck inequality, the inequality is divided into several parts. Before proposing constitutive equations, the idea of the COI is explained. In addition, other essential concepts such as geometrical linearisation and spectral decomposition of the solid strain are also presented. Eventually, the constitutive relations are discussed regarding the solid and the fluid, respectively.

After the theoretical interpretation, the detailed numerical treatments are presented in **Chapter 5**. At first, several critical issues related to the fracturing process itself, such as the threshold of fracturing, the irreversibility of crack generation, and the inclusion of pre-existing cracks, are discussed. Afterwards, the implementation in the framework of the Finite-Element Method is introduced. The process starts from the derivation of the governing equations in a weak form and continues with the spatial and temporal pressurised. The choice of the basic governing equations concerning the applied boundary and loading conditions is, en passant, also discussed. The last part of this chapter exhibits the derivation of the consistent tangent for convenience purposes only.

Chapter 6 displays numerical examples in two- and three dimensions. The first example aims to justify the fluid-type transition with the proposed constitutive equations while

the second one simulates the crack propagation under a pressurised load. In order to demonstrate the performance of the material model under confining stresses and pre-cracks, the third model is assumed to be under a plane-strain condition, contains two different-oriented cracks and is assigned with different combinations of confining stresses. The hydraulic fracture is triggered by injecting the fluid into one of the pre-existing cracks. The derived crack patterns are then compared to the experiments reported in Blanton [24]. The last model is set up in three dimensions and shows the capability of the model in handling higher-dimensional problems.

The thesis is summarised in **Chapter 7**. The advantages, together with the limitations of the presented numerical methodology are analysed. Moreover, an appropriate theoretical extension and potential applications are outlooked.

The essential mathematical relations of tensor calculus are outlined in **Appendix A** while essential supplements in thermodynamics are given in **Appendix B**. Furthermore, **Appendix C** gives a short introduction of the customised colour scheme in the graphics of this monograph.

Chapter 2:
Fundamentals of the Theory of Porous Media

This chapter aims to give a brief introduction to the TPM, which sets up a basic framework for the following work. The main concern includes several basic concepts of the TPM (e. g. the concept of volume balance) and balance equations (e. g. mass balance equation). The chapter is finalised with the derivation of the entropy inequality. This inequality provides the derived material model with a necessary condition for the thermodynamical consistency and will later be applied to define suitable constitutive relations for the solid and the fluid in Chapter 4.

2.1 Basic Definitions

2.1.1 Concept of volume fractions

Starting from a macroscopic scale, the TPM provides an excellent and comprehensive theory describing multi-phasic and multi-constituent materials. In this regard, a representative elementary volume (REV) is selected from the original heterogeneous material. During the homogenisation, the heterogeneity of micro-structures is neglected by a volumetric averaging process under the assumption of an ideal disarrangement state. Thus, the derived homogenised model contains a statistical substitution of the detailed inner structures, which leads to the statistical mean values of all geometrical and physical quantities. In a concerned REV, immiscible constituents, denoted by φ^α, are assumed to be superimposed in space from a macroscopical point of view, forming up the overall aggregate φ,

$$\varphi := \bigcup_\alpha \varphi^\alpha. \tag{2.1}$$

However, if looking into the microstructures, the overall volume element $\mathrm{d}v$ is composed of independent partial volume elements $\mathrm{d}v^\alpha$. The difference between macroscopical and microscopical scales requires the concept of the volume fraction, where the volume fraction n^α of a constituent φ^α is defined as

$$n^\alpha := \frac{\mathrm{d}v^\alpha}{\mathrm{d}v}. \tag{2.2}$$

If no voids exist in the REV and the whole space is occupied by constituents φ^α, then this full saturation condition enforces the constraint that

$$\sum_\alpha n^\alpha = 1. \tag{2.3}$$

If we turn back to the macroscopic scale, the overall volume V of a body $\mathcal{B}$ is defined as the sum of the partial volumes V^α of the constituent bodies B^α as

$$V := \int_{\mathcal{B}} \mathrm{d}v = \sum_\alpha V^\alpha \quad \text{with} \quad V^\alpha := \int_{\mathcal{B}^\alpha} \mathrm{d}v = \int_{\mathcal{B}} \mathrm{d}v^\alpha = \int_{\mathcal{B}} n^\alpha \mathrm{d}v. \tag{2.4}$$

Based on these volume elements, two corresponding densities are defined, namely the real density $\rho^{\alpha R}$ with respect to the local partial volume element and the partial density ρ^α with respect to the local overall volume element, as follows,

$$\rho^{\alpha R} := \frac{\mathrm{d}m^\alpha}{\mathrm{d}v^\alpha} \quad \text{and} \quad \rho^\alpha := \frac{\mathrm{d}m^\alpha}{\mathrm{d}v}, \tag{2.5}$$

where $\mathrm{d}m^\alpha$ is the local partial mass element. These two densities are related to each other via

$$\rho^\alpha = n^\alpha \rho^{\alpha R}. \tag{2.6}$$

From this equation, it is clear that the partial density depends not only on the real density (the material compressibility) but also on the volume fraction. Considering an incompressible constituent in TPM, the partial density may vary with a changing volume fraction while its real density remains constant. In correspondence to (2.4), the overall density is defined as

$$\rho := \sum_\alpha \frac{\mathrm{d}m^\alpha}{\mathrm{d}v} = \sum_\alpha n^\alpha \rho^{\alpha R}. \tag{2.7}$$

2.1.2   Motion functions

Although the REV is simultaneously occupied by constituents φ^α at a moment t at position $\mathbf{x}$, each constituent may proceed from a different reference position $\mathbf{X}_\alpha$. Thus, the independent motion functions $\boldsymbol{\chi}_\alpha$ are required to trace the movement of the material particles,

$$\mathbf{x} = \boldsymbol{\chi}_\alpha(\mathbf{X}_\alpha, t). \tag{2.8}$$

Moreover, the motion should be uniquely invertible from its physical nature, which yields non-singular functional derivatives (*Jacobi*an[1]) J_α in a mathematical manner,

$$\mathbf{X}_\alpha = \boldsymbol{\chi}_\alpha^{-1}(\mathbf{x}, t) \quad \text{with} \quad J_\alpha := \det \frac{\partial \mathbf{x}}{\partial \mathbf{X}_\alpha} \neq 0. \tag{2.9}$$

Notice that $\mathbf{x}$ and $\mathbf{X}_\alpha$ claim the positions of the material point P^α in the current (spatial) and reference (material) configurations, respectively. Other kinematical quantities related to this material point can also be expressed in these two settings. For example, in the reference configuration, the definition of the velocity and acceleration functions for the constituents φ^α can be given as follows

$$\overset{\prime}{\mathbf{x}}_\alpha = \mathbf{v}_\alpha := \frac{\mathrm{d}}{\mathrm{d}t} \boldsymbol{\chi}_\alpha(\mathbf{X}_\alpha, t) \quad \text{and} \quad \overset{\prime\prime}{\mathbf{x}}_\alpha = (\mathbf{v}_\alpha)_\alpha' = \mathbf{a}_\alpha := \frac{\mathrm{d}^2}{\mathrm{d}t^2} \boldsymbol{\chi}_\alpha(\mathbf{X}_\alpha, t). \tag{2.10}$$

---

[1] *Carl Gustav Jacob Jacobi* (1804-1851): German mathematician.

Substituting $\mathbf{x}$ by its reference position $\mathbf{X}_\alpha$ yields the expressions in the current configuration as

$$\overset{\prime}{\mathbf{x}}_\alpha = \overset{\prime}{\mathbf{x}}_\alpha[\boldsymbol{\chi}_\alpha^{-1}(\mathbf{x},\, t),\, t] = \overset{\prime}{\mathbf{x}}_\alpha(\mathbf{x},\, t) \quad \text{and} \quad \overset{\prime\prime}{\mathbf{x}}_\alpha = \overset{\prime\prime}{\mathbf{x}}_\alpha[\boldsymbol{\chi}_\alpha^{-1}(\mathbf{x},\, t),\, t] = \overset{\prime\prime}{\mathbf{x}}_\alpha(\mathbf{x},\, t). \tag{2.11}$$

In comparison to (2.7), the velocity of the overall aggregate is introduced as

$$\dot{\mathbf{x}} := \frac{1}{\rho}\sum_\alpha \rho^\alpha \overset{\prime}{\mathbf{x}}_\alpha, \tag{2.12}$$

where $\dot{\mathbf{x}}$ is also known as the barycentric velocity. A detailed derivation of $\dot{\mathbf{x}}$ refers to Section 2.2.2. Following this definition, the difference between the velocity of the constituent and the barycentric velocity is then defined as the so-called diffusion velocity via

$$\mathbf{d}_\alpha := \overset{\prime}{\mathbf{x}}_\alpha - \dot{\mathbf{x}} \quad \text{with} \quad \sum_\alpha \rho^\alpha \mathbf{d}_\alpha = \sum_\alpha \rho^\alpha \overset{\prime}{\mathbf{x}}_\alpha - \dot{\mathbf{x}}\sum_\alpha \rho^\alpha = \mathbf{0}. \tag{2.13}$$

2.1.3   Deformations and strains

Due to the idea of a spatially superimposed material point, the position vectors for all constituents are identical in the current configuration. Hence, there is no need to mention the constituent when computing the spatial gradient. However, regarding the fact that the constituents might start from different referential positions, the choice of the referred constituent φ^α must be clarified when defining the material gradient. Based on this finding, the material and spatial gradients are defined as

$$\operatorname{Grad}_\alpha \boldsymbol{\Psi} := \frac{\partial \boldsymbol{\Psi}}{\partial \mathbf{X}_\alpha} \quad \text{and} \quad \operatorname{grad} \boldsymbol{\Psi} := \frac{\partial \boldsymbol{\Psi}}{\partial \mathbf{x}}. \tag{2.14}$$

For example, the deformation gradient of the constituent φ^α and its inverse are defined as

$$\mathbf{F}_\alpha := \frac{\partial \boldsymbol{\chi}_\alpha(\mathbf{X}_\alpha, t)}{\partial \mathbf{X}_\alpha} = \operatorname{Grad}_\alpha \mathbf{x} \quad \text{and} \quad \mathbf{F}_\alpha^{-1} := \frac{\partial \boldsymbol{\chi}_\alpha^{-1}(\mathbf{X}_\alpha, t)}{\partial \mathbf{x}} = \operatorname{grad} \mathbf{X}_\alpha. \tag{2.15}$$

These two tensors provide covariant vectors, e. g. the local line elements, with the so-called covariant push-forward (from reference to current configurations) and pull-back (from current to reference configurations) transformations, respectively,

$$d\mathbf{x} = \mathbf{F}_\alpha \, d\mathbf{X}_\alpha \quad \text{and} \quad d\mathbf{X}_\alpha = \mathbf{F}_\alpha^{-1} \, d\mathbf{x}, \tag{2.16}$$

where $d\mathbf{X}_\alpha$ and $d\mathbf{x}$ are the local line elements in the reference and current configurations. For contravariant vectors, e. g. the local area elements in the reference and current configurations, $d\mathbf{A}_\alpha$ and $d\mathbf{a}$, the push-forward mapping tensor is given by $\operatorname{cof}\mathbf{F}_\alpha$

$$d\mathbf{a} = \operatorname{cof}\mathbf{F}_\alpha \, d\mathbf{A}_\alpha \quad \text{with} \quad \operatorname{cof}\mathbf{F}_\alpha := (\det \mathbf{F}_\alpha)\, \mathbf{F}_\alpha^{T-1}. \tag{2.17}$$

Herein, the determinant of the deformation gradient $\det \mathbf{F}_\alpha$ also relates the reference volume element dV_α to its current one dv by

$$dv = \det \mathbf{F}_\alpha \, dV_\alpha \quad \text{and} \quad \det \mathbf{F}_\alpha = \frac{dv}{dV_\alpha}. \tag{2.18}$$

Combining this relation and (2.5), the partial density is derived via

$$\rho^\alpha = \rho_0^\alpha (\det \mathbf{F}_\alpha)^{-1}, \tag{2.19}$$

where ρ_0^α is the initial value of ρ^α at time $t = 0$. The inverse of the deformation gradient can be formulated as

$$\mathbf{F}_\alpha^{-1} = \frac{(\operatorname{cof} \mathbf{F}_\alpha)^T}{\det \mathbf{F}_\alpha} \quad \text{with} \quad \det \mathbf{F}_\alpha > 0, \tag{2.20}$$

which is a direct result regarding the physical meaning of volume elements (positive value). The initial (undeformed) state yields that the deformation gradient must be an identity tensor at the beginning and its determinant hence must be one,

$$\mathbf{F}_\alpha(t = t_0) = \operatorname{Grad}_\alpha \mathbf{X}_\alpha = \mathbf{I} \quad \text{and} \quad \det \mathbf{F}_\alpha(t = t_0) = 1. \tag{2.21}$$

When one investigates the scalar product of the line elements, the following relations are deduced, where the right and left *Cauchy*[2]-*Green*[3] tensors, $\mathbf{C}_\alpha$ and $\mathbf{B}_\alpha$, transform the square of line elements from the reference to current configuration and vice versa, as:

$$\mathrm{d}\mathbf{x} \cdot \mathrm{d}\mathbf{x} = (\mathbf{F}_\alpha \, \mathrm{d}\mathbf{X}_\alpha) \cdot (\mathbf{F}_\alpha \, \mathrm{d}\mathbf{X}_\alpha) = \mathrm{d}\mathbf{X}_\alpha \cdot \mathbf{C}_\alpha \, \mathrm{d}\mathbf{X}_\alpha \qquad \text{with} \quad \mathbf{C}_\alpha := \mathbf{F}_\alpha^T \, \mathbf{F}_\alpha,$$
$$\tag{2.22}$$
$$\mathrm{d}\mathbf{X}_\alpha \cdot \mathrm{d}\mathbf{X}_\alpha = (\mathbf{F}_\alpha^{-1} \, \mathrm{d}\mathbf{x}) \cdot (\mathbf{F}_\alpha^{-1} \, \mathrm{d}\mathbf{x}) = \mathrm{d}\mathbf{x} \cdot \mathbf{B}_\alpha^{-1} \, \mathrm{d}\mathbf{x} \qquad \text{with} \quad \mathbf{B}_\alpha := \mathbf{F}_\alpha \, \mathbf{F}_\alpha^T.$$

If the difference between the square of the line elements in these two configurations is compared, the notion "strain" of a body can be introduced via

$$\mathrm{d}\mathbf{x} \cdot \mathrm{d}\mathbf{x} - \mathrm{d}\mathbf{X}_\alpha \cdot \mathrm{d}\mathbf{X}_\alpha = \begin{cases} \mathrm{d}\mathbf{X}_\alpha \cdot (\mathbf{C}_\alpha - \mathbf{I}) \, \mathrm{d}\mathbf{X}_\alpha = \mathrm{d}\mathbf{X}_\alpha \cdot 2\mathbf{E}_\alpha \, \mathrm{d}\mathbf{X}_\alpha, \\[2mm] \mathrm{d}\mathbf{x} \cdot (\mathbf{I} - \mathbf{B}_\alpha^{-1}) \, \mathrm{d}\mathbf{x} = \mathrm{d}\mathbf{x} \cdot 2\mathbf{A}_\alpha \, \mathrm{d}\mathbf{x}, \end{cases} \tag{2.23}$$

where $\mathbf{E}_\alpha$ and $\mathbf{A}_\alpha$ denote the *Green-Lagrange*an[4] and *Almansi*an[5] strain tensors, respectively,

$$\mathbf{E}_\alpha = \frac{1}{2}(\mathbf{C}_\alpha - \mathbf{I}), \qquad\qquad \mathbf{A}_\alpha = \frac{1}{2}(\mathbf{I} - \mathbf{B}_\alpha^{-1}). \tag{2.24}$$

The factor, $\frac{1}{2}$, makes the definition of strain tensors consistent with the traditional engineering strain or the well-known *Hook*ean[6] elasticity law after a geometrical linearisation. The transformation between these two tensors refers to the contravariant push-forward and pull-back mapping for a second-order tensor,

$$\mathbf{A}_\alpha = \mathbf{F}_\alpha^{T-1} \, \mathbf{E}_\alpha \, \mathbf{F}_\alpha^{-1}, \qquad\qquad \mathbf{E}_\alpha = \mathbf{F}_\alpha^T \, \mathbf{A}_\alpha \, \mathbf{F}_\alpha. \tag{2.25}$$

---

[2] *Augustin Louis Cauchy* (1789-1857): French mathematician.

[3] *George Green* (1793-1841): British miller and self-taught mathematician.

[4] *Joseph-Louis Lagrange*, born *Giuseppe Lodovico Lagrangia* (1736-1813): Italian mathematician and astronomer.

[5] *Emilio Almansi* (1869-1948): Italian physicist and mathematician.

[6] *Robert Hook* (1635-1703): English natural philosopher, architect and polymath. "Polymath" represents the person who has a broad interest ranged from mathematics, physics, biology, chemistry, astrology, astronomy, philosophy, writing and gambling.

2.1.4 Velocity gradient and deformation rates

When discussing the time derivative, the material time derivative is defined as the total time derivative. Obviously, there is no difference if the interested quantity is expressed in the reference configuration. However, attention needs to be paid to the derivatives in the current configuration. Unlike the single-phasic material, the material time derivative in the TPM must be assigned to a specific constituent due to the existence of different velocities at this superimposed material point. Hence, the material time derivatives of scalar-valued and vector-valued quantities with respect to constituent φ^α are defined as

$$
\begin{aligned}
(\Psi)'_\alpha &= \frac{\mathrm{d}_\alpha \Psi}{\mathrm{d}\,t} = \frac{\partial\,\Psi}{\partial\,t} + \operatorname{grad}\Psi \cdot \mathbf{v}_\alpha, \\
(\boldsymbol{\Psi})'_\alpha &= \frac{\mathrm{d}_\alpha \boldsymbol{\Psi}}{\mathrm{d}\,t} = \frac{\partial\,\boldsymbol{\Psi}}{\partial\,t} + (\operatorname{grad}\boldsymbol{\Psi})\,\mathbf{v}_\alpha.
\end{aligned}
\tag{2.26}
$$

Moreover, the material time derivatives between two different constituents φ^α and φ^β are related by the following equations,

$$
(\Psi)'_\alpha = (\Psi)'_\beta + \operatorname{grad}\Psi \cdot (\mathbf{v}_\alpha - \mathbf{v}_\beta), \quad (\boldsymbol{\Psi})'_\alpha = (\boldsymbol{\Psi})'_\beta + \operatorname{grad}\boldsymbol{\Psi}\,(\mathbf{v}_\alpha - \mathbf{v}_\beta), \tag{2.27}
$$

.

If one recalls the preceding sections, the material and spatial velocity gradients are obtained by

$$
(\mathbf{F}_\alpha)'_\alpha = \frac{\mathrm{d}_\alpha}{\mathrm{d}\,t}\Big(\frac{\partial \mathbf{x}_\alpha}{\partial \mathbf{X}_\alpha}\Big) = \frac{\partial \overset{\prime}{\mathbf{x}}_\alpha}{\partial \mathbf{X}_\alpha} \quad \text{and} \quad \mathbf{L}_\alpha = \frac{\partial \overset{\prime}{\mathbf{x}}_\alpha}{\partial \mathbf{x}}, \tag{2.28}
$$

which map the material and spatial line elements to its velocity elements, respectively. These velocity gradients are related to each other by the inverse of the deformation gradient, i.e.,

$$
\mathrm{d}\,\overset{\prime}{\mathbf{x}}_\alpha = (\mathbf{F}_\alpha)'_\alpha \mathrm{d}\,\mathbf{X}_\alpha = (\mathbf{F}_\alpha)'_\alpha\,\mathbf{F}_\alpha^{-1}\mathrm{d}\,\mathbf{x} = \mathbf{L}_\alpha\,\mathrm{d}\,\mathbf{x} \quad \text{and} \quad \mathbf{L}_\alpha = (\mathbf{F}_\alpha)'_\alpha\,\mathbf{F}_\alpha^{-1}. \tag{2.29}
$$

Regarding the definition of the spatial velocity gradient, the trace of $\mathbf{L}_\alpha$ can also be interpreted as the divergence of the velocity $\overset{\prime}{\mathbf{x}}_\alpha$, compare,

$$
\mathbf{L}_\alpha = \operatorname{grad}\overset{\prime}{\mathbf{x}}_\alpha \quad \text{and} \quad \mathbf{L}_\alpha \cdot \mathbf{I} = \operatorname{div}\overset{\prime}{\mathbf{x}}_\alpha. \tag{2.30}
$$

By splitting the tensor $\mathbf{L}_\alpha$ into a symmetric part and a skew-symmetric part, one yields the rate of deformation $\mathbf{D}_\alpha$ and the spin tensor $\mathbf{W}_\alpha$. When computing the rate of the square of the current line elements, the following relation is derived,

$$
(\mathrm{d}\mathbf{x} \cdot \mathrm{d}\mathbf{x})'_\alpha = \mathrm{d}\mathbf{X}_\alpha \cdot (\mathbf{C}_\alpha)'_\alpha\,\mathrm{d}\mathbf{X}_\alpha = \mathrm{d}\mathbf{X}_\alpha \cdot (2\mathbf{F}_\alpha^T\,\mathbf{D}_\alpha\,\mathbf{F}_\alpha)\,\mathrm{d}\mathbf{X}_\alpha = \mathrm{d}\mathbf{x} \cdot (2\,\mathbf{D}_\alpha)\,\mathrm{d}\mathbf{x}, \tag{2.31}
$$

where the transformation is considered as

$$
(\mathbf{C}_\alpha)'_\alpha = (\mathbf{F}_\alpha^T \mathbf{F}_\alpha)'_\alpha = ((\mathbf{F}_\alpha)'_\alpha)^T \mathbf{F}_\alpha + \mathbf{F}_\alpha^T (\mathbf{F}_\alpha)'_\alpha = \mathbf{F}_\alpha^T \mathbf{L}^T \mathbf{F}_\alpha + \mathbf{F}_\alpha^T \mathbf{L}_\alpha \mathbf{F}_\alpha = 2\mathbf{F}_\alpha^T \mathbf{D}_\alpha \mathbf{F}_\alpha. \tag{2.32}
$$

It is concluded that the rate of the deformation tensor $\mathbf{D}_\alpha$ maps the square of the current line element $\mathrm{d}\mathbf{x}$ to the temporal change of this square $(\mathrm{d}\mathbf{x} \cdot \mathrm{d}\mathbf{x})'_\alpha$ while $(\mathbf{C}_\alpha)'_\alpha$ transforms

the square of the referential line element $\mathrm{d}\mathbf{X}_\alpha$ to this time derivative. Additionally, $(\mathbf{E}_\alpha)'_\alpha$ is derived as a half of $(\mathbf{C}_\alpha)'_\alpha$, which can also be obtained by a contravariant pull-back transformation of $\mathbf{D}_\alpha$, compare (2.25),

$$(\mathbf{E}_\alpha)'_\alpha = \frac{1}{2}(\mathbf{C}_\alpha)'_\alpha = \mathbf{F}_\alpha^T \mathbf{D}_\alpha \mathbf{F}_\alpha. \tag{2.33}$$

2.1.5 Stresses

In a typical thermodynamical problem, the load coming from the environment around the body $\mathcal{B}$ results in changes of certain quantities, e. g. mass or temperature, within the body. For an arbitrary point on the surface, the traction force applied to it is not only dependent on its position and time but also the orientation of the surface. Therefore, the traction vector per unit surface area is defined as a function of $\mathbf{x}$, t and the outward-oriented unit surface normal vector $\mathbf{n}$. Regarding this, the *Cauchy* stress theorem defines the *Cauchy* stress tensor $\mathbf{T}$ via

$$\mathbf{t}(\mathbf{x},\, t,\, \mathbf{n}) = \mathbf{T}(\mathbf{x},\, t)\mathbf{n}, \tag{2.34}$$

which states that the stress tensor $\mathbf{T}$ maps the surface normal vector $\mathbf{n}$ to the corresponding traction force $\mathbf{t}$. Attention needs to be paid that both of the vectorial terms, $\mathbf{n}$ and $\mathbf{t}$, are in the current configuration. In addition, the *Cauchy* stress tensor for a constituent φ^α is denoted by $\mathbf{T}^\alpha$. If different area elements of the constituent α are considered, the partial stress tensors $\boldsymbol{\tau}^\alpha$ and $\mathbf{P}^\alpha$ related to the current force element $\mathrm{d}\mathbf{k}^\alpha$ are then defined as the *Kirchhoff*[7] and 1st *Piola*[8]-*Kirchhoff* stress tensors, respectively,

$$\mathrm{d}\mathbf{k}^\alpha = \mathbf{T}^\alpha\, \mathrm{d}\mathbf{a} = \boldsymbol{\tau}^\alpha\, \mathrm{d}\bar{\mathbf{a}}^\alpha = \mathbf{P}^\alpha\, \mathrm{d}\mathbf{A}^\alpha, \tag{2.35}$$

where $\mathrm{d}\mathbf{A}^\alpha$ is the reference area element and the weighted area element $\mathrm{d}\bar{\mathbf{a}}^\alpha$ is given by

$$\mathrm{d}\bar{\mathbf{a}}^\alpha = (\det \mathbf{F}_\alpha)^{-1}\mathrm{d}\mathbf{a}. \tag{2.36}$$

Pulling back the force element to the reference configuration introduces the partial 2nd *Piola-Kirchhoff* stress tensor $\mathbf{S}^\alpha$:

$$\mathrm{d}\mathbf{K}^\alpha = \mathbf{F}_\alpha^{-1}\, \mathrm{d}\mathbf{k}^\alpha = \mathbf{S}^\alpha\, \mathrm{d}\mathbf{A}^\alpha, \tag{2.37}$$

where the traction force in the reference configuration $\mathrm{d}\mathbf{K}^\alpha$ does not exist but is an imaginary object. To summarise the stress tensors, the following relations are found,

$$\mathbf{T}^\alpha = (\det \mathbf{F}_\alpha)^{-1}\, \boldsymbol{\tau}^\alpha = (\det \mathbf{F}_\alpha)^{-1}\, \mathbf{P}^\alpha\, \mathbf{F}_\alpha^T = (\det \mathbf{F}_\alpha)^{-1}\, \mathbf{F}_\alpha\, \mathbf{S}^\alpha\, \mathbf{F}_\alpha^T, \tag{2.38}$$

where $\boldsymbol{\tau}^\alpha$ can be obtained by a covariant push-forward transformation of $\mathbf{S}_\alpha$.

---

[7] *Gustav Robert Kirchhoff* (1824-1887): German physicist.
[8] *Gabrio Piola* (1794-1850): Italian mathematician and physicist.

2.2 Balance Relations

Following the procedure in Ehlers [63] and [68], this section starts with an introduction to the balance for an arbitrary physical quantity in the global and local forms. Subsequently, the fundamental balances for a single-phasic material in the range of Continuum Mechanics are given. After a brief explanation of the metaphysical principles, the local balance equations for a constituent α, together with its further derivations, are concluded. At last, an additional discussion on the entropy balance is held so as to derive the *Clausius*[9]-*Planck*[10] inequality that is also the necessary condition for the thermodynamical consistency.

2.2.1 General structures

Before discussing the balances for multi-phasic materials, the conclusions in continuum mechanics are recalled. The general and global form of the balance for an arbitrary physical quantity can be interpreted as

$$\int_{\mathcal{B}} \text{vector-valued:} \qquad \frac{\mathrm{d}}{\mathrm{d}t} \int_{\mathcal{B}} \boldsymbol{\Psi} \, \mathrm{d}v = \int_{\mathcal{S}} (\boldsymbol{\Phi}\,\mathbf{n}) \, \mathrm{d}a + \int_{\mathcal{B}} \boldsymbol{\sigma} \, \mathrm{d}v + \int_{\mathcal{B}} \hat{\boldsymbol{\Psi}} \, \mathrm{d}v, \qquad (2.39)$$

where Ψ and $\boldsymbol{\Psi}$ are the volume-specific scalar- and vector-valued physical quantities while their production terms are expressed by $\hat{\Psi}$ and $\hat{\boldsymbol{\Psi}}$. The external influence includes the effluxes denoted by $\boldsymbol{\phi}$ and $\boldsymbol{\Phi}$, which directly enter the body $\mathcal{B}$ over the surface $\mathcal{S}$, and the volume-specific supply terms σ and $\boldsymbol{\sigma}$, which contribute from a distance. In other words, it tells that the temporal change of a certain quantity within the body $\mathcal{B}$ must be a result of the external loads (acting in the vicinity or distant supply) and the productions (within the body for a closed system or across the surface for an open system). In order to rewrite (2.39) in a local form, the temporal change of an arbitrary quantity can be rewritten as

$$
\begin{aligned}
\frac{\mathrm{d}}{\mathrm{d}t} \int_{\mathcal{B}} (\,\cdot\,) \, \mathrm{d}v &= \int_{\mathcal{B}} [(\dot{\cdot}) \, \mathrm{d}v + (\,\mathrm{d}v\,)^{\cdot}], \text{ with } (\mathrm{d}v)^{\cdot} = \operatorname{div} \dot{\mathbf{x}} \, \mathrm{d}v \\
&= \int_{\mathcal{B}} [(\dot{\cdot}) + (\,\cdot\,) \operatorname{div} \dot{\mathbf{x}}] \, \mathrm{d}v.
\end{aligned}
\qquad (2.40)
$$

Besides, the divergence theorem is necessary to transform the efflux integral through a closed surface to a volume integral over the region inside that surface,

$$\int_{\mathcal{S}} (\boldsymbol{\phi} \cdot \mathbf{n}) \, \mathrm{d}a = \int_{\mathcal{B}} \operatorname{div} \boldsymbol{\phi} \, \mathrm{d}v \quad \text{and} \quad \int_{\mathcal{S}} (\boldsymbol{\Phi}\,\mathbf{n}) \, \mathrm{d}a = \int_{\mathcal{B}} \operatorname{div} \boldsymbol{\Phi} \, \mathrm{d}v. \qquad (2.41)$$

Insertion of (2.40) and (2.41) into (2.39) and assuming that this balance is valid for any arbitrary volumes yields the general form of the balance equations in a local sense:

$$
\begin{aligned}
\text{scalar-valued:} \qquad & \dot{\Psi} + \Psi \operatorname{div} \dot{\mathbf{x}} = \operatorname{div} \boldsymbol{\phi} + \sigma + \hat{\Psi}, \\
\text{vector-valued:} \qquad & \dot{\boldsymbol{\Psi}} + \boldsymbol{\Psi} \operatorname{div} \dot{\mathbf{x}} = \operatorname{div} \boldsymbol{\Phi} + \boldsymbol{\sigma} + \hat{\boldsymbol{\Psi}}.
\end{aligned}
\qquad (2.42)
$$

---

[9] *Rudolf Julius Emanuel Clausius* (1822-1888): German physicist and mathematician.
[10] *Max Karl Ernst Ludwig Planck* (1858-1947): German physicist.

For a thermodynamical process, the basic balances include the balances of mass, momentum, moment of momentum (m.o.m), energy and entropy. For each balance, the involved terms are listed in Table 2.1, where $\mathbf{b}$ is the body force, which in most cases can be con-

Table 2.1: *Definition of the specific terms in the balance equations*

	$\Psi,\ \boldsymbol{\Psi}$	$\phi,\ \boldsymbol{\Phi}$	$\sigma,\ \boldsymbol{\sigma}$	$\hat{\Psi},\ \hat{\boldsymbol{\Psi}}$
mass	ρ	$\mathbf{0}$	0	0
momentum	$\rho\dot{\mathbf{x}}$	$\mathbf{T}$	$\rho\mathbf{b}$	$\mathbf{0}$
m. o. m	$\mathbf{x}\times(\rho\dot{\mathbf{x}})$	$\mathbf{x}\times\mathbf{T}$	$\mathbf{x}\times(\rho\mathbf{b})$	$\mathbf{0}$
energy	$\rho\varepsilon+\frac{1}{2}\dot{\mathbf{x}}\cdot(\rho\dot{\mathbf{x}})$	$\mathbf{T}^T\dot{\mathbf{x}}-\mathbf{q}$	$\dot{\mathbf{x}}\cdot(\rho\mathbf{b})+\rho\,r$	0
entropy	$\rho\eta$	$\boldsymbol{\phi}_\eta$	σ_η	$\hat{\eta}$

sidered as the gravitation force $\mathbf{g}$. Moreover, in the energy balance, ε is the mass-specific internal energy, which is influenced by the heat influx $\mathbf{q}$ and the external heat supply r. As η is a common expression for the mass-specific entropy, $\boldsymbol{\phi}_\eta$ and σ give the entropy efflux and external entropy supply, respectively, while $\hat{\eta}$ is defined as the entropy production. Insertion of the above-mentioned definitions into (2.42) yields the local balance equations, compare Table 2.2. Recalling the property of the cross products for two second-ordered

Table 2.2: *Local balance equations for a single-phasic material*

$$
\begin{aligned}
\text{mass:} \qquad && \dot{\rho}+\rho\,\mathrm{div}\,\dot{\mathbf{x}} &= 0 \\
\text{momentum:} \qquad && \rho\,\ddot{\mathbf{x}} &= \mathrm{div}\,\mathbf{T}+\rho\,\mathbf{b} \\
\text{m.o.m:} \qquad && \mathbf{0} &= \mathbf{I}\times\mathbf{T} \\
\text{energy:} \qquad && \rho\,\dot{\varepsilon} &= \mathbf{T}\cdot\mathbf{L}-\mathrm{div}\,\mathbf{q}+\rho\,r \\
\text{entropy:} \qquad && \rho\,\dot{\eta} &= \mathrm{div}\,\boldsymbol{\phi}_\eta+\sigma_\eta+\hat{\eta}
\end{aligned}
$$

tensors, cf. Appendix A.1.1, the balance of m.o.m is fulfilled by

$$\mathbf{T}=\mathbf{T}^T. \tag{2.43}$$

Additionally, the 2nd thermodynamic law postulates that the entropy production is never negative, namely $\hat{\eta}\geq 0$. Thus, the entropy inequality can be derived as

$$\rho\,\dot{\eta}\geq \mathrm{div}\,\boldsymbol{\phi}_\eta+\sigma_\eta. \tag{2.44}$$

2.2.2   Specific balance relations for a TPM model

Tackling the multi-phasic materials requires a bridge over the balance relations of each constituent and the balance relation of the overall aggregate. In this regard, *Truesdell*[11]

---

[11] *Clifford Ambrose Truesdell III* (1919-2000): American mathematician, natural philosopher, historian of science, and polemicist.

suggested his well-known metaphysical principles, which conclude the general properties of all multi-phasic and multi-constituent materials, cf. Table 2.3.

Table 2.3: *Truesdell's metaphysical principles*

1. *All properties of the mixture must be mathematical consequences of properties of the constituents.*

2. *So as to describe the motion of a constituent, we may in imagination isolate it from the rest of the mixture, provided we allow properly for the actions of the other constituents upon it.*

3. *The motion of the mixture is governed by the same equations as is a single body.*

To be consistent with the structure in (2.39), the global balance equations of the constituent are suggested to be

$$\text{scalar-valued:} \qquad \frac{\mathrm{d}_\alpha}{\mathrm{d}t} \int_{\mathcal{B}} \Psi^\alpha \, \mathrm{d}v = \int_{\mathcal{S}} (\boldsymbol{\phi}^\alpha \cdot \mathbf{n}) \, \mathrm{d}a + \int_{\mathcal{B}} \sigma^\alpha \, \mathrm{d}v + \int_{\mathcal{B}} \hat{\Psi}^\alpha \, \mathrm{d}v,$$

$$\text{vector-valued:} \qquad \frac{\mathrm{d}_\alpha}{\mathrm{d}t} \int_{\mathcal{B}} \boldsymbol{\Psi}^\alpha \, \mathrm{d}v = \int_{\mathcal{S}} (\boldsymbol{\Phi}^\alpha \mathbf{n}) \, \mathrm{d}a + \int_{\mathcal{B}} \boldsymbol{\sigma}^\alpha \, \mathrm{d}v + \int_{\mathcal{B}} \hat{\boldsymbol{\Psi}}^\alpha \, \mathrm{d}v. \qquad (2.45)$$

Moreover, their local forms are given by

$$\text{scalar-valued:} \qquad (\Psi^\alpha)'_\alpha + \Psi^\alpha \operatorname{div} \overset{'}{\mathbf{x}}_\alpha = \operatorname{div} \boldsymbol{\phi}^\alpha + \sigma^\alpha + \hat{\Psi}^\alpha,$$

$$\text{vector-valued:} \qquad (\boldsymbol{\Psi}^\alpha)'_\alpha + \boldsymbol{\Psi}^\alpha \operatorname{div} \overset{'}{\mathbf{x}}_\alpha = \operatorname{div} \boldsymbol{\Phi}^\alpha + \boldsymbol{\sigma}^\alpha + \hat{\boldsymbol{\Psi}}^\alpha. \qquad (2.46)$$

To fulfil the third principle in Table 2.3, the terms in the balances of the overall aggregate are obtained by summing up the balances for each constituent and comparing with (2.39) and (2.45).

	quantity	efflux	supply	production
scalar-valued	$\Psi = \sum_\alpha \Psi^\alpha$	$\boldsymbol{\phi} \cdot \mathbf{n} = \sum_\alpha (\boldsymbol{\phi} - \Psi^\alpha \mathbf{d}_\alpha) \cdot \mathbf{n}$	$\sigma = \sum_\alpha \sigma^\alpha$	$\hat{\Psi} = \sum_\alpha \hat{\Psi}^\alpha$
vector-valued	$\boldsymbol{\Psi} = \sum_\alpha \boldsymbol{\Psi}^\alpha$	$\boldsymbol{\Phi} \, \mathbf{n} = \sum_\alpha (\boldsymbol{\Phi} - \boldsymbol{\Psi}^\alpha \otimes \mathbf{d}_\alpha) \mathbf{n}$	$\boldsymbol{\sigma} = \sum_\alpha \boldsymbol{\sigma}^\alpha$	$\hat{\boldsymbol{\Psi}} = \sum_\alpha \hat{\boldsymbol{\Psi}}^\alpha$

In analogy to the definition in Table 2.1, the required terms in the balances are listed in Table 2.4. Herein, $\hat{\rho}^\alpha$, $\hat{\mathbf{s}}^\alpha$, $\hat{\mathbf{h}}^\alpha$ and $\hat{e}^\alpha$ denote the mass, momentum, m.o.m and energy productions, respectively. Compared to the definitions in Table 2.1, these four terms

Table 2.4: *Definition of scalar-, vector- and tensor-valued terms for each constituent in balance equations*

	Ψ^α, $\boldsymbol{\Psi}^\alpha$	ϕ^α, $\boldsymbol{\Phi}^\alpha$	σ^α, $\boldsymbol{\sigma}^\alpha$	$\hat{\Psi}^\alpha$, $\hat{\boldsymbol{\Psi}}^\alpha$
mass	ρ^α	$\mathbf{0}$	0	$\hat{\rho}^\alpha$
momentum	$\rho^\alpha \overset{\prime}{\mathbf{x}}_\alpha$	$\mathbf{T}^\alpha$	$\rho^\alpha \mathbf{b}^\alpha$	$\hat{\mathbf{s}}^\alpha$
m. o. m	$\mathbf{x} \times (\rho^\alpha \overset{\prime}{\mathbf{x}}_\alpha)$	$\mathbf{x} \times \mathbf{T}^\alpha$	$\mathbf{x} \times (\rho^\alpha \mathbf{b}^\alpha)$	$\hat{\mathbf{h}}^\alpha$
energy	$\rho^\alpha \varepsilon^\alpha + \frac{1}{2} \overset{\prime}{\mathbf{x}}_\alpha \cdot (\rho^\alpha \overset{\prime}{\mathbf{x}}_\alpha)$	$(\mathbf{T}^\alpha)^T \overset{\prime}{\mathbf{x}}_\alpha - \mathbf{q}^\alpha$	$\overset{\prime}{\mathbf{x}}_\alpha \cdot (\rho^\alpha \mathbf{b}^\alpha) + \rho^\alpha r^\alpha$	$\hat{e}^\alpha$
entropy	$\rho^\alpha \eta^\alpha$	ϕ^α_η	σ^α_η	$\hat{\eta}^\alpha$

are no longer zero due to the fact that additional productions might come from the exchange between the constituents within the body $\mathcal{B}$ by crossing the internal boundaries in REV. Furthermore, to distinguish the source of the productions, all production terms are decomposed into a direct production (such as the momentum production due to the contact force between constituents) and an additional production (e. g. the momentum production due to the mass production). According to *Truesdell*'s metaphysical principles, the sum of the productions must vanish such that the overall aggregate behaves as a single body, cf. Table 2.5.

Table 2.5: *Decomposition of the total production for each balance*

total production	=	direct production	+	additional production		
$\sum_\alpha \rho^\alpha$					$=$	0
$\sum_\alpha \hat{\mathbf{s}}^\alpha$	$=$	$\sum_\alpha \hat{\mathbf{p}}^\alpha$	$+$	$\hat{\rho}^\alpha \overset{\prime}{\mathbf{x}}_\alpha$	$=$	$\mathbf{0}$
$\sum_\alpha \hat{\mathbf{h}}^\alpha$	$=$	$\sum_\alpha \hat{\mathbf{m}}^\alpha$	$+$	$\mathbf{x} \times (\hat{\mathbf{p}}^\alpha + \hat{\rho}^\alpha \overset{\prime}{\mathbf{x}}_\alpha)$	$=$	$\mathbf{0}$
$\sum_\alpha \hat{e}^\alpha$	$=$	$\sum_\alpha \hat{\varepsilon}^\alpha$	$+$	$\hat{\mathbf{p}}^\alpha \cdot \overset{\prime}{\mathbf{x}}_\alpha + \hat{\rho}^\alpha (\varepsilon^\alpha + \frac{1}{2} \overset{\prime}{\mathbf{x}}_\alpha \cdot \overset{\prime}{\mathbf{x}}_\alpha)$	$=$	0
$\sum_\alpha \hat{\eta}^\alpha$	$=$	$\sum_\alpha \hat{\zeta}^\alpha$	$+$	$\hat{\rho}^\alpha \eta^\alpha$	$\geq$	0

For the same consideration, the basic thermodynamic quantities for the overall aggregate are given in (2.47). Therein, ρ and $\dot{\mathbf{x}}$ have already been introduced in Section 2.1.1 and 2.1.2. With the definition in Table 2.4, the general balance equations (2.46) are extended

in Table 2.6.

$$
\begin{aligned}
\rho &= \sum_\alpha \rho^\alpha, & \mathbf{T} &= \sum_\alpha \left(\mathbf{T}^\alpha - \rho\, \mathbf{d}_\alpha \otimes \mathbf{d}_\alpha \right), \\
\rho\, \dot{\mathbf{x}} &= \sum_\alpha \rho^\alpha\, \overset{'}{\mathbf{x}}_\alpha, & \rho\, \ddot{\mathbf{x}} &= \sum_\alpha \left[\overset{''}{\mathbf{x}}_\alpha - \operatorname{div}\left(\rho \mathbf{d}_\alpha \otimes \mathbf{d}_\alpha \right) + \hat{\rho}^\alpha\, \overset{'}{\mathbf{x}}\alpha \right], \\
\rho\, r &= \sum_\alpha \rho^\alpha \left(r^\alpha + \mathbf{b}^\alpha \cdot \mathbf{d}_\alpha \right), & \rho\, \varepsilon &= \sum_\alpha \rho^\alpha \left(\varepsilon^\alpha + \tfrac{1}{2}\, \mathbf{d}_\alpha \cdot \mathbf{d}_\alpha \right), \\
\rho\, \mathbf{b} &= \sum_\alpha \rho^\alpha\, \mathbf{b}^\alpha, & \mathbf{q} &= \sum_\alpha \left[\mathbf{q}^\alpha - (\mathbf{T}^\alpha)^T \mathbf{d}_\alpha + \rho^\alpha \varepsilon^\alpha\, \mathbf{d}_\alpha + \right], \\
& & & \quad + \tfrac{1}{2} \left(\mathbf{d}_\alpha \cdot \mathbf{d}_\alpha \right) \mathbf{d}_\alpha \Big]
\end{aligned}
\tag{2.47}
$$

Due to the existence of production terms, further discussion is needed for the m.o.m balance. For a single-phasic material, the m.o.m balance is fulfilled by (2.43), while for a multiphasic material, this balance holds for the case that the *Cauchy* stress tensor is linked to its transpose by

$$
\mathbf{T}^\alpha = (\mathbf{T}^\alpha)^T - \hat{\mathbf{M}}^\alpha \quad \text{with} \quad \hat{\mathbf{m}}^\alpha = \frac{1}{2}\, (\mathbf{I} \times \hat{\mathbf{M}}^\alpha),
\tag{2.48}
$$

where $\hat{\mathbf{M}}^\alpha$ is the skew-symmetric moment of momentum coupling tensor, cf. Ehlers [70]. Thereafter, the definition of the stress of the overall aggregate is recalled, cf. $(2.47)_2$. It is apparent that the term $\rho\, \mathbf{d}_\alpha \otimes \mathbf{d}_\alpha$ is a symmetric tensor. Hence, if each individual constituent is a standard *Cauchy* material and the stress tensor of each constituent is symmetric (in a micro-structure sense), the stress tensor of the overall aggregate will also be symmetric (in a macro-structure sense). In other words, the property of the symmetry of the constituent stress tensor is preserved during the homogenisation process, cf. Hassanizadeh and Gray [108] and Ehlers [68]. Hence, it is assumed that

$$
\mathbf{T}^\alpha = (\mathbf{T}^\alpha)^T,
\tag{2.49}
$$

which results in $\hat{\mathbf{M}}^\alpha = \mathbf{0}$ and

$$
\hat{\mathbf{m}}^\alpha = \mathbf{0}.
\tag{2.50}
$$

Proceeding from the definition of m.o.m production, one observes that the sum of the additional production term must vanish,

$$
\sum_\alpha \mathbf{x} \times (\hat{\mathbf{p}}^\alpha + \hat{\rho}\, \overset{'}{\mathbf{x}}_\alpha) = \mathbf{x} \times \sum_\alpha (\hat{\mathbf{p}}^\alpha + \hat{\rho}\, \overset{'}{\mathbf{x}}_\alpha) = \mathbf{0},
\tag{2.51}
$$

because the term inside the parentheses is the momentum production and the sum of this term is a zero tensor. Regarding this, the restriction of the m.o.m production is reduced to

$$
\sum_\alpha \hat{\mathbf{m}}^\alpha \equiv \mathbf{0},
\tag{2.52}
$$

which reduces the sum of m.o.m production to the sum of the direct m.o.m production. This equation is automatically satisfied by the assumption (2.50).

Table 2.6: *Local balance equations for constituent*

mass:	$(\rho^\alpha)'_\alpha + \rho^\alpha \operatorname{div} \overset{\prime}{\mathbf{x}}_\alpha$	$=$	$\hat{\rho}^\alpha$
momentum:	$\rho^\alpha \overset{\prime\prime}{\mathbf{x}}_\alpha$	$=$	$\operatorname{div} \mathbf{T}^\alpha + \rho^\alpha \mathbf{b}^\alpha + \hat{\mathbf{p}}^\alpha$
m.o.m.:	$\mathbf{0}$	$=$	$\mathbf{I} \times \mathbf{T}^\alpha + \hat{\mathbf{m}}^\alpha$
energy:	$\rho^\alpha (\varepsilon^\alpha)'_\alpha$	$=$	$\mathbf{T}^\alpha \cdot \mathbf{L}_\alpha - \operatorname{div} \mathbf{q}^\alpha + \rho^\alpha r^\alpha + \hat{\varepsilon}^\alpha$
entropy:	$\rho^\alpha (\eta^\alpha)'_\alpha$	$=$	$\operatorname{div} \boldsymbol{\phi}^\alpha_\eta + \sigma^\alpha_\eta + \hat{\zeta}^\alpha$

As an opposite case against *Cauchy* type materials, granular materials are so-called micro-polar materials, which, at the micro scale, are defined as rotatable particles. As a result, an additional degree of freedom, the rotation angle must be accounted for leading to an asymmetrical stress tensor. The interested reader might refer to the work of *Cosserat* brother [50, 51]. For the *Cosserat* model in the framework of the TPM, compare the work of Diebels & Ehlers [57], Diebels [58], Ehlers [68], Ehlers & Volk [64, 65] and Scholz [186].

2.2.3 Entropy inequality

For further discussion about entropy, a priori constitutive equations are given here,

$$\phi^\alpha_\eta = \frac{1}{\theta^\alpha} \mathbf{q}^\alpha \quad \text{and} \quad \sigma^\alpha_\eta = \frac{1}{\theta^\alpha} \rho^\alpha r^\alpha, \tag{2.53}$$

where θ^α is the absolute *Kelvin*[12] temperature and subject to the condition that $\theta^\alpha > 0$. These relations correspond to a single-phasic material, cf. Ehlers [63]. As a consequence of (2.44), the entropy of the overall aggregate must satisfy that

$$\hat{\eta} = \sum_\alpha \hat{\eta}^\alpha = \sum_\alpha \left[\rho^\alpha (\eta^\alpha)'_\alpha + \operatorname{div}(\frac{1}{\theta} \mathbf{q}^\alpha) - \frac{1}{\theta^\alpha} \rho^\alpha r^\alpha + \hat{\rho}^\alpha \eta^\alpha \right] \geq 0. \tag{2.54}$$

The internal energy ε^α is usually considered as a function depending on the strain tensor, e. g. $\mathbf{E}_\alpha$ and the entropy η^α. However, the conjugate term of the entropy, namely the temperature θ^α, is easier to measure or to observe during the natural process or experiments. Thus, the so-called *Helmholtz*[13] free energy ψ^α, depending on the temperature and the strain, is introduced into the energy balance by the *Legendre*[14] transformation as

$$\psi^\alpha := \varepsilon^\alpha - \theta^\alpha \eta^\alpha. \tag{2.55}$$

Therewith, the entropy inequality is reformulated as

$$\sum_\alpha \frac{1}{\theta^\alpha} \left\{ \mathbf{T}^\alpha \cdot \mathbf{L}_\alpha - \rho^\alpha [(\psi^\alpha)'_\alpha + (\theta^\alpha)'_\alpha \eta^\alpha] - \hat{\mathbf{p}}^\alpha \cdot \overset{\prime}{\mathbf{x}}_\alpha - \right.$$
$$\left. -\hat{\rho}^\alpha (\psi^\alpha + \frac{1}{2} \overset{\prime}{\mathbf{x}}_\alpha \cdot \overset{\prime}{\mathbf{x}}_\alpha) - \frac{1}{\theta^\alpha} \mathbf{q}^\alpha \cdot \operatorname{grad} \theta^\alpha + \hat{e}^\alpha \right\} \geq 0, \tag{2.56}$$

---

[12] *William Thomson, 1st Baron Kelvin* (1824-1907): Scots-Irish mathematical physicist and engineer.
[13] *Hermann Ludwig Ferdinand von Helmholtz* (1821-1894): German physician and physicist.
[14] *Adrien-Marie Legendre* (1752-1833): French mathematician.

which is also known as the *Clausius-Duhem*[15] inequality. For a purely mechanical model, where the thermal effect does not play a role, the temperature is assumed to be spatially and temporally constant:

$$\theta = \theta^\alpha \equiv \text{const.} \tag{2.57}$$

Taking into account that the absolute *Kelvin* temperature is always a positive number helps to reduce the above-mentioned inequality to the so-called *Clausius-Planck* inequality:

$$\sum_\alpha \left[\, \mathbf{T}^\alpha \cdot \mathbf{L}_\alpha - \rho^\alpha (\psi^\alpha)'_\alpha - \hat{\mathbf{p}}^\alpha \cdot \overset{'}{\mathbf{x}}_\alpha - \hat{\rho}^\alpha (\psi^\alpha + \frac{1}{2} \overset{'}{\mathbf{x}}_\alpha \cdot \overset{'}{\mathbf{x}}_\alpha) \right] \geq 0. \tag{2.58}$$

This inequality provides a necessary condition for the thermodynamical consistency and will be further discussed in Chapter 4.

---

[15] *Pierre Maurice Marie Duhem* (1861-1916): French physicist, mathematician and philosopher of science.

Chapter 3:
Fundamentals of Fracture Mechanics

This chapter aims to give a brief introduction to the basic theory of fracture mechanics. It starts with an explanation of the physical mechanism from both macro- and nanoscopic points of view and follows an elementary knowledge of several classical theories such the Stress Intensity Factor, Griffith's theory, and the J-integral. In the last section, a phase-field model applied to fracture is presented, which in the following context is chosen as an approach for the crack phenomena in porous media. For a detailed depiction of fracture mechanics, compare the books of Gross & Seelig [98], Anderson [10], and Kanninen & Popelar [128]. Note that the discussion within this chapter is limited to the failure in a pure solid. For porous media, special considerations need to be paid owing to the heterogeneity of the micro-structure. For example, the failure mechanism of porous materials under compression is discussed in Salje et al. [183].

3.1 What is Fracture?

Fracture is one of the most common and important reasons for structural failure. However, it is not that easy to find an exact definition to conclude these phenomena. From a macroscopic point of view, a fracture can be straightforwardly interpreted as the separation of an object or material into two or more pieces. When one fracture occurs, it must be accompanied by the generation of two new surfaces, forming additional internal boundaries within the body. These new boundaries are the so-called crack surface in three dimensions or the crack lips in two dimensions, the joint curve or point of which is known as crack front or crack tip correspondingly. According to the relative movement of the crack surface, three independent fundamental fracture modes are defined by Irwin [119], cf. Figure 3.1. These basic fracture modes are usually known as Mode I (Opening Mode/Tension), where the two crack surfaces only move in $\mathbf{e}_2$ direction symmetrically
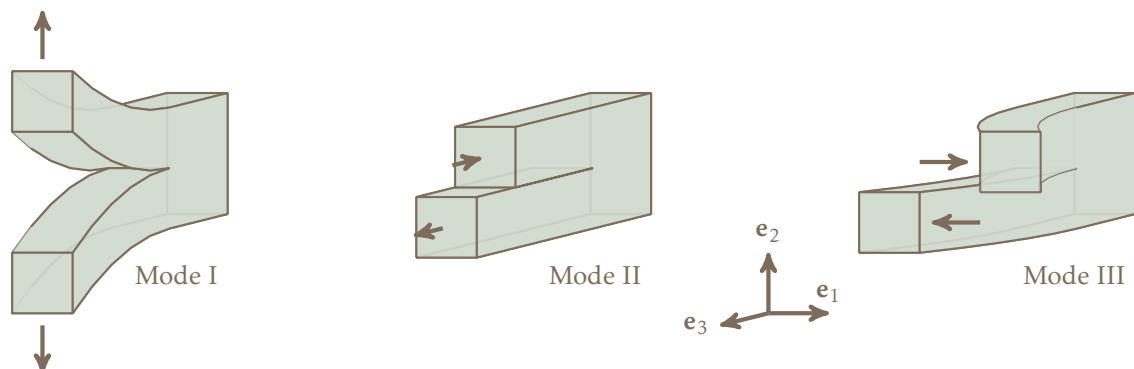

Figure 3.1: *Three fundamental fracture modes.*

with respect to the undeformed crack plane ($\mathbf{e}_1 - \mathbf{e}_3$ plane); Mode II (Sliding Mode/In-plane Shear), where the crack surfaces slide against each other with the same magnitude in $\mathbf{e}_3$ direction; and Mode III (Tearing Mode/Out-of-plane Shear), where the crack parts proceed in the opposite directions parallel to the crack front. In particular, an arbitrary fracture mode can be described as one of these three modes, or their combinations.

On the other hand, from a nanoscopic point of view, a fracture is directly caused by a break of bonds that hold atoms together. These bonds are formed, for example, when the liquid-state metal is cooled down until a polycrystalline structure is accomplished. The bonds are stable owing to the electromagnetic forces between the electrons of neighbour atoms. Note that the inter-atomic distance is reduced with the decrease of temperature, leading to an equilibrium state at the critical distance x_0 of a bond creation. Assume an opposite condition, when a sufficient stress is applied under a tensile test, these bonds will be broken if the atoms are far away from each other and the mutual attractive forces are too small. Following an interpretation in Anderson [10], the bond energy is proposed to be a function of the separation distance d that reaches a minimum at the critical distance x_0, cf. Figure 3.2. In order to force this distance greater than x_0, an external tension force needs to be applied while, on the other hand, the bond shrinks under a compression force. In particular, the work done by the external force has to be equal to the difference of the bond energy. So as to compute the critical strength in this setup, the dependency of the inter-atomic force $\bar{f}$ between atoms on their distance is ideally approximated by a sine wave as shown in Figure 3.2 with a dashed curve,

$$\bar{f} = f_c \sin\left[\frac{\pi(x - x_0)}{\lambda}\right] \quad \text{for} \quad x \in (x_0, x_0 + \lambda). \tag{3.1}$$

Herein, λ is chosen to be the two-time value of the distance between the moments when the force turns from compression to tension and when the maximum tensile force f_c is achieved. Since $\sin(\frac{\pi x}{\lambda}) \approx (\frac{\pi x}{\lambda})$ for a small x, the elastic stiffness around x_0 can be approximated by

$$k = f_c \frac{\pi}{\lambda}. \tag{3.2}$$

Notice that k measures the stiffness of each bond and the more common elastic modulus, *Young*'s[1] modulus E, is referred to a unit area. Therefore, if the number of bonds per unit area is known and expressed by N_b, the *Young*'s modulus can be computed by

$$E = \frac{kN_b}{x_0}. \tag{3.3}$$

In addition, the multiplication of f_c and N_b yields the critical force per unit area, which is usually named after the critical stress and expressed by σ_c. Thus, this stress takes the form of

$$\sigma_c = \frac{E\lambda}{\pi x_0}. \tag{3.4}$$

As the bond energy measures the work done by the external force, it can be approximated under the above assumptions by

$$E_b = \int_{x_0}^{\infty} f \, \mathrm{d}x \approx \int_{x_0}^{x_0+\lambda} f_c \sin\left[\frac{\pi(x - x_0)}{\lambda}\right] \mathrm{d}x. \tag{3.5}$$

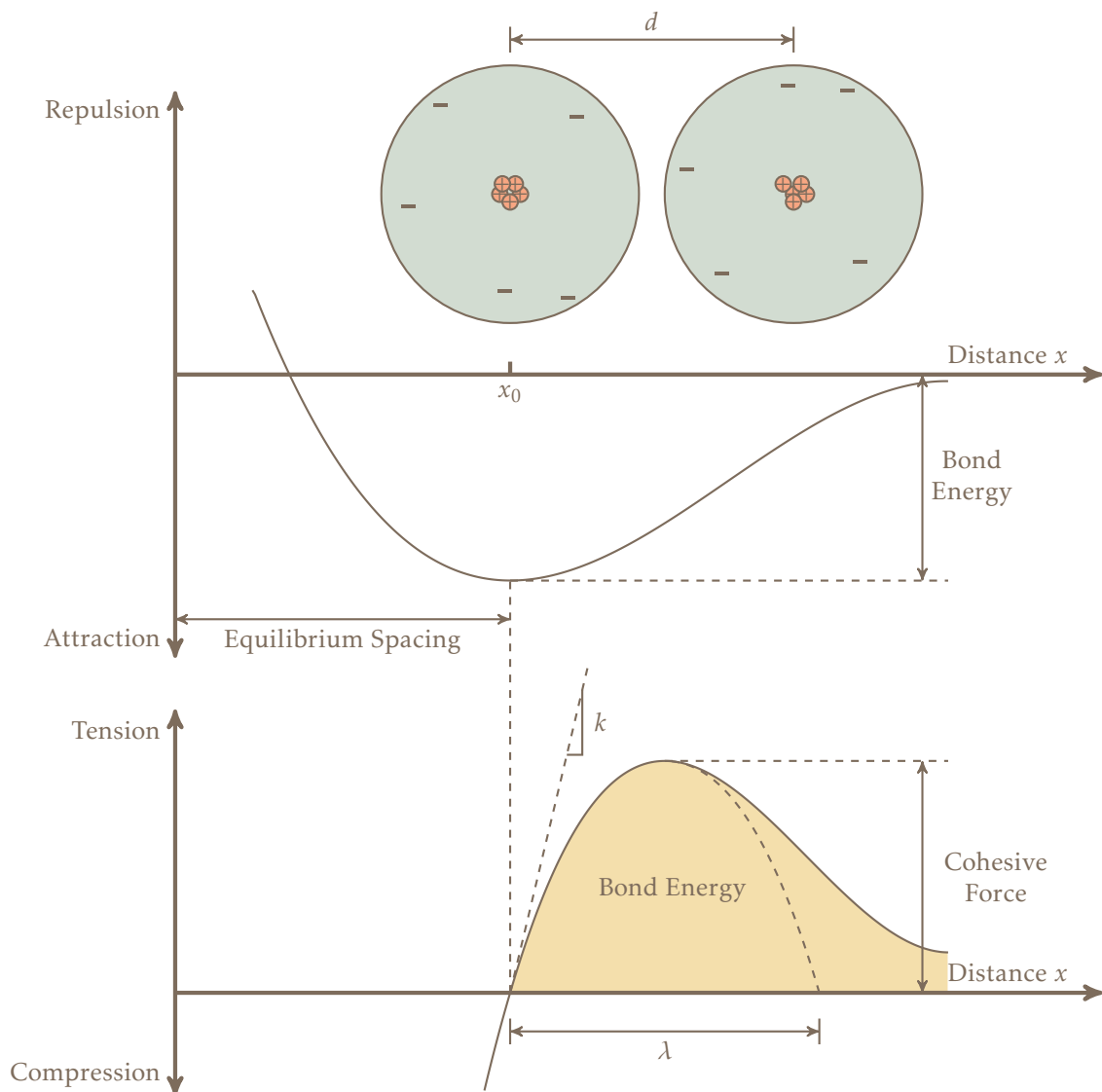[1] *Thomas Young* (1773-1829): English polymath.

Figure 3.2: *Schematic illustration of potential energy and force with respect to the distance between two atoms (originated from Anderson [10]).*

Correspondingly, the surface energy per unit surface area γ_s is defined as one half of the multiplication of E_b and N_b by noticing two surfaces with the same areas are created when a material fractures. In some references, γ_s is also called the surface tension of the material.

$$\gamma_s \approx \frac{1}{2} \int_{x_0}^{x_0+\lambda} \sigma_c \sin\left[\frac{\pi(x - x_0)}{\lambda}\right] dx = \sigma_c \frac{\lambda}{\pi} \tag{3.6}$$

In order to rewrite the critical stress in terms of the surface energy, insertion of (3.17) into (3.5) yields

$$\sigma_c = \sqrt{\frac{E\gamma_s}{x_0}}. \tag{3.7}$$

It is observed that for most materials, the surface energy γ_s is usually on the order of
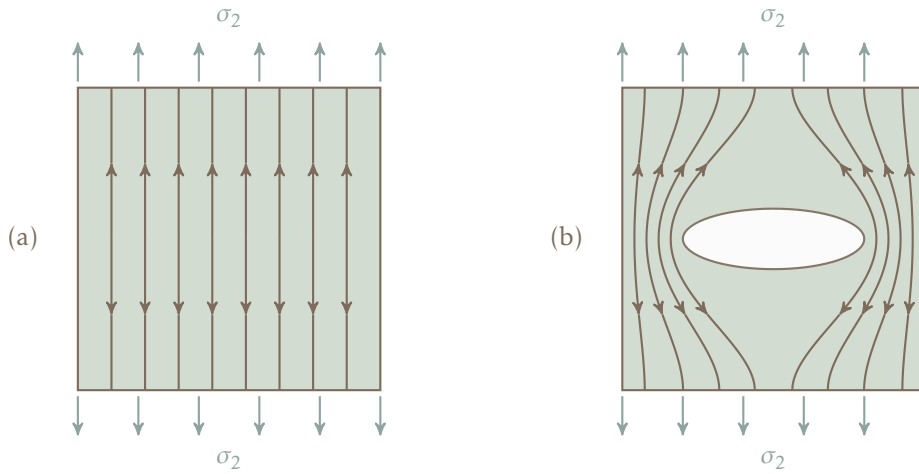
Figure 3.3: *(a) straight stress trajectories (lines of force) in an unbroken plate (b) curved stress trajectories in a plate with an elliptical hole in the middle.*

$0.01E\,x_0$, cf. Cottrel [52]. Hence, a practical estimation of the theoretical strength is given by

$$\sigma_c = \frac{E}{10}. \tag{3.8}$$

However, this result has a large deviation from the one discovered by experiments whereas the experimental result is much lower. The main reason for such a discrepancy is the stress concentration caused by the inevitable flaws in the practical-size bulk material. Details in this regard will be discussed in the following section.

3.2   Stress Concentration and Stress Intensity Factor

In order to explain the discrepancy between the theoretical critical stress and the actual strength, one may firstly consider the following example. As shown in Figure 3.3, a vertical tensile stress is applied to an infinite rectangular plate. In an ideally homogeneous case (a), the paths of the force through the plate are a set of uniformly-distributed straight lines. If an elliptical void is located in the centre, the lines are curved surrounding the hole and squeezed together to fit in a smaller cross-section. This phenomenon is known as the stress concentrations, and the analytical solution was derived by Inglis [118]. In his work, an elliptical hole is settled in the centre of the plate, whose major and minor axis have the lengths of $2a$ and $2b$, respectively, cf. Figure 3.4. The maximum stress occurs at the end of the major axis, and its value is suggested as

$$\sigma_{22}\left(x_1 = \pm a,\, x_2 = 0\right) = \sigma_2\left(1 + 2\,\frac{a}{b}\right). \tag{3.9}$$

Note that a macroscopic notch, in this context, is equivalent to a slit-like ellipse ($\frac{1}{b} \gg 1$). Therefore, the corresponding stress is given by

$$\sigma_{22}(x_1 = \pm a,\, x_2 = 0) \approx 2\,\sigma_2\,\frac{a}{b}. \tag{3.10}$$
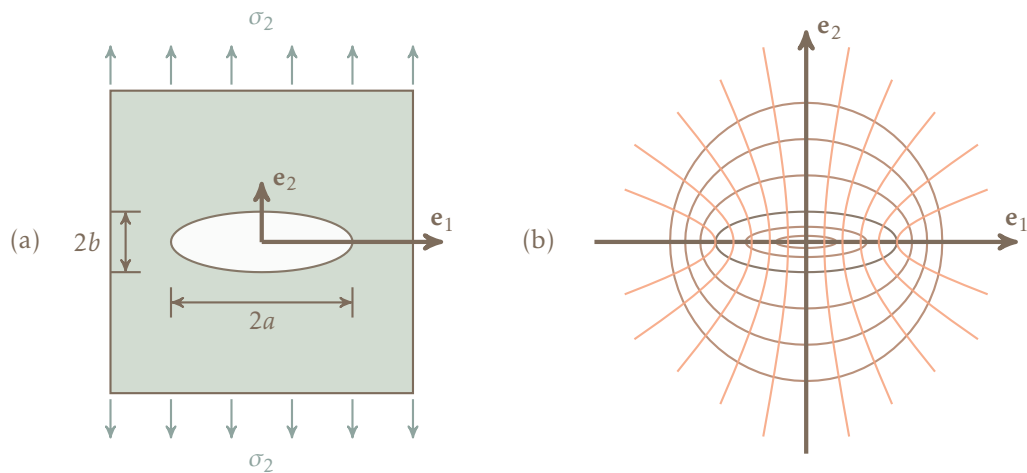
Figure 3.4: *(a) an elliptical hole in an infinite plate subjected to tension (b) an elliptical coordinate system.*

An alternative expression of this conclusion is achieved by substituting the minor axis b by the radius of curvature at the end of a, which reads

$$\sigma_{22}(x_1 = \pm a,\ x_2 = 0) \approx 2\,\sigma_2\,\sqrt{\frac{a}{r}} \quad \text{with} \quad r(x_1 = \pm a,\ x_2 = 0) = \frac{b^2}{a}. \tag{3.11}$$

After realising the significance of (3.11), implying that the stress concentration depends on the shape of the void (the ratio of the major and minor axes) rather than on its absolute size, Irwin proposed his famous concept of **Stress Intensity Factor** (SIF) in [119, 120]. The SIF is usually denoted by K with sub- or superscript I, II, and III corresponding to the three basic crack modes. As shown in Figure 3.5, a polar coordinate system is set up originated from the crack tip which allows an easier expression of the stress field in its
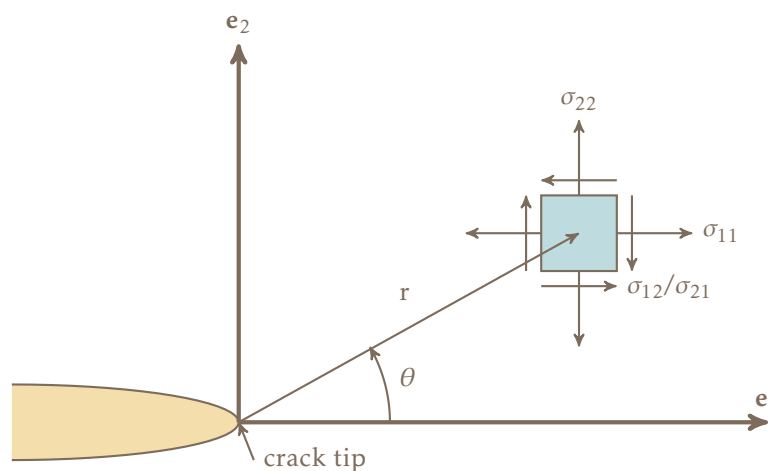

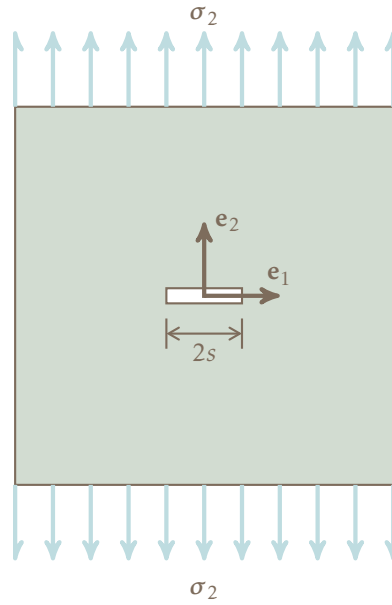**Figure 3.5:** *The polar coordinate system around a crack tip.*

Figure 3.6: *Exemplary illustration of an infinite plate with a sharp crack of length $2s$ subjected to remote stress σ_2.*

vicinity as given by

$$
\begin{aligned}
\sigma_{11} &= \frac{K_I}{\sqrt{2\pi r}}\cos(\frac{\theta}{2})\left[1 - \sin(\frac{\theta}{2})\sin(\frac{3\theta}{2})\right], \\
\sigma_{22} &= \frac{K_I}{\sqrt{2\pi r}}\cos(\frac{\theta}{2})\left[1 + \sin(\frac{\theta}{2})\sin(\frac{3\theta}{2})\right], \\
\sigma_{12} &= \frac{K_I}{\sqrt{2\pi r}}\cos(\frac{\theta}{2})\sin(\frac{\theta}{2})\cos(\frac{3\theta}{2}).
\end{aligned}
\tag{3.12}
$$

Regarding the specific boundary conditions, different solutions are derived, cf. Rooke & Cartwright [181] and Wu & Carlsson [202]. A detailed review in this regard is referred to Yarema [204] and the book of Gross & Seelig [98, 99].

3.3 Griffith's Theory

Griffith's theory is widely accepted as the origin of the modern theory of continuum mechanics applied to brittle fracture, although it is motivated, at the beginning, by the difference between the theoretical stresses for breaking atomic bonds of glass (about 10,000 MPa) and the experimentally detected glass strength (around 100 MPa). By noticing the existence of the inherent defects in brittle materials, Griffith set up a theoretical model, where the defect is substituted by a sharp crack of length $2s$, see Figure 3.6. The criterion of the crack propagation is given as (in his words), *"A crack will propagate when the decrease in elastic strain energy is at least equal to create the new crack"*. To be consistent with the classical continuum mechanics, the total energy of the model is

extended by the surface energy of the whole body denoted by U_Γ,

$$U = \underbrace{U_\text{int} + U_\text{ext}}_{U_\text{pot}} + U_\Gamma. \tag{3.13}$$

In order to compute the minimum of this potential, a standard approach is to satisfy the following relation

$$\frac{\partial U}{\partial s} = 0. \tag{3.14}$$

According to Inglis [118], the increment of the strain energy due to an elliptical crack is given by

$$\Delta U_\text{in} = \frac{\pi(\sigma_2 s)^2}{E'} \quad \text{with} \quad E' = \frac{E}{1 - \nu^2} \quad \text{for plane-strain cases,} \tag{3.15}$$

where ν is known as the *Poisson*'s[2] ratio. Based on *Clapeyron*'s[3] theorem, cf. Fosdick & Truskinovsky [87], the work done by the external load is obtained by

$$U_\text{ext} = -2U_\text{int} \tag{3.16}$$

for linear elastic materials. In addition, the total surface energy U_Γ can be computed via the predefined surface energy per unit surface area γ_s

$$U_\Gamma = 4\gamma_s s. \tag{3.17}$$

where the symbol γ_s is also called the critical strain energy-release rate and substituted by $\mathcal{G}_c$, Inserting (3.15) and (3.17) into (3.14) yields the critical stress triggering the crack propagation

$$\sigma_c = \sqrt{\frac{2E'\gamma_s}{\pi s}}, \tag{3.18}$$

which exhibits a clear relation between the critical stress and the size of an inherent defect, and thus, explains the discrepancy between the theoretical and actual strengths by the comparison with (3.8).

3.4 J-integral

Heretofore, the fracture mechanism is only explained within a pure-elastic domain, which is a rather strong assumption. In order to propose a more general model including inelastic material behaviour, e. g. plasticity, the concept of *J*-integral is introduced by Eshelby [81, 82] and well spread with the literature of Rice [179], which sets up a two-dimensional quasi-static model with a horizontal crack, cf. Figure 3.7 (a). The material is assumed homogeneously linear or nonlinear elastic and the body force is neglected. The *J*-integral is defined as a line integral along the curve Γ surrounding the notch tip and takes the form of

$$J := \int_\Gamma \left(w\, \mathrm{d}x_2 - \mathbf{t} \cdot \frac{\partial \mathbf{u}}{\partial x_1} \right) \mathrm{d}s, \tag{3.19}$$

---

[2] *Siméon Denis Poisson* (1781-1840): French mathematician, geometer, and physicist.
[3] *Benoît Paul Émile Clapeyron* (1799-1864): French engineer and physicist.
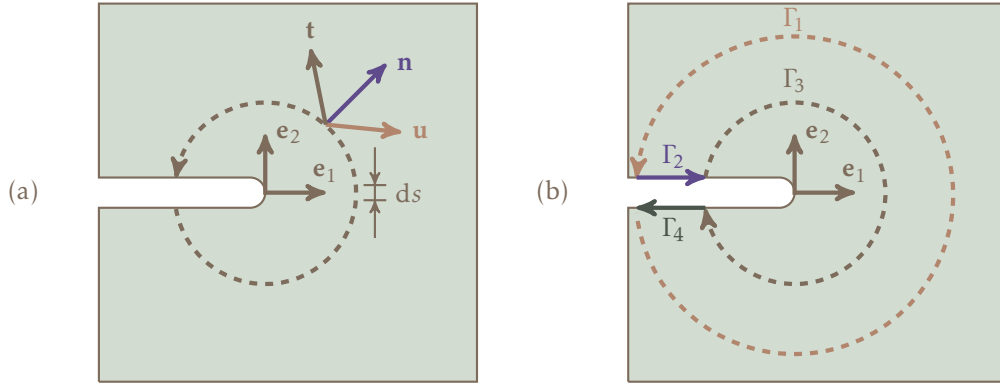
Figure 3.7: *(a) exemplary illustration of the J-integral (b) supplementary illustration in the proof of its path-independency.*

where w is the so-called strain-energy density defined as

$$w = \int_0^\varepsilon \boldsymbol{\sigma} \cdot \mathrm{d}\varepsilon. \tag{3.20}$$

Note that $\boldsymbol{\sigma}$ and $\boldsymbol{\varepsilon}$ in this subsection denote a generalised stress and strain tensor as an exemption in order to be consistent with Rice [179]. Moreover, $\mathbf{u}$ and $\mathbf{t}$ are the displacement and traction force applied to the surface Γ with a normal $\mathbf{n}$. In order to prove the path independency of this integral, a further closed curve Γ is considered, see Figure 3.7 (b). It should be mentioned that the closed curve is divided into four parts and the line integral J is defined with respect to the counterclockwise direction,

$$J_i = \int_{\Gamma_i^{\mathrm{counter}}} \left(w \, \mathrm{d}x_2 - \mathbf{t} \cdot \frac{\partial \mathbf{u}}{\partial x_1} \right) \mathrm{d}s \text{ where } i = 1, 2, 3, 4. \tag{3.21}$$

Regarding this, the J-integral for this closed curve can be computed via

$$J_\Gamma := J_1 - J_2 - J_3 + J_4 = \oint_\Gamma \left(w \, \mathrm{d}x_2 - \mathbf{t} \cdot \frac{\partial \mathbf{u}}{\partial x_1} \right) \mathrm{d}s. \tag{3.22}$$

The application of the *Green*'s theorem then transforms the line integral into an integral over the closed domain bounded by this curve,

$$J_\Gamma = \int_{\Omega_\Gamma} \left[\frac{\partial w}{\partial x_1} - \mathrm{div} \left(\boldsymbol{\sigma} \frac{\partial \mathbf{u}}{\partial x_1} \right) \right] \mathrm{d}a. \tag{3.23}$$

Furthermore, the first term of the integrants can be reformulated by the chain rule yielding the following equation,

$$\frac{\partial w}{\partial x_1} = \frac{\partial w}{\partial \boldsymbol{\varepsilon}} \cdot \frac{\partial \boldsymbol{\varepsilon}}{\partial x_1} = \boldsymbol{\sigma} \cdot \frac{\partial \boldsymbol{\varepsilon}}{\partial x_1}. \tag{3.24}$$

After expanding the second term, one may find the same result

$$\mathrm{div} \left(\boldsymbol{\sigma} \frac{\partial \mathbf{u}}{\partial x_1} \right) = \mathrm{div}\, \boldsymbol{\sigma} \cdot \frac{\partial \mathbf{u}}{\partial x_1} + \boldsymbol{\sigma} \cdot \mathrm{grad}\, \frac{\partial \mathbf{u}}{\partial x_1} = \boldsymbol{\sigma} \cdot \frac{\partial \boldsymbol{\varepsilon}}{\partial x_1}, \tag{3.25}$$

if noticing that the momentum balance is reduced to $\operatorname{div}\boldsymbol{\sigma} = \mathbf{0}$ with the absence of acceleration and body forces while taking the symmetry of the stress tensor into account,

$$\boldsymbol{\sigma} \cdot \operatorname{grad} \frac{\partial \mathbf{u}}{\partial x_1} = \boldsymbol{\sigma} \cdot \frac{1}{2} \left[\operatorname{grad} \frac{\partial \mathbf{u}}{\partial x_1} + \left(\operatorname{grad} \frac{\partial \mathbf{u}}{\partial x_1} \right)^T \right] = \boldsymbol{\sigma} \cdot \frac{\partial \boldsymbol{\varepsilon}}{\partial x_1}. \tag{3.26}$$

Inserting the above results into (3.23) proves the *J*-integral along any arbitrary closed curve always vanishes.

$$J_\Gamma = J_1 - J_2 - J_3 + J_4 = 0 \tag{3.27}$$

However, as no traction force is applied to the crack surface and the range of $\mathrm{d}x_2$ is zero along the crack, the *J*-integrals along the surface Γ_3 and Γ_4 thus are eliminated.

$$J_3 = J_4 = 0 \tag{3.28}$$

Therefore, the integrals J_1 and J_2 are identical,

$$J_1 = J_2, \tag{3.29}$$

which proves the path-independency of the *J*-integral. For further application of the J-integral, the interested reader may compare, for example, Eriksson [80] and Huber et al. [116].

3.5   A Phase-field Approach

The aforementioned theories mainly focus on the mechanism of fracture. In order to describe the material behaviour before and after fracture, the most simple solution is to introduce an additional variable d into the stiffness. For example, the linearised strain-stress relation for a one-dimensional case is modified as

$$\sigma = (1 - d)E\varepsilon. \tag{3.30}$$

If d evolves according to a certain criterion such as an accumulation of the potential energy, a straightforward simulation of fracture nucleation will be done. By interpreting the variable as a damage variable in, e. g. Kachanov [123], this equation also represents a typical damage model. The standard damage model considers failure as material softening, meaning a decreasing stress concerning an increasing strain, see, for example, Kachanov[124], Frémond [90] and Lemaitre [137]. In reviewing the brittle fracture from a macroscopic point of view, a fracture can be regarded as a structural change, e. g. generation of two surfaces and loss of cohesion in-between. In this regard, the damage model substitutes such a structural change by an evolution of material property, in particular, the decrease of stiffness. This approach has an apparent advantage in the numerical implementation because no extra consideration needs to be paid to the geometry and its corresponding mesh. However, it suffers from a so-called pathological effect, since the width of fracture is always dependent on the mesh size, cf. Jirásek [122]. This effect is due to the fact that in a standard damage model, an artificially imperfect region is required to trigger the softening. In addition, the size of this region has to be consistent

with the minimum mesh size, which leads the derived result to be highly influenced by the mesh size. This drawback can be conquered by introducing the non-local theories such as gradient damage model, where a sharp crack is approximated by a diffusive one, cf. Capriz [48], Mariano [145] and Frémond & Nedjar [89].

Nevertheless, without realising the above methodologies, scientists from the physics community proposed a phase-field model to brittle fracture under the inspiration of the Ginzburg-Landau equation, which initially describes superconductivity and then is extended to the phase transition problems. Instead of the damage variable, an order parameter ϕ is usually adopted to characterise different phases. Here, for the sake of uniformity, ϕ is defined as

$$\phi = \begin{cases} 0 \text{ for intact material,} \\ 1 \text{ for fully cracked material.} \end{cases} \tag{3.31}$$

Although various formulation under different considerations can be found in the work of Aranson et al. [11], Hakim & Karma [106], Gurtin [103], and Henry & Levine [114], the basic form of the potential energy may be concluded as

$$\psi(\boldsymbol{\varepsilon},\,\phi) = \int_{\Omega} \{g(\phi)[\psi_0(\boldsymbol{\varepsilon}) - \psi_c] + V(\phi) + D_\phi|\text{grad}\,\phi|^2\}\,\mathrm{d}\,v, \tag{3.32}$$

which involves the overplus stored energy measuring the difference of the total strain energy $\psi_0(\boldsymbol{\varepsilon})$ and the critical energy ψ_c, a so-called Ginzburg-Landau double-well potential $V(\phi)$, and a gradient-type phase energy $D_\phi|\text{grad}\,\phi|^2$. ψ_c is defined as the critical strain energy for crack initiation and thus, the difference between it and the stored strain energy $\psi_0(\mathbf{u})$ provides the work of generating crack surfaces. Note that this potential will be released with the arising cracks, a necessary coupling between the elastic and phase field is then introduced by the degrading function $g(\phi)$ that can be chosen in various ways but must hold for

$$g(\phi) \geq 0 \quad \text{for} \quad \phi \in [0,\,1] \quad , \quad g(\phi = 0) = 1 \quad , \quad g(\phi = 1) = 0. \tag{3.33}$$

The inclusion of the double-well potential $V \propto \phi^2(1 - \phi^2)$ guarantees the two minima for two preferred states $\phi = 0$ and $\phi = 1$ while creating an energy barrier between them, cf. Hakim & Karma [106]. The square terms, by the way, keeps the potential always a positive value. The constant coefficient D_ϕ usually contains a so-call length scale, governing the width of diffusive cracks. In addition, the constitutive equation for stress and the evolution equation for the phase variable reads

$$\boldsymbol{\sigma} := g(\phi) \frac{\partial \psi_0}{\partial \boldsymbol{\varepsilon}} \quad \text{and} \quad M\dot{\phi} = -\frac{\delta \psi}{\delta \phi}, \tag{3.34}$$

where M is the dynamic modulus.

Almost in the meantime, another phase-field model based on Griffith's theory was independently developed by scientists with more mechanical backgrounds. Based on the variational principle, the fracture process is governed by minimising the energy functional

$$F(\boldsymbol{\varepsilon},\,\phi) = \int_{\Omega} g(\phi)\,\psi_0(\boldsymbol{\varepsilon})\,\mathrm{d}\,v + G_c \int_{\partial\Omega} \Gamma(\phi)\,\mathrm{d}\,a, \tag{3.35}$$
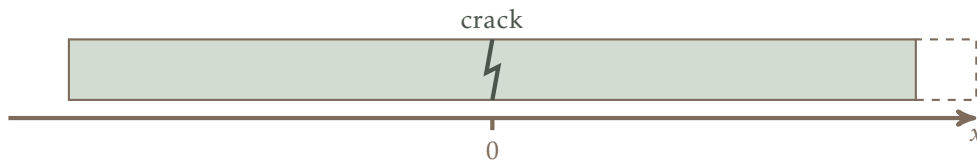
Figure 3.8: *A one-dimensional bar with a crack in the middle under elongation.*

where the first term represents an elastic energy density degrading with an evolution of ϕ while the second term, denoting the surface energy, increases. In order to avoid the divergence and instability in the numerical implementation, an artificial residual stiffness coefficient η_r is added into the degrading function g to prevent the zero-stiffness and the resulting singular stiffness matrix. According to the definition in (3.31), the most common form of g is given by

$$g = [(1 - \phi)^2 + \eta_r],\tag{3.36}$$

which fulfils the condition in (3.33). If the elastic potential energy and surface energy is chosen in a proper way, the phase-field model proves to be consistent with the classical Griffith theory, cf. Kuhn & Müller [135]. Herein, an example based on isotropic material behaviour is proposed with the linearised elastic stored energy

$$\psi_0 := \frac{1}{2}\boldsymbol{\varepsilon} \cdot (\overset{4}{\mathbf{C}}\boldsymbol{\varepsilon}),\tag{3.37}$$

and the phase-field-dependent coefficient

$$\Gamma := \frac{1}{\epsilon}\phi^2 + \epsilon\,|\mathrm{grad}\,\phi|^2.\tag{3.38}$$

where $\overset{4}{\mathbf{C}}$ denotes a linearised elastic stiffness tensor, and ϵ is the smear crack width or the length-scale parameter. In addition, the evolution equation of the phase variable ϕ reads

$$M\dot{\phi} = 2(1 - \phi)\psi_0 + \frac{G_c}{\epsilon}(\phi - \epsilon^2 \mathrm{div}\,\mathrm{grad}\,\phi).\tag{3.39}$$

In order to understand the physical meaning of the above equation, a simple one-dimensional model is considered. Therefore, assume that a bar with a crack in the middle is elongated, see Figure 3.8. Then, the bar will be divided into two parts, and no strain will occur in both pieces as a response to the disappearing resistance. Following this, the evolution equation (3.39) for a quasi-static case will be reduced to

$$\phi - \epsilon^2 \mathrm{div}\,\mathrm{grad}\,\phi = 0,\tag{3.40}$$

since $(1 - \phi)$ is zero for the cracked part and $\psi = 0$ for the intact but no strain part, which eliminates the first term of the right side of this equation. Solving this ordinary differential equation yields

$$\phi = \Lambda e^{-\frac{|x|}{\epsilon}},\tag{3.41}$$
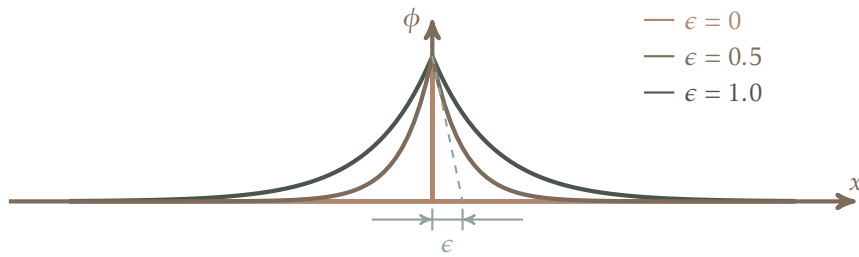
Figure 3.9: *The distribution for ϕ of a one-dimensional bar of a crack in the middle regarding different length scales.*

where $\Lambda = 1$ should be found by fulfilling the boundary condition, $\phi(x = 0) = 1$ for a crack in the middle. Insertion of this solution into the energy functional gives

$$F = G_c \int_{-l}^{l} \frac{1}{\epsilon} \phi^2 + \epsilon \,|\mathrm{grad}\,\phi|^2 \mathrm{d}\,x = G_c(2 - 2e^{-\frac{2l}{\epsilon}}). \tag{3.42}$$

If the extreme case $\epsilon \to 0$ is considered, the energy functional is found to be one half of Griffith's critical energy-release rate $\mathcal{G}_c$. By plotting (3.41) in Figure 3.9, it is clearly concluded that the length scale parameter ϵ controls the width of the smeared crack. When it approaches zero, a sharp crack (a jump) occurs.

Chapter 4:
Constitutive Settings for a Fracturing biphasic Material

This chapter formulates the constitutive equations for fracturing biphasic materials based on the derived *Clausius-Planck* inequality, cf. (2.58). In order to simplify the problem, several reasonable assumptions are introduced in Section 4.1 at first. Then, the *Clausius-Planck* inequality, together with the balance equations for mass and momentum, are reformulated to obtain the requirements for the constitutive equations. In Section 4.3, a new concept, namely the Crack-Opening Indicator (COI), is suggested to enhance the model for tackling more complex conditions, e. g. pre-cracked materials or cyclic loading cases. So as to further simplify the derived model, a geometrical linearisation is applied in Section 4.4. After a brief introduction of the spectral decomposition of the solid strain tensor in Section 4.4.2, the constitutive equations for the solid and the fluid are postulated in Sections 4.4.3 and 4.4.4, respectively.

4.1 Preliminaries

Strata are usually composed of solid matters, e. g. organic matter and minerals, liquid matter, e. g. underground water and oil, and gas matter, e. g. methane. However, when developing the constitutive equations for a typical hydraulic fracturing process, the dominant composites can be reduced to the solid skeleton and pore fluid, denoted by S and F, respectively. Correspondingly, the solidity and porosity are defined by their volume fractions,

$$\alpha := \begin{cases} S & \text{for solid,} \\ F & \text{for fluid.} \end{cases} \quad \text{and} \quad \begin{cases} n^S, & \text{solidity} \\ n^F, & \text{porosity.} \end{cases}$$

For the solid, the displacement $\mathbf{u}_S$ is usually chosen as the primary variable,

$$\mathbf{u}_S := \mathbf{x} - \mathbf{X}_S, \tag{4.1}$$

while for the fluid, the velocity is preferred due to the fact that the referential position of the fluid $\mathbf{X}_F$ is usually unknown. In addition, the seepage velocity $\mathbf{w}_F$ is introduced as the difference between the fluid and solid velocities such that the motion of the fluid can be easily expressed in relation to the solid motion, which is also called the modified *Euler*[1]ian setting.

$$\mathbf{w}_F := \mathbf{v}_F - \mathbf{v}_S. \tag{4.2}$$

After choosing the solid displacement to be the primary variable, the deformation gradient and its inverse are reformulated as

$$\mathbf{F}_S = \text{Grad}_S\left(\mathbf{X}_S + \mathbf{u}_S\right) = \mathbf{I} + \text{Grad}_S\mathbf{u}_S \quad \text{and} \quad \mathbf{F}_S^{-1} = \text{grad}\left(\mathbf{x} - \mathbf{u}_S\right) = \mathbf{I} - \text{grad}\,\mathbf{u}_S. \tag{4.3}$$

---

[1] *Leonhard Euler* (1707-1783): Swiss mathematician, physicist, astronomer, logician and engineer.

Recalling (2.3), the saturation condition is given by

$$\sum_\alpha n^\alpha = n^S + n^F = 1. \tag{4.4}$$

In hydraulics, the fluid is usually considered as an incompressible material. The solid skeleton can also be regarded as materially incompressible in an isothermal process due to the fact that the change of the real density is negligible compared to the bulk density change. Hence, for a hydraulic fracturing model, the real densities for both constituents are assumed constant:

$$\rho^{\alpha R} = \text{const.} \tag{4.5}$$

As there is no exchange between the solid and fluid constituents, the mass production term is always absent, viz.:

$$\hat{\rho}^\alpha \equiv 0. \tag{4.6}$$

While using the phase-field model to describe the fracture process, the phase variable needs to be defined. Herein, it is defined as

$$\phi^S = \begin{cases} 0 \text{ for intact material,} \\ 1 \text{ for fully cracked material.} \end{cases} \tag{4.7}$$

When solving a general continuum-mechanical Initial-Boundary-Value problem (IBVP), the total state of certain quantities is assumed to be known. These quantities usually include but not limited to motion and temperature, volume fractions and densities. Besides, the initial values of some quantities are also given, e. g. the initial densities and the initial volume fractions. The other quantities, which can not be derived directly by either the above-mentioned quantities or the balance relations, are called the response functions $\mathcal{R}$, cf. Ehlers [70]. For example, the *Helmholtz* free energy and the *Cauchy* stress tensor can be summarised into the response functions. It is straightforward to conclude that the response functions are governed by a set of independent process variables $\mathcal{V}$. The insertion of this dependency of $\mathcal{R}$ on $\mathcal{V}$ into the entropy inequality helps to define appropriate constitutive equations. However, before determining the dependency between $\mathcal{R}$ and $\mathcal{V}$, the fundamental thermodynamical principles, namely the principles of *determinism, equipresence, local action, material frame-indifference* and *dissipation*, have to be introduced at first. Note in passing that these principles guarantee the thermodynamical consistency, which a physical material model is supposed to satisfy. The principle of *determinism* restricts the undetermined response functions to be uniquely defined by the given $\mathcal{V}$, which excludes the randomness of the response functions at any time t and any positions $\mathbf{x}$. Following the principle of *equipresence*, the response functions $\mathcal{R}$ depends on the whole basic set of the variables $\mathcal{V}$, which includes not only the current state but also the history information. However, the choice of the variable set is not unique. For the so-called *first-grade* or *simple* material, it is assumed that the response functions for the material point P are dependent on itself, e. g. $\mathbf{x}$, and its immediate neighbourhood, e. g. $\mathbf{F}_S$ ($\text{Grad}_S \mathbf{x}$). This assumption is also known as the principle of *local action*. In contrast, the *second-grade* material considers additional gradient terms besides the basic variables, for example, $\text{Grad}_S \mathbf{F}_S$. For a multiphasic material, this second-gradient term $\text{Grad}_S \mathbf{F}_S$

can be excluded from the process variables $\mathcal{V}$ because it is only related to the production terms, cf. Bowen [41]. More discussion regarding this issue is referred to Ehlers [62, 70]. The principle of *material frame-indifference* is also called *material objectivity*, which states that the proposed constitutive equations should always be objective, cf. Noll [165, 166]. For example, when the observer moves in the space, the scalar quantity (e. g. the *Helmholtz* free energy) is invariant. According to the principle of *dissipation*, any thermodynamic processes are admissible only if the entropy inequality is fulfilled. Apart from these above-mentioned basic principles, Ehlers introduced the principle of *phase separation* in [70], which was originally named after "principle of constituent separation". This principle states that the free energy of each individual constituent only depends on the state variable of the concerned constituent and not of the overall aggregate. Following this, the *Helmholtz* free energy for the solid is considered as a function of the solid deformation gradient $\mathbf{F}_S$ or its equivalent substituent, the *Green-Lagrange*an strain tensor $\mathbf{E}_S$. Additionally, a phase variable ϕ^S, together with its material gradient $\mathrm{Grad}_S \phi^S$ also plays a role when the phase-field model is applied for describing the fracture process. For the fluid, the energy can be considered as a constant in the absence of the thermal effects. To summarise, the following dependencies are given,

$$\psi^S = \psi^S(\mathbf{F}_S, \phi^S, \mathrm{Grad}_S \phi^S) = \psi^S(\mathbf{E}_S, \phi^S, \mathrm{Grad}_S \phi^S) \quad \text{and} \quad \psi^F = \psi^F(-). \tag{4.8}$$

4.2 Reformulation of Balance Relations and *Clausius-Planck* Inequality

As a direct result of the material incompressibility assumption (4.5) and vanishing mass production terms (4.6), the mass balance is reduced to the volume balance,

$$(n^\alpha)'_\alpha + n^\alpha \operatorname{div} \overset{'}{\mathbf{x}}_\alpha = 0. \tag{4.9}$$

Hence, the time derivative of the volume fraction is given by

$$(n^\alpha)'_\alpha = -n_)^\alpha \operatorname{div} \overset{'}{\mathbf{x}}_\alpha. \tag{4.10}$$

By reformulating (2.19), the volume fraction of the constituent α is given by

$$n^\alpha = n^\alpha (\det \mathbf{F}_\alpha)^{-1}. \tag{4.11}$$

Due to the saturation condition in (4.4), it is deduced that the temporal change of the sum of the volume fractions is zero. Hence, if this change is with respect to the solid deformation, the following equation is derived, viz.:

$$\left(\sum_\alpha n^\alpha\right)'_S = (n^S + n^F)'_S = 0. \tag{4.12}$$

If one consider this equation as an additional condition and multiply it with a *Lagrange* multiplier (i. e. the pore pressure p), an extended form for the *Clausius-Planck* inequality for the overall aggregate will be written as

$$\sum_\alpha [\, \mathbf{T}^\alpha \cdot \mathbf{L}_\alpha - \rho^\alpha (\psi^\alpha)'_\alpha - \hat{\mathbf{p}}^\alpha \cdot \overset{'}{\mathbf{x}}_\alpha] + p \left(\sum_\alpha n^\alpha\right)'_S \geq 0 \tag{4.13}$$

With the following relation

$$(n^F)'_F = (n^F)'_S + \operatorname{grad} n^F \cdot \mathbf{w}_F, \tag{4.14}$$

(4.12) leads to

$$n^S \operatorname{div} \mathbf{v}_S + n^F \operatorname{div} \mathbf{v}_F + \operatorname{grad} n^F \cdot \mathbf{w}_F = 0. \tag{4.15}$$

As no mass production occurs, the additional momentum production also vanishes. Then, the sum of the direct momentum production is equal to the total momentum production, which also vanishes:

$$\hat{\mathbf{p}}^S + \hat{\mathbf{p}}^F = \mathbf{0}. \tag{4.16}$$

Since the *Cauchy* stress is a symmetric tensor, cf. (2.49), the stress power $\mathbf{T}^\alpha \cdot \mathbf{L}_\alpha$ can be rewritten by

$$\mathbf{T}^\alpha \cdot \mathbf{L}_\alpha = \mathbf{T}^\alpha \cdot \mathbf{D}_\alpha. \tag{4.17}$$

Insertion of (4.15), (4.16) and (4.17) into (4.13) yields

$$\mathbf{T}_E^S \cdot \mathbf{D}_S - \rho^S (\psi^S)'_S + \mathbf{T}_E^F \cdot \mathbf{D}_F - \rho^F (\psi^F)'_F - \hat{\mathbf{p}}_E^F \cdot \mathbf{w}_F \geq 0, \tag{4.18}$$

where the subscript E denotes an extra or effective term:

$$\mathbf{T}_E^S := \mathbf{T}^S + n^S p \, \mathbf{I}, \quad \mathbf{T}_E^F := \mathbf{T}^F + n^F p \, \mathbf{I} \quad \text{and} \quad \hat{\mathbf{p}}_E^F := \hat{\mathbf{p}}^F - p \operatorname{grad} n^F. \tag{4.19}$$

Proceeding from (4.8), the material time derivatives of the *Helmholtz* free energy for the solid and the fluid are given by

$$(\psi^S)'_S = \frac{\partial \psi^S}{\partial \mathbf{E}_S} \cdot (\mathbf{E}_S)'_S + \frac{\partial \psi^S}{\partial \phi^S} (\phi^S)'_S + \frac{\partial \phi^S}{\partial \operatorname{Grad}_S \phi^S} \cdot \operatorname{Grad}_S (\phi^S)'_S \quad \text{and} \quad (\psi^F)'_F = 0, \tag{4.20}$$

respectively. Applying the divergence theorem to the last term of the first time derivative for the solid yields

$$\frac{\partial \phi^S}{\partial \operatorname{Grad}_S \phi^S} \cdot \operatorname{Grad}_S (\phi^S)'_S = \operatorname{Div}_S \left[(\phi^S)'_S \frac{\partial \phi^S}{\partial \operatorname{Grad}_S \phi^S} \right] - (\phi^S)'_S \operatorname{Div}_S \left(\frac{\partial \psi^S}{\partial \operatorname{Grad}_S \phi^S} \right). \tag{4.21}$$

Moreover, the stress power may take the form

$$\mathbf{T}^\alpha \cdot \mathbf{D}_\alpha = \left[(\det \mathbf{F}_\alpha)^{-1} \mathbf{F}_\alpha \mathbf{S}^\alpha \mathbf{F}_\alpha^T \right] \cdot \left[\mathbf{F}_\alpha^{T-1} (\mathbf{E}_\alpha)'_\alpha \mathbf{F}_\alpha^{-1} \right] = (\det \mathbf{F}_\alpha)^{-1} \mathbf{S}^\alpha \cdot (\mathbf{E}_\alpha)'_\alpha, \tag{4.22}$$

which is reformulated in the referential configuration. With (4.21) and (4.22) at hand, the inequality in (4.18) is then rewritten as

$$(\det \mathbf{F}_S)^{-1} (\mathbf{S}_E^S - \rho_0^S \frac{\partial \psi^S}{\partial \mathbf{E}_S}) \cdot (\mathbf{E}_S)'_S - \rho^S \left[\frac{\partial \psi^S}{\partial \phi^S} - \operatorname{Div}_S \left(\frac{\partial \psi^S}{\partial \operatorname{Grad}_S \phi^S} \right) \right] (\phi^S)'_S -$$

$$- \rho^S \operatorname{Div}_S \left[(\phi^S)'_S \frac{\partial \phi^S}{\partial \operatorname{Grad}_S \phi^S} \right] + \mathbf{T}_E^F \cdot \mathbf{D}_F - \hat{\mathbf{p}}_E^F \cdot \mathbf{w}_F \geq 0. \tag{4.23}$$

In order to fulfil this inequality, one may decompose it into the equilibrium parts, which vanishes finally, and the non-equilibrium (dissipation) parts, which are required to be

non-negative.

Equilibrium parts:

$$(\det \mathbf{F}_S)^{-1}(\mathbf{S}_E^S - \rho_0^S \frac{\partial \psi^S}{\partial \mathbf{E}_S}) \cdot (\mathbf{E}_S)'_S = \mathbf{0} \quad \rightarrow \quad \mathbf{S}_E^\alpha = \rho_0^S \frac{\partial \psi^S}{\partial \mathbf{E}_S} \tag{4.24}$$

$$\rho^S \operatorname{Div}_S \left[(\phi^S)'_S \frac{\partial \phi^S}{\partial \operatorname{Grad}_S \phi^S} \right] = 0 \tag{4.25}$$

Non-equilibrium (dissipation) parts:

$$-\rho^S \left[\frac{\partial \psi^S}{\partial \phi^S} - \operatorname{Div}_S \left(\frac{\partial \psi^S}{\partial \operatorname{Grad}_S \phi^S} \right) \right] (\phi^S)'_S \geq 0$$

$$\rightarrow \quad (\phi^S)'_S \propto -\rho^S \left[\frac{\partial \psi^S}{\partial \phi^S} - \operatorname{Div}_S \left(\frac{\partial \psi^S}{\partial \operatorname{Grad}_S \phi^S} \right) \right] \tag{4.26}$$

$$\mathbf{T}_E^F \cdot \mathbf{D}_F \geq 0 \rightarrow \mathbf{T}_E^F \propto \mathbf{D}_F \tag{4.27}$$

$$-\hat{\mathbf{p}}_E^F \cdot \mathbf{w}_F \geq 0 \rightarrow \hat{\mathbf{p}}_E^F \propto -\mathbf{w}_F \tag{4.28}$$

For the equilibrium part, the first equation is a standard relation in the small-strain elasticity due to the fact that for an arbitrary strain rate $(\mathbf{E}_S)'_S$, the entropy production should be zero in a non-dissipative process. The second equation is more or less considered as the continuity equation for the vector term in the bracket, and its realisation is done by integrating the term over the whole domain. By applying the *Gauss*[2] integral theorem, this volume-specific integral term can be equivalently transformed to a surface integral as

$$\int_\Omega \rho^S \operatorname{Div}_S \left[(\phi^S)'_S \frac{\partial \phi^S}{\partial \operatorname{Grad}_S \phi^S} \right] \mathrm{d}v = \int_\Omega \rho_0^S \operatorname{Div}_S \left[(\phi^S)'_S \frac{\partial \phi^S}{\partial \operatorname{Grad}_S \phi^S} \right] \mathrm{d}V_\alpha$$

$$= \int_{\partial\Omega} \rho_0^S (\phi^S)'_S \frac{\partial \phi^S}{\partial \operatorname{Grad}_S \phi^S} \cdot \mathbf{n}\,\mathrm{d}A_\alpha, \tag{4.29}$$

where Ω is an arbitrary volume bounded by its surface $\partial\Omega$ with an outward-oriented unit normal vector $\mathbf{n}$. If the equation holds for any closed surface, the integrant must be perpendicular to the unit normal $\mathbf{n}$:

$$\rho_0^S \frac{\partial \phi^S}{\partial \operatorname{Grad}_S \phi^S} \cdot \mathbf{n} = 0. \tag{4.30}$$

This equation will later be applied as the boundary condition for the phase-variable evolution in the numerical implementation, cf. (4.58).

---

[2] *Carl Friedrich Gauss* (1777-1855): German mathematician and physicist.

4.3   Crack-Opening Indicator (COI)

Before postulating the constitutive equations for the dissipative parts, one may concern the fact that for a hydraulic fracturing process, the stratum is usually imperfect, where pre-cracks exist. Furthermore, there are confining stresses in the deep-buried stratum due to the weight of the strata above it. These stresses are also known as the geological stresses which squeeze the cracked stratum together. In such cases, the porous material behaves in a manner of an intact one despite the existence of the pre-cracks until the loadings, e. g. injection of the fracking fluid or the tension from the outside, pull them apart, where the pre-cracks are again open. Proceeding from this finding, one concludes that it is not enough to determine the state of a crack (whether a crack is open or closed) and the state of a fluid in the crack zone (whether the flow type is a *Darcy*'s[3] filter flow or a *Navier*[4]-*Stokes* [5] free flow) only by the phase variable (that distinguishes the cracked material from the intact one) . In order to conquer this drawback, a new variable, the COI, is then introduced as,

$$\mathcal{I} = \begin{cases} 1, \text{ if a crack opening is possible,} \\ 0, \text{ else.} \end{cases} \tag{4.31}$$

Particular emphasis is placed on the fact that like the phase variable, this COI alone is unable to determine whether there is an open crack or not. According to the definition, when $\mathcal{I} = 1$, two extreme states exist, namely intact solid ($\phi^S = 1$) and cracked material ($\phi^S = 0$) with an open crack. Analogously, for $\mathcal{I} = 0$, corresponding states refer to an intact solid ($\phi^S = 1$) and a cracked solid ($\phi^S = 0$) with a closed crack. In order to investigate a proper criterion for the COI, the following case is considered as shown in Figure 4.1. A one-dimensional bar (of length l) with a crack in the middle is under consideration, and a displacement of Δl is enforced on the right side. Two possible deformations are given as (b) and (c). In the first case, the extension occurs in the middle, at the pre-existing crack, while the rest remains unchanged. For the second case, the whole bar is extended evenly along the length, and the strain throughout the bar is $\Delta l/l$. With (4.4) and (4.11) at hand, the porosity is related to the solid strain by

$$n^F = 1 - n^S = 1 - n_0^S \left(1 + \varepsilon_1\right)^{-1}. \tag{4.32}$$

It is easy to find that in the first case, the porosity is a constant for these two separate parts while for the second case, the porosity is increased by $n_0^S \frac{\Delta l}{\Delta l + l}$. However, due to the existence of the crack, an additional restriction has to be fulfilled that the cracked material can bear no tensile stress. Hence, the second case is unrealistic for the given displacement. In other words, once there is a crack in a one-dimensional setting, an increasing porosity is always much more easily achieved by opening the crack than by enlarging the pores since there is no resistance against tension in the cracked material.

---

[3] *Henry Philibert Gaspard Darcy* (1803-1858): French engineer.
[4] *Claude Louis Marie Henri Navier* (1785-1863): French French engineer and physicist.
[5] *George Gabriel Stokes* (1819-1903): Irish physicist and mathematician.
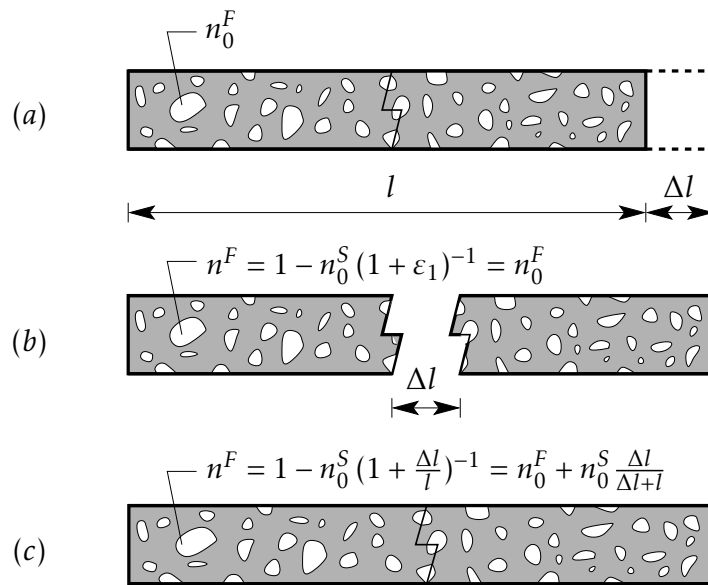
Figure 4.1: *(a) geometry and boundary conditions for a one-dimensional hydraulic fracturing problem (b, c) possible responses to the given displacement*

Based on this understanding, the COI is then defined via the porosity change as,

$$
\mathcal{I} = \begin{cases} 1: \text{for increasing porosity } n^F > n_0^F \ , \\ \\ 0: \text{for decreasing or constant porosity } n^F \leq n_0^F \ . \end{cases}
\tag{4.33}
$$

The detailed definition of the COI in this monograph will be given in the following section, cf. (4.40), where a geometrical linearisation with respect to the solid deformation is applied. The COI, together with the extreme value of the phase variable, defines four states for each material point P, see Table 4.1. It is apparent that for $\phi^S = 0$, no matter if the porosity increases (State I) or decreases (State II), the fluid flows compliant with *Darcy*'s filter law since the solid skeleton is intact. However, for a fractured porous media, the fluid flow is governed by the *Navier-Stokes* equation in an open crack (State IV) while tends to be a filter flow if the crack is closed again (State III).

state	ϕ^S	$\mathcal{I}$	description	flow type
I	0	0	intact solid with reducing pores	*Darcy*
II	0	1	intact solid with enlarging pores	*Darcy*
III	1	0	fractured solid with closed cracks	*Darcy*
IV	1	1	fractured solid with open cracks	*Navier-Stokes*

Table 4.1: *Four states of porous media in hydraulic fracturing categorised using ϕ^S and $\mathcal{I}$*

4.4 Constitutive Relations

4.4.1 Geometrical linearisation

From a mathematical point of view, an arbitrary function Ψ can be represented by the sum of an infinite number of terms that are computed from the function and its derivatives at a single point $\mathbf{x}_0$. This function decomposition is also called *Taylor*'s[6] expansion or *Taylor* series, viz.

$$\Psi(\mathbf{x}) = \Psi_0(\mathbf{x}_0) + \left.\frac{\mathrm{d}}{\mathrm{d}\,\mathbf{x}}\Psi\right|_{\mathbf{x}=\mathbf{x}_0} \cdot (\mathbf{x}-\mathbf{x}_0) + \left.\frac{\mathrm{d}^2}{\mathrm{d}\,\mathbf{x}^2}\Psi\right|_{\mathbf{x}=\mathbf{x}_0} \cdot [(\mathbf{x}-\mathbf{x}_0)\otimes(\mathbf{x}-\mathbf{x}_0)] + \mathcal{O}(\mathbf{x}^3) \quad (4.34)$$

For practical reasons, if the higher order terms are sufficiently small, for example,

$$|\mathbf{x}-\mathbf{x}_0|^2 \approx 0, \tag{4.35}$$

the function can be approximated by the sum of the local value and the terms related to its first-order derivative. This simplification is also called a geometrical linearisation and commonly adopted in geomechanics, which helps to reduce the complexity not only of the model formulation but also of the numerical implementation. Therefore,

$$\Psi(\mathbf{x}) \approx \mathrm{lin}\,\Psi(\mathbf{x}) := \Psi_0(\mathbf{x}_0) + \left.\frac{\mathrm{d}}{\mathrm{d}\,\mathbf{x}}\Psi\right|_{\mathbf{x}=\mathbf{x}_0} \cdot (\mathbf{x}-\mathbf{x}_0) \tag{4.36}$$

In this context, a simplification is applied regarding the solid displacement such that the following equations hold, viz.

$$
\begin{aligned}
&\mathrm{Grad}_S(\cdot) \approx \mathrm{grad}\,(\cdot) & &\boldsymbol{\varepsilon}_S := \mathrm{lin}\,\mathbf{E}_S = \frac{1}{2}(\mathrm{grad}\,\mathbf{u}_S + \mathrm{grad}^T\,\mathbf{u}_S)\\[2mm]
&\mathrm{Div}_S(\cdot) \approx \mathrm{div}\,(\cdot) & &\boldsymbol{\sigma}^S := \mathrm{lin}\,\mathbf{T}^S = \mathrm{lin}\,\boldsymbol{\tau}^S = \mathrm{lin}\,\mathbf{P}^S = \mathrm{lin}\,\mathbf{S}^S\\[2mm]
&J_S \approx 1 + \mathrm{div}\,\mathbf{u}_S & &\mathbf{D}_F \approx \frac{1}{2}\,(\,\mathrm{grad}\,\mathbf{v}_F + \mathrm{grad}^T\,\mathbf{v}_F\,)\\[2mm]
&(J_S)^{-1} \approx 1 - \mathrm{div}\,\mathbf{u}_S & &\boldsymbol{\sigma}^S = \rho_0^S\,\frac{\partial\psi^S}{\partial\boldsymbol{\varepsilon}_S}
\end{aligned}
\tag{4.37}
$$

Recalling (4.11), one can derive

$$n^S = n_0^S(\det\mathbf{F}_S)^{-1} \approx n_0^S(1 - \mathrm{div}\,\mathbf{u}_S). \tag{4.38}$$

Insertion of the above relation into $n^F = 1 - n^S$, one derives

$$n^F = 1 - n_0^S(1 - \mathrm{div}\,\mathbf{u}_S) = \underbrace{1 - n_0^S}_{n_0^F} + n_0^S\,\mathrm{div}\,\mathbf{u}_S = n_0^F + n_0^S\,\mathrm{div}\,\mathbf{u}_S. \tag{4.39}$$

---

[6] *Brook Taylor* (1685-1731): English mathematician.

Based on this equation, it is apparent that if the term, $\operatorname{div} \mathbf{u}_S$, is positive, the porosity n^F will increase and vice versa. Regarding (4.33), the COI can be defined as

$$
\mathcal{I} = \begin{cases} 1: \text{ for } \operatorname{div} \mathbf{u}_S > 0 \,, \\[2ex] 0: \text{ for } \operatorname{div} \mathbf{u}_S \leq 0 \,. \end{cases} \tag{4.40}
$$

For a geometrically linearised model, if the load is applied under a moderate velocity, the seepage velocity $\mathbf{w}_F$ is supposed to be very small, and as a consequence, the higher-order terms of $(\operatorname{grad} \mathbf{v}_F)\mathbf{w}_F$ are negligible, cf. Zienkiewicz et al. [209]. Therefore, when computing the material time derivative of the fluid velocity, the convection term is omitted, i.e.

$$
(\mathbf{v}_F)'_F = (\mathbf{v}_F)'_S + \operatorname{grad} \mathbf{v}_F \mathbf{w}_F \approx (\mathbf{v}_F)'_S \tag{4.41}
$$

For a detailed derivation of relations under a geometrically linearised setting, one may compare the works of Ehlers [76], Eipper [77], Markert [146] and Karajan [129].

4.4.2 Spectral decomposition of solid strain

In continuum mechanics, a decomposition is often applied to the deformation tensors, e. g. the polar decomposition of the deformation gradient, such that different deformation modes are distinguished from one another. Herein, considering the symmetry of the geometrically linearised strain tensor $\boldsymbol{\varepsilon}_S$, the spectral decomposition is adopted. Notwithstanding the importance of the decompositions of the deformation tensors in postulating the constitutive equations, only a brief but a necessary introduction is given in this section. For further interest in this topic, one may compare, e. g. Lambrecht [138], Markert [146] and the references therein. According to the definition of the spectral decomposition, an arbitrary symmetric tensor can be expressed by the sum of the multiplication of its eigenvalues and the dyadic productions of its corresponding vectors, or in other words, its eigentensors. For the geometrically linearised strain tensor $\boldsymbol{\varepsilon}_S$, it reads

$$
\boldsymbol{\varepsilon}_S = \sum_{i=1}^{3} \lambda_{Si} \mathbf{n}_{Si} \otimes \mathbf{n}_{Si} = \sum_{i=1}^{3} \lambda_{Si} \mathbf{M}_{Si}. \tag{4.42}
$$

where $\mathbf{M}_{Si}$ denotes the eigentensor and the eigenvalues λ_{Si} and eigenvector $\mathbf{n}_{Si}$ must satisfy the following equation,

$$
(\boldsymbol{\varepsilon}_S - \lambda_{Si}\mathbf{I})\mathbf{n}_{Si} = \mathbf{0} \tag{4.43}
$$

with the condition $\mathbf{n}_{Si} \neq \mathbf{0}$. To calculate the eigenvalues, one may apply the *Cayley*[7]-*Hamilton*[8] theorem, which states that the eigenvalues make the associated characteristic polynomial zero,

$$
\det (\boldsymbol{\varepsilon}_S - \lambda_S\mathbf{I}) = \lambda_S^3 - I_{S1}\lambda_S^2 + I_{S2}\lambda_S - I_{S3} = 0, \tag{4.44}
$$

---

[7] *Arthur Cayley* (1821-1895): British mathematician.
[8] *William Rowan Hamilton* (1805-1865): Irish mathematician, physicist and astronomer.

the principal invariants of which are defined as

$$I_{S1} = \operatorname{tr}\boldsymbol{\varepsilon}_S = \boldsymbol{\varepsilon}_S \cdot \mathbf{I},$$

$$I_{S2} = \operatorname{tr}(\operatorname{cof}\boldsymbol{\varepsilon}_S) = \tfrac{1}{2}[(\operatorname{tr}\boldsymbol{\varepsilon}_S)^2 - \operatorname{tr}(\boldsymbol{\varepsilon}_S\boldsymbol{\varepsilon}_S)], \qquad (4.45)$$

$$I_{S3} = \det\boldsymbol{\varepsilon}_S.$$

It is worth mentioning that the principal invariants are related to the eigenvalues by

$$I_{S1} = \lambda_{S1} + \lambda_{S2} + \lambda_{S3},$$

$$I_{S2} = \lambda_{S1}\lambda_{S2} + \lambda_{S2}\lambda_{S3} + \lambda_{S1}\lambda_{S3}, \qquad (4.46)$$

$$I_{S3} = \lambda_{S1}\lambda_{S2}\lambda_{S3}.$$

Furthermore, the derived eigenvectors $\mathbf{n}_{Si}$ form one set of orthogonal coordinates, mathematically speaking,

$$\mathbf{n}_{Si} \cdot \mathbf{n}_{Sj} = \delta_{ij}, \qquad (4.47)$$

where δ_{ij} is the *Kronecker*[9] Delta:

$$\delta_{ij} = \begin{cases} 1, & \text{for } i = j, \\ 0, & \text{for } i \neq j. \end{cases} \qquad (4.48)$$

. As a result, the sum of the eigentensors $\mathbf{M}_{Si}$ yields the identity tensor,

$$\sum_{i=1}^{3} \mathbf{M}_{Si} = \mathbf{I} \quad \text{with} \quad \mathbf{M}_{Si} = \mathbf{n}_{Si} \otimes \mathbf{n}_{Si}. \qquad (4.49)$$

More properties of the eigentensor $\mathbf{M}_{Si}$ are including but not limited to

$$(\mathbf{M}_{Si})^n = \mathbf{M}_{Si} \qquad ; \quad \mathbf{M}_{Si}\mathbf{M}_{Sj} = \mathbf{0} \text{ for } i \neq j$$

$$\boldsymbol{\varepsilon}_S\mathbf{M}_{Si} = \mathbf{M}_{Si}\boldsymbol{\varepsilon}_S = \lambda_{Si}\mathbf{M}_{Si} \quad ; \quad \mathbf{M}_{Si}\mathbf{M}_{Sj} = \delta_{ij}.$$

In order to solve the balance equations by a numerical method iteratively, as discussed later in Chapter 5.2.2, the consistent tangent is required, cf. Chapter 5.3. Here, several preliminary derivatives are given,

$$\frac{\partial \lambda_{Si}}{\partial \boldsymbol{\varepsilon}_S} = \mathbf{M}_{Si}$$

$$\frac{\partial \mathbf{M}_{Si}}{\partial \boldsymbol{\varepsilon}_S} = \frac{1}{2}\sum_{j=1,\,j\neq i}^{3} \frac{1}{\lambda_{Si} - \lambda_{Sj}}[(\mathbf{M}_{Si} \otimes \mathbf{M}_{Sj})^{\overset{23}{T}} + (\mathbf{M}_{Si} \otimes \mathbf{M}_{Sj})^{\overset{24}{T}} + \qquad (4.50)$$

$$+ (\mathbf{M}_{Sj} \otimes \mathbf{M}_{Si})^{\overset{23}{T}} + (\mathbf{M}_{Sj} \otimes \mathbf{M}_{Si})^{\overset{24}{T}}] =: \overset{4}{\mathbb{M}}_{Si}.$$

---

[9] *Leopold Kronecker* (1823-1891): German mathematician.

Note that this equation only works for the case where three distinct eigenvalues exist. For the other cases (two or three equal eigenvalues), the eigenvectors for the corresponding eigenvalues are not unique. For example, if there are two equal eigenvalues, the corresponding eigenvectors can be two arbitrary orthogonal vectors which are located on the surface perpendicular to the third eigenvector. In this regard, the eigenvectors have to be set manually. Moreover, in this case, the denominator of the coefficient in (4.50), $\lambda_{Si} - \lambda_{Sj}$, is zero and no longer physical. When computing the mapping tensors in (5.33), modifications must be introduced to compute the limiting values which can be found by the rule of *de l'Hôspital*[10]. Relative derivation procedures can be found in the work of Miehe & Lambrecht [153].

In the work of Miehe et al. [155], the idea of decomposing the strain tensor according to the sign of the eigenvalues was firstly introduced. This stems from the observation that a crack is generated only due to tension but not to compression. To put it another way, the stiffness for the fractured material decreases only in the direction where tension is applied. Hence, it is persuasive to separate the strain tensor according to the sign of its eigenvalue, which actually measures the principal strain,

$$\boldsymbol{\varepsilon}_S^\pm := \sum_{i=1}^3 \frac{\lambda_{Si} \pm |\lambda_{Si}|}{2}\, \mathbf{M}_{Si} = \sum_{i=1}^3 (\lambda)_{Si}^\pm\, \mathbf{M}_{Si} \quad \text{with} \quad (\lambda)_{Si}^\pm := \frac{\lambda_{Si} \pm |\lambda_{Si}|}{2}, \qquad (4.51)$$

where the plus/minus superscripts denote that the tensor contains positive/negative principal strains. Based on these considerations, the solid stress energy, introduced in Section 4.4.3, is able to describe an anisotropic degradation of stiffness according to tension/compression stress directions.

4.4.3 Constitutive relations for the solid

In the work of Miehe et al. [155], the free energy for a pure solid was proposed. If combing the formulation suggested therein with (4.7), the *Helmholtz* free energy then takes the form,

$$\rho_0^S \psi^S(\boldsymbol{\varepsilon}_S, \phi^S, \operatorname{grad}\phi^S) = \left[(1-\phi^S)^2 + \eta_r^S\right] \rho_0^S \psi^{S+}(\boldsymbol{\varepsilon}_S^+) + \rho_0^S \psi^{S-}(\boldsymbol{\varepsilon}_S^-) +$$
$$+ G_c\, \Gamma^S(\phi^S, \operatorname{grad}\phi^S)\,, \qquad (4.52)$$

where

$$\rho_0^S \psi^{S+}(\boldsymbol{\varepsilon}_S^+) \qquad = \mu^S\,(\boldsymbol{\varepsilon}_S^+ \cdot \boldsymbol{\varepsilon}_S^+) + \frac{1}{2}\lambda^S[(\operatorname{tr}\boldsymbol{\varepsilon}_S)^+]^2\,,$$

$$\rho_0^S \psi^{S-}(\boldsymbol{\varepsilon}_S^-) \qquad = \mu^S\,(\boldsymbol{\varepsilon}_S^- \cdot \boldsymbol{\varepsilon}_S^-) + \frac{1}{2}\lambda^S[(\operatorname{tr}\boldsymbol{\varepsilon}_S)^-]^2\,, \qquad (4.53)$$

$$\Gamma^S(\phi^S, \operatorname{grad}\phi^S) = \frac{1}{2\epsilon}(\phi^S)^2 + \frac{\epsilon}{2}\operatorname{grad}\phi^S \cdot \operatorname{grad}\phi^S\,.$$

Herein, an additional definition is introduced by

$$(\operatorname{tr}\boldsymbol{\varepsilon}_S)^\pm = \frac{\operatorname{tr}\boldsymbol{\varepsilon}_S \pm |\operatorname{tr}\boldsymbol{\varepsilon}_S|}{2}. \qquad (4.54)$$

---

[10] *Guillaume de l'Hôpital* (1661-1704): French mathematician

Because η_r^S is introduced only due to a numerical consideration and it adds more or less an artificial stiffness to the solid skeleton. Hence, it should be chosen as small as possible provided that the computation is stable. The smeared crack length or the length-scale parameter is expressed by ϵ while μ^S and λ^S are the partial *Lamé*[11] constants. From (4.52), the total stress energy per referential bulk volume $\rho_0^S \psi^S$ consists of a tensile energy $\rho_0^S \psi^{S+}(\boldsymbol{\varepsilon}_S^+)$ with a factor $(1-\phi^S)^2 + \eta_r^S$, a compressive energy $\rho_0^S \psi^{S-}(\boldsymbol{\varepsilon}_S^-)$ and a crack energy $G_c \Gamma^S$. Thanks to the split of the strain tensor into a negative part and a positive one, the evolution of the phase variable reduces the storage stress energy only resulting from the positive principal strains instead of the total strains. In contrast, the compressive energy depends only on the solid deformation despite the phase variable. When the positive stress energy decreases, the fracture energy $G_c \Gamma^S$ grows with the increasing phase variable and its gradient.

By inserting the stress energy (4.52) into (4.37)$_8$, the linearised effective stress of the solid will take the form,

$$\boldsymbol{\sigma}_E^S = \rho_0^S \frac{\partial \psi^S}{\partial \boldsymbol{\varepsilon}_S}$$

$$= \left[(1 - \phi^S)^2 + \eta_r^S \right] \left[2\,\mu^S\,\boldsymbol{\varepsilon}_S^+ + \lambda^S\,(\operatorname{tr}\boldsymbol{\varepsilon}_S)^+\,\mathbf{I} \right] + 2\,\mu^S\,\boldsymbol{\varepsilon}_S^- + \lambda^S\,(\operatorname{tr}\boldsymbol{\varepsilon}_S)^-\,\mathbf{I}\,. \tag{4.55}$$

In order to fulfil the proportionality in (4.26), the simplest form is to set up a linear dependency via

$$(\phi^S)_S' = -\frac{1}{M}\left[\rho_0^S \frac{\partial \psi^S}{\partial \phi^S} - \operatorname{div}\left(\rho_0^S \frac{\partial \psi^S}{\partial \operatorname{grad}\phi^S} \right) \right], \tag{4.56}$$

where M is a mobility parameter and must have a non-negative value. In the work of Miehe et al. [155], it is concluded that a rate-independent process (an exclusion of the evolution term, $(\phi^S)_S'$, from (4.56) by setting $M = 0$) makes the numerical algorithm robust. In order to prevent the singularity of a zero-value denominator, the above equation is equivalently rewritten as

$$M(\phi^S)_S' = 2\,(1 - \phi^S)\,\rho_0^S \psi^{S+} - G_c\left(\frac{\phi^S}{\epsilon} - \epsilon\,\operatorname{div}\operatorname{grad}\phi^S \right). \tag{4.57}$$

With the given energy function at hand, the equilibrium in (4.30) holds if

$$G_c\,\epsilon\,\operatorname{grad}\phi^S \cdot \mathbf{n} = 0. \tag{4.58}$$

4.4.4 Constitutive relations for the fluid

Proceeding from the investigation of the entropy inequality and the introduction of the COI, the effective fluid stress is defined as

$$\mathbf{T}_E^F = 2\,\mathcal{I}\,(\phi^S)^2\,n^F \mu^{FR}\,\mathbf{D}_F\,, \tag{4.59}$$

---

[11] *Gabriel Lamé* (1795-1879): French mathematician.

where the effective dynamic viscosity of the pore fluid is denoted by μ^{FR} and the square of ϕ^S guarantees a non-negative value of the coefficient during the numerical computation. With this form, the fluid stress is equivalent to that of a *Newton*ian[12] fluid for the case when $\mathcal{I} = 1$ and $\phi^S = 1$, corresponding to an open crack. Meanwhile, an effective fluid momentum production given by

$$\hat{\mathbf{p}}_E^F = -\left[1 - \mathcal{I} + \mathcal{I}(1 - \phi^S)^2\right] \frac{(n^F)^2 \gamma^{FR}}{k^F} \mathbf{w}_F , \tag{4.60}$$

is vanishing. The hydraulic conductivity k^F is related to the intrinsic permeability K^S by the specific weight $\gamma^{FR} = \rho^{FR}|\mathbf{g}|$ via

$$k^F = \frac{\gamma^{FR}}{\mu^{FR}} K^S. \tag{4.61}$$

For an increasing porosity ($\mathcal{I} = 1$), the fluid momentum production decreases with the evolution of the phase variable, which corresponds to the fact that the accumulation of the micro-cracks decreases the resistance of the solid when the fluid penetrates the solid skeleton. In order to review the state of the fluid, its momentum balance is rewritten as

$$\rho^F(\mathbf{v}_F)_F' = \operatorname{div}(\mathbf{T}_E^F - p\,n^F\mathbf{I}) + \rho^F\mathbf{g} + (\hat{\mathbf{p}}_E^F + p\,\operatorname{grad} n^F). \tag{4.62}$$

Inserting the above constitutive relations into the balance equations and considering the extreme values of the phase variable and the COI, four corresponding states are obtained, cf. Table 4.2.

Table 4.2: *Review of the four states in Table 4.1*

state	ϕ^S	$\mathcal{I}$	$\mathbf{T}_E^F$	$\hat{\mathbf{p}}_E^F$	flow type
I	0	0	$\mathbf{0}$	$-\dfrac{(n^F)^2\gamma^{FR}}{k^F}\mathbf{w}_F$	*Darcy*
II	0	1	$\mathbf{0}$	$-\dfrac{(n^F)^2\gamma^{FR}}{k^F}\mathbf{w}_F$	*Darcy*
III	1	0	$\mathbf{0}$	$-\dfrac{(n^F)^2\gamma^{FR}}{k^F}\mathbf{w}_F$	*Darcy*
IV	1	1	$2\,n^F\mu^{FR}\mathbf{D}_F$	$\mathbf{0}$	*Navier-Stokes*

As shown above, the three states, I, II and III, correspond to the same state of the fluid. Rewriting the fluid momentum balance for these states under a creeping flow condition with $(\mathbf{v}_F)_F' \approx \mathbf{0}$ yields

$$n^F\mathbf{w}_F = -\frac{1}{\gamma^{FR}}k^F(\operatorname{grad} p - \rho^{FR}\mathbf{g}), \tag{4.63}$$

---

[12] *Sir Isaac Newton* (1642-1726/27): English mathematician, astronomer, theologian, author and physicist.

which is known as a standard form of *Darcy*'s law. For the open-crack case (corresponding to state IV), the balance is transformed into

$$\rho^F (\mathbf{v}_F)_F' = \operatorname{div}(2\mu^{FR} \mathbf{D}_F) - \operatorname{grad} p + \rho^F \mathbf{g}. \tag{4.64}$$

In comparison with the momentum balance of a single fluid, it agrees with the *Navier-Stoke*'s equation of an incompressible *Newton*ian fluid.

Chapter 5:
Numerical Treatment

This chapter follows the material model proposed in the above chapters and elaborates the numerical treatment. Firstly, three supplementary problems involving the strain energy of triggering fracture, the prevention of fracture from recovery and the realisation of pre-existing cracks are under study in Section 5.1. Subsequently, the strong and weak forms of the governing equations, as well as the spatial and temporal discretisation, are presented in Section 5.2. At last, the consistent tangent for an iteration method is computed in Section 5.3.

5.1 Specific Consideration Based on the Solid Fracturing Process

5.1.1 Threshold of fracturing

When describing the brittle fracture of a solid, one may expect a purely elastic behaviour until the first macro-crack is triggered by the accumulated strain energy. With this in mind, (4.57) shall be confined to

$$M(\phi^S)'_S \begin{cases} = 0, & \text{for } \rho_0^S \psi^{S+} \leq \Upsilon_t^S, \\ > 0, & \text{for } \rho_0^S \psi^{S+} > \Upsilon_t^S, \end{cases} \tag{5.1}$$

where Υ_t^S represents the so-called triggering strain energy when the fracture is initiated. Correspondingly, (4.57) is modified as

$$M(\phi^S)'_S = 2\,(1 - \phi^S)\,\Delta\rho_0^S \psi^{S+} - G_c\,(\frac{\phi^S}{\epsilon} - \epsilon\,\text{div grad}\,\phi^S) \tag{5.2}$$

with the overplus part of the positive energy defined as

$$\Delta\rho_0^S \psi^{S+} := \begin{cases} \rho_0^S \psi^{S+} - \Upsilon_t^S, & \text{for } \rho_0^S \psi^{S+} > \Upsilon_t^S \\ \\ 0, & \text{else.} \end{cases} \tag{5.3}$$

From (5.2), the evolution of the phase variable will not start until the strain energy reaches the triggering energy. This guarantees an elastic and non-dissipative material behaviour before a crack occurs. Moreover, only the overplus part of the positive energy, $\Delta\rho_0^S \psi^{S+}$, instead of the total positive energy, contributes to the phase-variable evolution. Thus, the crack growth owing to the micro-crack accumulation depends on the part of the positive strain energy which is greater than the triggering strain energy. The crack will propagate only if the strain energy is larger than the triggering energy.

5.1.2 Fracturing as an irreversible process

Fracture in a fracking process is usually considered to be irreversible since the solid skeleton, e. g. shale, cannot be self-healed or self-sealed. Therefore, the evolution of the phase variable, reflecting the accumulation of the micro-cracks, must be monotonic, viz.:

$$(\phi^S)'_S \geq 0. \tag{5.4}$$

If this condition is considered in (5.2), the evolution equation will be rewritten as

$$(\phi^S)'_S = \mathrm{Max} \left\{ \frac{1}{M} \left[2(1-\phi^S) \, \Delta\rho_0^S \psi^{S+} - G_c(\frac{\phi^S}{\epsilon} - \epsilon \, \mathrm{div} \, \mathrm{grad} \, \phi^S) \right], 0 \right\}. \tag{5.5}$$

However, the switch in this equation may lead to divergence in the numerical implementation. In order to address this problem equivalently without losing efficiency, a history variable defined as

$$\mathcal{H} = \mathrm{Max}_{t \geqq t_0} \, (\Delta\rho_0^S \psi^{S+}), \tag{5.6}$$

has been introduced in the work of Miehe et al. [155]. The evolution equation is thus reformulated as

$$(\phi^S)'_S = \frac{1}{M} \left[2(1-\phi^S) \, \mathcal{H} - G_c(\frac{\phi^S}{\epsilon} - \epsilon \, \mathrm{div} \, \mathrm{grad} \, \phi^S) \right]. \tag{5.7}$$

For a comprehensive explanation, one may compare, e. g. Miehe et al. [155] and Hofacker [115].

5.1.3 Implementation of initial cracks

In order to initialise a crack in an ideally homogeneous material, a straightforward way is to introduce a geometrical singularity as an imperfection. The realisation of such a geometrical imperfection may be obtained by two approaches. One is to introduce a notch when setting up the geometry of the model while the other requires an initial pseudo-energy in the target area such that the phase variable evolves until reaching the limiting value 1.0 and the resistance of the solid skeleton vanishes in the meantime. In

Table 5.1: *Parameters for the single-phasic solid material*

μ^S	$8.077 \times 10^{10}\,\mathrm{Pa}$	λ^S	$12.115 \times 10^{10}\,\mathrm{Pa}$	G_c	$2.7 \times 10^3\,\mathrm{N/m}$
ϵ	$0.01\,\mathrm{m}$	η_r	1×10^{-4}	M	$3 \times 10^{-6}\,\mathrm{N/(ms)}$

order to compare these two approaches, an example is given here where a standard tensile test on a pure solid is simulated. The geometry, material properties and loading settings are inspired by the work of Miehe et al. [155]. The material properties are listed in Table 5.1. The geometry, together with the boundary conditions, is demonstrated in Figure 5.1.
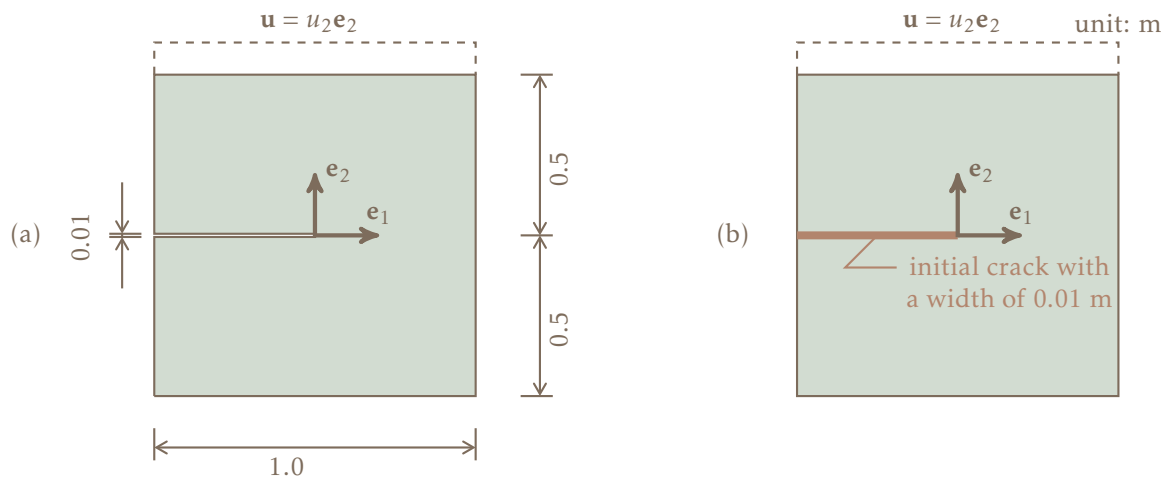
Figure 5.1: *Geometry and boundary conditions of a pure solid block.*

In case (a), a rectangular notch with an open crack of $0.01\,\mathrm{m}$ and a length of $0.5\,\mathrm{m}$ is located in the left middle of a square which has a length of 1m. In case (b), this notch is substituted by a rectangular area with a size of $0.5\,\mathrm{m} \times 0.01\,\mathrm{m}$. In order to obtain a phase variable with the value of one that denotes a fully cracked material therein, an initial pseudo energy $\mathcal{H}_0$ is introduced into the evolution equation such that a smeared crack is generated before the load $\mathbf{u}$ is applied. The value of this initial pseudo energy has been investigated in the work of Borden et al. [33] and reads,

$$\mathcal{H}_0 = \frac{G_c}{4\,\epsilon\,(1 - \phi^S)}. \tag{5.8}$$

By choosing $\phi^S = 0.999$ (when $\phi^S = 0.999$, the material is considered to be fully fractured), the initial pseudo energy is then computed to be $6.75 \times 10^7\,J/m^3$ for case (b). For the geometrical notch in the first case, this pseudo energy is not necessary and omitted. Furthermore, the displacement function $\mathbf{u}$ is given by

$$u_2 = \begin{cases} 0, & \text{for } t \leq 10\mathrm{s} \\ 1 \times 10^{-5}(t - 10)\,\mathrm{m}, & \text{for } t \in (10, 70)\mathrm{s} \end{cases} \tag{5.9}$$

Figure 5.2 shows the vertical reaction force with respect to the vertical displacement at the top. In comparison, no distinct difference is found except that in case (b), a higher reaction force is found after the crack has penetrated the whole cross-section. This is because the pre-defined diffusive crack provides the model with an extra residual stiffness. However, a diffusive crack has a unique advantage when treating the re-closing phenomena of pre-existing cracks. The continuous geometry of the diffusive crack prevents the adjacent crack surfaces from penetration. In opposite to that, in case (a), an extra description of the displacement in the notch has to be announced when the crack surfaces might contact each other. For example, a possible way is to compute the minimum distance between these two surfaces and prevent this value from being negative, which is feasible but becomes quite complex when a three-dimensional geometry comes into play. In this

regard, the diffusive crack model is a better solution and the small deviation of the force occurs when the generation of the crack is completed.
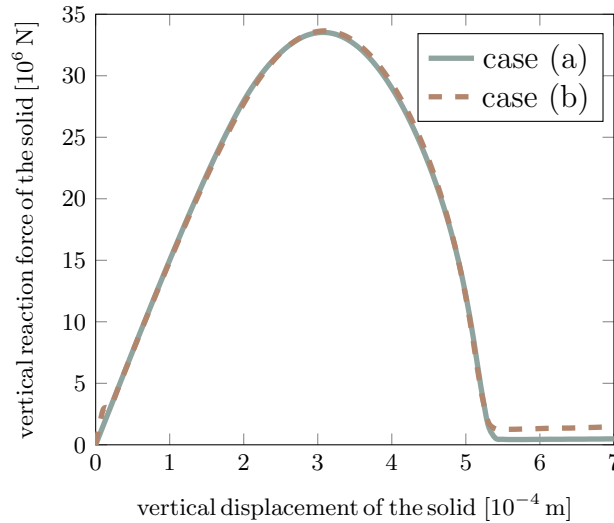

Figure 5.2: *Comparison of the displacement-force relations between a geometrical notch (case a) and a diffusive crack (case b).*

5.2   Finite-Element Method (FEM)

When tackling a set of Partial Differential Equations (PDEs) for an Initial-Boundary-Value problem (IBVP), analytical solutions can be obtained only for a very limited number of cases. As an auxiliary numerical approach, the FEM provides approximate solutions with satisfactory accuracy, if appropriately applied. Thus it has become the most commonly used numerical method in a variety of engineering fields. For an elaborate introduction into the theory and application, the reader may compare, e. g. the textbook of Bathe [15], Braess [45] and Hughs [117].

The Institute of Applied Mechanics (Chair of Continuum Mechanics) has dedicated thirty years in solving various coupled problems for multi-phasic materials and thus has accumulated enormous experience. The preparatory work in this field was accomplished by Ellsiepen [78], Eipper [77] and Ammann [8], who set up the fundamentals of the numerical software PANDAS, which specialises in the study of porous media. Moreover, Acartürk included real chemical mixtures in his work [1] while an advanced model concerning the viscoelasticity at large strains was considered by Markert [146] and his successor Karajan [129]. In addition, more specific characteristics of a solid skeleton were introduced by, e. g. Graf [94] and Avci [13] who discussed the elastoplastic behaviour, and Rempler [178] who described the fracture process in combination with the XFEM. Various applications, to name but a few, the drug-infusion processes in the brain tissue, the remodelling of the bone and the simulation of the human hip joint, have been investigated by Wagner [198], Krause [134] and Mabuma [143]. Furthermore, a tri-phasic material concerning a fluid-phase transition was proposed in the dissertation of Häberle [104], as well as Koch

[132] took the thermal effect into account. In order to discover the stability of the numerical methods applied to the coupled problem, Zinatbakhsh compared several typical numerical methods in his work [210].

5.2.1 Governing equations in strong and weak forms

Before solving the coupled problem, the set of primary variables needs to be determined. In order to avoid the second-order derivative terms, e. g. the acceleration of the solid, one may introduce the intermediate term, i. e. the solid velocity $\mathbf{v}_S$ as a primary variable such that the solid acceleration $\mathbf{a}_S$ is regarded as the first-order time derivative of $\mathbf{v}_S$. Furthermore, either the fluid velocity $\mathbf{v}_F$ or the seepage velocity $\mathbf{w}_F$ can be chosen as the primary variable for the kinematical description of the fluid phase. Herein, five primary variables are selected as

$$\mathcal{V} = \left\{ \mathbf{u}_S,\ \mathbf{v}_S,\ \mathbf{v}_F,\ p,\ \phi^S \right\}, \tag{5.10}$$

which corresponds to five partial differential equations. For $\mathbf{u}_S$, the equation corresponds to the solid displacement relation as

$$(\mathbf{u}_S)'_S = \mathbf{v}_S \tag{5.11}$$

Due to the absence of spatial-gradient terms in this relation, it is not necessary to approximate the nodal value by a discretisation in space within the numerical implementation. Therefore, in the next step, this equation will not be rewritten in a weak form nor be integrated over the whole domain. Instead, it is computed in the sense of a strong form in space.

Proceeding from the volume balance for one constituent, one derives the overall volume balance by summing up (4.9). Rewriting the sum by taking (4.12) into account yields

$$\sum (n^\alpha)'_\alpha + n^\alpha \operatorname{div} \overset{'}{\mathbf{x}}_\alpha = n^S \operatorname{div} \mathbf{v}_S + n^F \operatorname{div} \mathbf{v}_F + \operatorname{grad} n^F \cdot \mathbf{w}_F = \operatorname{div} \left(\mathbf{v}_S + n^F \mathbf{w}_F \right). \tag{5.12}$$

This equation will later correspond to the primary variable p.

By considering the momentum balance in Table 2.6, the overall momentum balance is a direct result of the sum of the momentum balance of both constituents. Thus, an arbitrary choice of two from these three momentum balance equations, namely the solid, the fluid and the overall aggregate, forms the set of momentum balances. As an example, the first set (Set I) selects the momentum balance of the overall aggregate and the fluid,

$$\begin{cases} \rho^S(\mathbf{v}_S)'_S + \rho^F(\mathbf{v}_F)'_S &= \operatorname{div}\left(\mathbf{T}_E^S + \mathbf{T}_E^F - p\,\mathbf{I}\right) + (\rho^S + \rho^F)\mathbf{g}, \\ \rho^F(\mathbf{v}_F)'_S &= \operatorname{div}\mathbf{T}_E^F - n^F \operatorname{grad} p + \rho^F\mathbf{g} + \hat{\mathbf{p}}_E^F, \end{cases} \tag{5.13}$$

while the second choice (Set II) is a combination of the momentum balances of the solid and the fluid,

$$\begin{cases} \rho^S(\mathbf{v}_S)'_S &= \operatorname{div}\boldsymbol{\sigma}_E^S - n^S \operatorname{grad} p + \rho^S\mathbf{g} - \hat{\mathbf{p}}_E^F, \\ \rho^F(\mathbf{v}_F)'_S &= \operatorname{div}\mathbf{T}_E^F - n^F \operatorname{grad} p + \rho^F\mathbf{g} + \hat{\mathbf{p}}_E^F. \end{cases} \tag{5.14}$$

Table 5.2: *Summary of governing PDE: Set I*

solid displacement-velocity relation:

$$(\mathbf{u}_S)'_S = \mathbf{v}_S$$

overall volume balance:

$$\mathrm{div}\left(\mathbf{v}_S + n^F \mathbf{w}_F\right) = 0$$
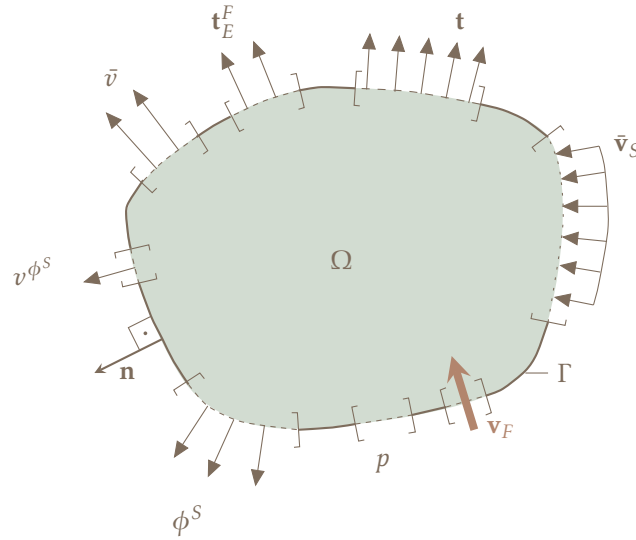
overall momentum balance:

$$\rho^S (\mathbf{v}_S)'_S + \rho^F (\mathbf{v}_F)'_S = \mathrm{div}\left(\mathbf{T}_E^S + \mathbf{T}_E^F - p\,\mathbf{I}\right) + (\rho^S + \rho^F)\mathbf{g}$$

fluid momentum balance:

$$\rho^F (\mathbf{v}_F)'_S = \mathrm{div}\,\mathbf{T}_E^F - n^F \mathrm{grad}\,p + \rho^F \mathbf{g} + \hat{\mathbf{p}}_E^F$$

phase-field evolution equation:

$$(\phi^S)'_S = \frac{1}{M}\left[2(1-\phi^S)\mathcal{H} - \frac{G_c}{\epsilon}(\phi^S - \epsilon^2\,\mathrm{div}\,\mathrm{grad}\,\phi^S)\right]$$

Figure 5.3: *Boundary conditions applied to the target domain* Ω

Both sets are physically feasible, and an appropriate combination depends on the specific initial-boundary conditions in the application. For Set I, the required governing equations are summarised in Table 5.2. In accordance with each equation, the boundary conditions

can be split into the *Dirichlet*[1] (essential) and the *Neumann*[2] (natural) boundary conditions over the whole surface $\partial\Omega$. In particular, either the *Dirichlet* or the *Neumann* boundary condition must be defined for any arbitrary boundary such that each equation has a unique solution. However, simultaneously defining both boundary conditions causes a contradiction since, logically, one should be the response to the other. Thus, the two boundary conditions at a certain time instance on the same surface are mutually exclusive, and only one is definable and must be defined. In this context, the *Dirichlet* boundary conditions include the value for the primary variables as given by (5.10) while the *Neumann* boundary conditions are the overall traction term $\mathbf{t}$, the extra fluid traction $\mathbf{t}_E^F$, the fluid volume efflux $\bar{v}$ and the phase-variable efflux v^{ϕ^S}. The aforementioned restrictions are given by

$$\Gamma^S = \Gamma_{\mathbf{v}_S} \cup \Gamma_{\mathbf{t}} \qquad \text{and} \qquad \Gamma_{\mathbf{v}_S} \cap \Gamma_{\mathbf{t}} = 0,$$

$$\Gamma^F = \Gamma_{\mathbf{v}_F} \cup \Gamma_{\mathbf{t}_F^E} \qquad \text{and} \qquad \Gamma_{\mathbf{v}_F} \cap \Gamma_{\mathbf{t}_F^E} = 0,$$

$$\Gamma^p = \Gamma_p \cup \Gamma_{\bar{v}} \qquad \text{and} \qquad \Gamma_p \cap \Gamma_{\bar{v}} = 0,$$

$$\Gamma^{\phi^S} = \Gamma_{\phi^S} \cup \Gamma_{v^{\phi^S}} \qquad \text{and} \qquad \Gamma_{\phi^S} \cap \Gamma_{v^{\phi^S}} = 0,$$

and the definition of the *Neumann* boundary conditions are given as

$$\mathbf{t} = (\boldsymbol{\sigma}_E^S + \mathbf{T}_F^S - p\,\mathbf{I})\mathbf{n}, \quad \mathbf{t}_E^F = \mathbf{T}_E^F\,\mathbf{n}, \quad \bar{v} = (n^F\mathbf{w}_F)\cdot\mathbf{n} \quad \text{and} \quad v^{\phi^S} = \operatorname{grad}\phi^S\cdot\mathbf{n}.$$

Analogously, the governing PDEs for Set II are summarised in Table 5.3. Comparing the equations in both sets, one recognises that the key difference lies in the *Neumann* boundary conditions for the momentum balance. As the solid momentum balance is considered in Set II instead of the overall momentum balance, its corresponding *Neumann* boundary condition is the extra solid traction and subjected to

$$\Gamma^S = \Gamma_{\mathbf{v}_S} \cup \Gamma_{\mathbf{t}_S^E} \qquad \text{and} \qquad \Gamma_{\mathbf{v}_S} \cap \Gamma_{\mathbf{t}_S^E} = 0,$$

where the extra solid traction is defined via

$$\mathbf{t}_E^S = \boldsymbol{\sigma}_E^S\mathbf{n}. \tag{5.15}$$

For a typical consolidation process of soil, the soil block takes over the compressive load, usually coming from the top. This downward force is applied to the whole surface, consisting of the solid and the fluid. However, the ratio of the load, which each constituent undertakes, depends on the real-time deformation and hence cannot be defined as a boundary condition. Therefore, Set I is more appropriate in this scenario as the overall traction, instead of the extra solid traction is prescribed as the *Neumann* boundary condition. To give a contrast illustration, one may regard the process of squeezing a foam full of water with a net full of holes. The water will flow out of the foam freely, and for this reason, no constraint force from the net is carried by it. Therefore, the force is completely applied to the solid skeleton and thus Set II makes the boundary conditions easier to be included in the numerical implementation.

---

[1] *Peter Gustav Lejeune Dirichlet* (18051859): German mathematician.
[2] *Carl Gottfried Neumann* (1832-1925): German mathematician.

Table 5.3: *Summary of governing PDE: Set II*

solid displacement-velocity relation:

$$(\mathbf{u}_S)'_S = \mathbf{v}_S$$

overall volume balance:

$$\mathrm{div}\left(\mathbf{v}_S + n^F \mathbf{w}_F\right) = 0$$

solid momentum balance:

$$\rho^S (\mathbf{v}_S)'_S = \mathrm{div}\,\boldsymbol{\sigma}_E^S - n^S \mathrm{grad}\, p + \rho^S \mathbf{g} - \hat{\mathbf{p}}_E^F$$

fluid momentum balance:

$$\rho^F (\mathbf{v}_F)'_S = \mathrm{div}\,\mathbf{T}_E^F - n^F \mathrm{grad}\, p + \rho^F \mathbf{g} + \hat{\mathbf{p}}_E^F$$

phase-field evolution equation:

$$(\phi^S)'_S = \frac{1}{M}\left[2(1-\phi^S)\mathcal{H} - \frac{G_c}{\epsilon}(\phi^S - \epsilon^2\,\mathrm{div}\,\mathrm{grad}\,\phi^S)\right]$$

5.2.2 Discretisation in space and time

For an IBVP, if one can find a set of solutions satisfying the PDEs in Table 5.2 or Table 5.3, then this solution is exact at each material point $\mathcal{P}$, and these PDEs are the balance/evolution equations in the so-called strong form. However, in order to compute the approximate solution instead of the exact one, the PDEs need to be transformed into the "weak" form at first. This is realised by multiplying each PDE with its corresponding test function and then by integrating the product over the whole domain. These equations hold in a "weak" sense because the equilibrium stays for the whole body $\mathcal{B}$ in an integral (distributed) manner instead of being satisfied for every material point $\mathcal{P}$. In addition, the original PDEs are also weighted by the test functions. Based on the given two sets of governing equations, the weak forms are listed in Table 5.4 and Table 5.5, respectively. Note that the solid displacement-velocity relation is not considered here. Hence, only the remainder of the primary variables $\mathcal{V}_S$ require the so-called ansatz functions, which,

Table 5.4: *Weak form of the governing partial differential equations: Set I*

---

overall volume balance:

$$\mathcal{G}_p = \int_{\mathcal{B}} \left(\operatorname{div} \mathbf{v}_S \, \delta p - n^F \mathbf{w}_F \cdot \operatorname{grad} \delta p \right) \mathrm{d}v + \int_{\mathcal{S}} \bar{v} \, \delta p \, \mathrm{d}a = 0$$

overall momentum balance:

$$\boldsymbol{\mathcal{G}}_{\mathbf{v}_S} = \int_{\mathcal{B}} \Big\{ \, [\rho^S (\mathbf{v}_S)'_S + \rho^F (\mathbf{v}_F)'_S] \cdot \delta \mathbf{v}_S + (\boldsymbol{\sigma}_E^S + \mathbf{T}_E^F - p\,\mathbf{I}) \cdot \operatorname{grad} \delta \mathbf{v}_S -$$

$$- (\rho^S + \rho^F)\, \mathbf{g} \cdot \delta \mathbf{v}_S \Big\} \, \mathrm{d}v - \int_{\mathcal{S}} \bar{\mathbf{t}} \cdot \delta \mathbf{v}_S \, \mathrm{d}a = 0$$

fluid momentum balance:

$$\boldsymbol{\mathcal{G}}_{\mathbf{v}_F} = \int_{\mathcal{B}} [\rho^{FR} (\mathbf{v}_F)'_S \cdot \delta \mathbf{v}_F + \mathbf{T}_E^F \cdot \operatorname{grad} \delta \mathbf{v}_F + n^F \operatorname{grad} p \cdot \delta \mathbf{v}_F - \rho^F \mathbf{g} \cdot \delta \mathbf{v}_F -$$

$$- \hat{\mathbf{p}}_E^F \cdot \delta \mathbf{v}_F] \, \mathrm{d}v - \int_{\mathcal{S}} \bar{\mathbf{t}}_E^F \cdot \delta \mathbf{v}_F \, \mathrm{d}a = 0$$

phase-field evolution equation:

$$\mathcal{G}_{\phi^S} = \int_{\mathcal{B}_S} \left([M(\phi^S)'_S - 2(1 - \phi^S)\mathcal{H} + \frac{G_c}{\epsilon}\phi^S] \delta \phi^S + G_c \epsilon \operatorname{grad} \phi^S \cdot \operatorname{grad} \delta \phi^S \right) \mathrm{d}v -$$

$$- \int_{\mathcal{S}} G_c \epsilon \operatorname{grad} \phi^S \cdot \mathbf{n} \, \delta \phi^S \, \mathrm{d}a = 0$$

---

together with their *Sobolev*[3] spaces $\mathcal{H}^1(\Omega)^4$, are defined as

$$\mathcal{A}^{\mathbf{v}_S}(t) := \{\mathbf{v}_S \in \mathcal{H}^1(\Omega)^d : \mathbf{v}_S(\mathbf{x}) = \bar{\mathbf{v}}_S(\mathbf{x}, t) \text{on } \Gamma_D^{\mathbf{v}_S}\},$$

$$\mathcal{A}^{\mathbf{v}_F}(t) := \{\mathbf{v}_F \in \mathcal{H}^1(\Omega)^d : \mathbf{v}_F(\mathbf{x}) = \bar{\mathbf{v}}_F(\mathbf{x}, t) \text{on } \Gamma_D^{\mathbf{v}_F}\},$$

$$\mathcal{A}^p(t) := \{p \in \mathcal{H}^1(\Omega)^d : p(\mathbf{x}) = \bar{p}(\mathbf{x}, t) \text{on } \Gamma_D^p\},$$

$$\mathcal{A}^{\phi^S}(t) := \{\phi^S \in \mathcal{H}^1(\Omega)^d : \phi^S(\mathbf{x}) = \bar{\phi}^S(\mathbf{x}, t) \text{on } \Gamma_D^{\phi^S}\},$$

$$(5.16)$$

with

$$\mathcal{V}_S = \{\mathbf{v}_S, \mathbf{v}_F, p, \phi^S\} . \tag{5.17}$$

---
[3] *Sergei Lvovich Sobolev* (1908-1989): Soviet mathematician.
[4] The Sobolev space $\mathcal{H}^1(\Omega)$ is a vector space, where the first-order derivatives of the functions are square integrable, cf. e. g. Bathe [15].

Theoretically, the test functions can be any arbitrary functions, since the equations hold for any material points at an arbitrary time instance in the strong forms. However, in practice, the test functions are usually considered to be identical to the ansatz functions, which is also known as the *Galerkin*[5] method. If the test functions are not identical to the ansatz functions, then the method is referred to *Petrov*[6]-*Galerkin* Method. In this context, the *Galerkin* method is applied, namely,

$$
\begin{aligned}
\mathcal{T}^{\mathbf{v}_S}(t) &:= \{\delta\mathbf{v}_S \in \mathcal{H}^1(\Omega)^d : \delta\mathbf{v}_S(\mathbf{x}) = \bar{\mathbf{v}}_S(\mathbf{x},\,t)\,\text{on}\,\Gamma_D^{\mathbf{v}_S}\}, \\[6pt]
\mathcal{T}^{\mathbf{v}_F}(t) &:= \{\delta\mathbf{v}_F \in \mathcal{H}^1(\Omega)^d : \delta\mathbf{v}_F(\mathbf{x}) = \bar{\mathbf{v}}_F(\mathbf{x},\,t)\,\text{on}\,\Gamma_D^{\mathbf{v}_F}\}, \\[6pt]
\mathcal{T}^{p}(t) &:= \{\delta p \in \mathcal{H}^1(\Omega)^d : \delta p(\mathbf{x}) = \bar{p}(\mathbf{x},\,t)\,\text{on}\,\Gamma_D^{p}\}, \\[6pt]
\mathcal{T}^{\phi^S}(t) &:= \{\delta\phi^S \in \mathcal{H}^1(\Omega)^d : \delta\phi^S(\mathbf{x}) = \bar{\phi}^S(\mathbf{x},\,t)\,\text{on}\,\Gamma_D^{\phi^S}\}.
\end{aligned}
\tag{5.18}
$$

During integration the multiplication products, the *Gauss*ian integral theorem is used such that certain terms in the volume domain, e. g. the total stress, are equivalently substituted by other terms over the surface, e. g. the overall traction force. Note that the application of the *Gauss*ian integral theorem not only helps to reduce the derivative order of the integrants but also allows the *Neumann* boundary condition to be explicitly assigned to the PDEs.
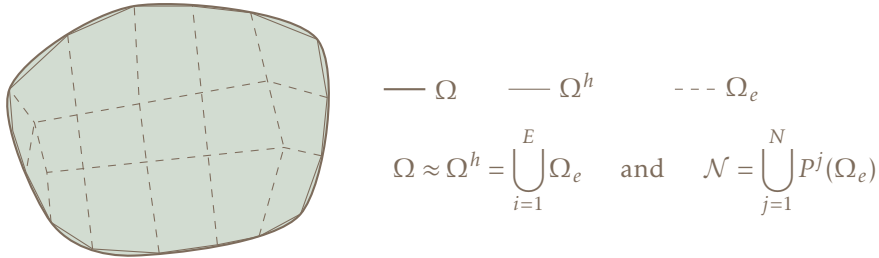

$$
\text{---}\ \Omega \qquad \text{---}\ \Omega^h \qquad \text{-- --}\ \Omega_e
$$

$$
\Omega \approx \Omega^h = \bigcup_{i=1}^{E}\Omega_e \quad \text{and} \quad \mathcal{N} = \bigcup_{j=1}^{N}P^j(\Omega_e)
$$

Figure 5.4: *Exemplary spatial discretisation of a certain domain.*

With the weak forms at hand, a standard FEM procedure then discretises the whole continuous domain Ω into a number E of non-overlapping finite subdomains Ω_e, which are also known as the finite elements. For an infinitely great number E, the discretised domain Ω is equivalent to the original domain Ω. In addition, nodal points with a number of N_e in each finite element are introduced, which are mutually interconnected with the common nodes of the adjacent element. In this context, the sum of all nodes is expressed by $\mathcal{N}$.

After approximating the domain Ω by its discretised one Ω^h, the continuous ansatz func-

---

[5] *Boris Grigoryevich Galerkin* (1871-1945): Soviet mathematician and engineer.
[6] *Georgy Petrov* (1912-1987): Soviet engineer.

Table 5.5: *Weak form of the governing partial differential equations: Set II*

overall volume balance:

$$\mathcal{G}_p = \int_{\mathcal{B}} \left(\operatorname{div} \mathbf{v}_S \, \delta p - n^F \mathbf{w}_F \cdot \operatorname{grad} \delta p \right) \mathrm{d}v + \int_{\mathcal{S}} \bar{v} \, \delta p \, \mathrm{d}a = 0$$

solid momentum balance:

$$\boldsymbol{\mathcal{G}}_{\mathbf{v}_S} = \int_{\mathcal{B}} [\, \rho^S (\mathbf{v}_S)'_S \cdot \delta \mathbf{v}_S + \boldsymbol{\sigma}_E^S \cdot \operatorname{grad} \delta \mathbf{v}_S + n^S \operatorname{grad} p \cdot \delta \mathbf{v}_S - \rho^S \mathbf{g} \cdot \delta \mathbf{v}_S +$$

$$\hat{\mathbf{p}}_E^F \cdot \delta \mathbf{v}_S \mathrm{d}v - \int_{\mathcal{S}} \bar{\mathbf{t}}_E^S \cdot \delta \mathbf{v}_S \, \mathrm{d}a = 0$$

fluid momentum balance:

$$\boldsymbol{\mathcal{G}}_{\mathbf{v}_F} = \int_{\mathcal{B}} [\, \rho^{FR} (\mathbf{v}_F)'_S \cdot \delta \mathbf{v}_F + \mathbf{T}_E^F \cdot \operatorname{grad} \delta \mathbf{v}_F + n^F \operatorname{grad} p \cdot \delta \mathbf{v}_F - \rho^F \mathbf{g} \cdot \delta \mathbf{v}_F -$$

$$- \hat{\mathbf{p}}_E^F \cdot \delta \mathbf{v}_F] \mathrm{d}v - \int_{\mathcal{S}} \bar{\mathbf{t}}_E^F \cdot \delta \mathbf{v}_F \, \mathrm{d}a = 0$$

phase-field evolution equation:

$$\mathcal{G}_{\phi^S} = \int_{\mathcal{B}_S} \left([M(\phi^S)'_S - 2(1 - \phi^S)\mathcal{H} + \frac{G_c}{\epsilon} \phi^S] \delta \phi^S + G_c \epsilon \operatorname{grad} \phi^S \cdot \operatorname{grad} \delta \phi^S \right) \mathrm{d}v -$$

$$- \int_{\mathcal{S}} G_c \epsilon \operatorname{grad} \phi^S \cdot \mathbf{n} \, \delta \phi^S \, \mathrm{d}a = 0$$

tions are approximated according to the nodal values and the basis functions,

$$
\begin{aligned}
\mathbf{v}_S(\mathbf{x}, t) &\approx \mathbf{v}_S^h(\mathbf{x}, t) &= \bar{\mathbf{v}}_S^h(\mathbf{x}, t) &+ \sum_{j=1}^{N} Q_{\mathbf{v}_S}^j(\mathbf{x}) \, \mathbf{v}_S^j(t) \in \mathcal{A}_{\mathbf{v}_S}^h, \\
\mathbf{v}_F(\mathbf{x}, t) &\approx \mathbf{v}_F^h(\mathbf{x}, t) &= \bar{\mathbf{v}}_F^h(\mathbf{x}, t) &+ \sum_{j=1}^{N} Q_{\mathbf{v}_F}^j(\mathbf{x}) \, \mathbf{v}_F^j(t) \in \mathcal{A}_{\mathbf{v}_F}^h, \\
p(\mathbf{x}, t) &\approx p^h(\mathbf{x}, t) &= \bar{p}^h(\mathbf{x}, t) &+ \sum_{j=1}^{N} Q_p^j(\mathbf{x}) \, p(t) \in \mathcal{A}_p^h, \\
\phi^S(\mathbf{x}, t) &\approx (\phi^S)^h(\mathbf{x}, t) &= (\bar{\phi}^S)^h(\mathbf{x}, t) &+ \sum_{j=1}^{N} Q_{\phi^S}^j(\mathbf{x}) \, \phi^S(t) \in c.
\end{aligned}
\tag{5.19}
$$

Analogously, the test functions are also meshed into the finite elements as,

$$
\begin{aligned}
\delta\mathbf{v}_S(\mathbf{x}, t) &\approx \delta\mathbf{v}_S^h(\mathbf{x}, t) & &= \delta\bar{\mathbf{v}}_S^h(\mathbf{x}, t) & &+ \sum_{j=1}^{N} Q_{\mathbf{v}_S}^j(\mathbf{x})\,\delta\mathbf{v}_S^j(t) \in \mathcal{T}_{\mathbf{v}_S}^h, \\
\delta\mathbf{v}_F(\mathbf{x}, t) &\approx \delta\mathbf{v}_F^h(\mathbf{x}, t) & &= \delta\bar{\mathbf{v}}_F^h(\mathbf{x}, t) & &+ \sum_{j=1}^{N} Q_{\mathbf{v}_F}^j(\mathbf{x})\,\delta\mathbf{v}_F^j(t) \in \mathcal{T}_{\mathbf{v}_F}^h, \\
\delta p(\mathbf{x}, t) &\approx \delta p^h(\mathbf{x}, t) & &= \delta\bar{p}^h(\mathbf{x}, t) & &+ \sum_{j=1}^{N} Q_p^j(\mathbf{x})\,\delta p(t) \in \mathcal{T}_p^h, \\
\delta\phi^S(\mathbf{x}, t) &\approx \delta(\phi^S)^h(\mathbf{x}, t) & &= \delta(\bar{\phi}^S)^h(\mathbf{x}, t) & &+ \sum_{j=1}^{N} Q_{\phi^S}^j(\mathbf{x})\,\delta\phi^S(t) \in \mathcal{T}_{(\phi^S)^h}.
\end{aligned}
\tag{5.20}
$$

The values of the primary variables set $\mathcal{V}_S$ at every node are the so-called degrees of freedom (DOF) of the system. In order to guarantee exact values at these nodes, the easiest way is to assume that the basis function $Q_{\mathcal{V}_S}^j$ holds for

$$
\begin{cases}
Q_{\mathcal{V}_S}^j(\mathbf{x}) = 0, & \text{for } \mathbf{x} \notin \bigcup_{e \in E^*} \Omega_e \\[2mm]
Q_{\mathcal{V}_S}^j(\mathbf{x}^{P^i}) = \delta_{ij}, & \text{for } \mathbf{x} \in \bigcup_{e \in E^*} \Omega_e.
\end{cases}
\tag{5.21}
$$

After the spatial discretisation, the present target is to find

$$
\begin{cases}
\mathbf{v}_S^h & \in \mathcal{A}_{\mathbf{v}_S}^h \quad \forall\delta\mathbf{v}_S^h & \in \mathcal{T}_{\mathbf{v}_S}^h \\[2mm]
\mathbf{v}_F^h & \in \mathcal{A}_{\mathbf{v}_F}^h \quad \forall\delta\mathbf{v}_F^h & \in \mathcal{T}_{\mathbf{v}_F}^h \\[2mm]
p^h & \in \mathcal{A}_p^h \quad \forall\delta p^h & \in \mathcal{T}_p^h \\[2mm]
(\phi^S)^h & \in \mathcal{T}_p^h \quad \forall\delta(\phi^S)^h & \in \mathcal{T}_{(\phi^S)^h}
\end{cases}
\quad \text{such that} \quad
\begin{cases}
\mathcal{G}_{\mathbf{v}_S}^h & = \mathbf{0} \\[2mm]
\mathcal{G}_{\mathbf{v}_F}^h & = \mathbf{0} \\[2mm]
\mathcal{G}_p^h & = 0 \\[2mm]
\mathcal{G}_{\phi^S}^h & = 0
\end{cases}
\tag{5.22}
$$

for a given set of initial and boundary conditions. In this regard, the test functions are limited by the so-called Partition-to-Unity principle, which states that the sum of the basis functions at each node must be equal to one. Basically, different or identical ansatz functions for each primary variable are both feasible to solve the problem. Nevertheless, a poor choice may cause computational instability and results in an oscillation of the solution, cf. Acartürk [1] and Graf [94]. Concerning the fracking problem, the unknown quantities, e. g. the solid displacement $\mathbf{u}_S$ and the pore pressure p, are present in both governing equations. This feature leads to a strong coupling when solving the problem simultaneously by a numerical method. Hence, a so-called mixed finite-element formulation of the basis functions is suggested by Acartürk [1]. Following his consideration, quadratic shape functions are used for the solid displacement $\mathbf{v}_S$ and the fluid velocity $\mathbf{v}_F$, while the pore pressure p and the phase variable ϕ^S are approximated by linear shape functions. To be consistent, the solid displacement $\mathbf{u}_S$ has the same order as the basis function of $\mathbf{v}_S$. This choice yields an equal-order approximation between the extra solid/fluid stress and the pore pressure if one notices that the stress, together with the strain, is a function

containing the gradient term of the displacement. This element type is usually known as the extended Taylor-Hood type, cf. Taylor & Hood [193], and is exemplarily illustrated in Figure 5.5 for a 10-noded tetrahedron and a 20-noded hexahedron in a three-dimensional case. In this example, the blue circles (only at the corners) denote nodal values for p and ϕ^S while the solid coral dots (both at the corners and in the middle of the edges) represent nodal values for $\mathbf{v}_S$ and $\mathbf{v}_F$. For any arbitrary element in the numerical model, one can
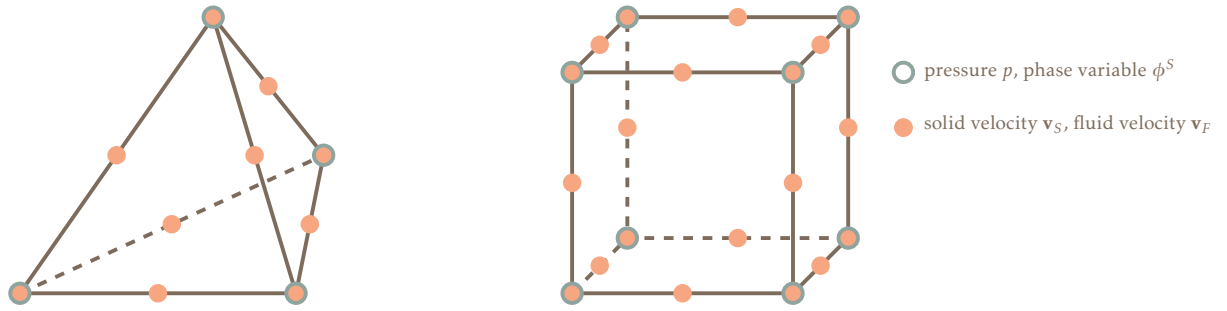

Figure 5.5: *Extended tetrahedral and hexahedral Taylor-Hood elements in three dimensions.*

transform its geometry to a standard reference element, where the local coordinates are denoted by, for example, $\boldsymbol{\xi}$. The location position $\mathbf{x}(\boldsymbol{\xi})$ reads
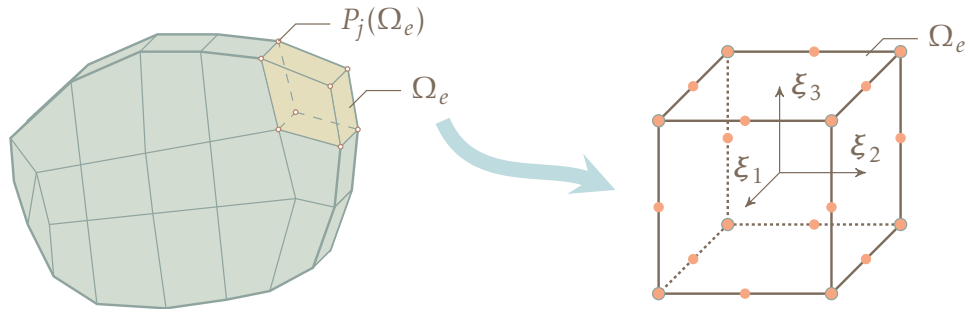

Figure 5.6: *Example of the geometry transformation for a hexahedral element with the local coordinates $\boldsymbol{\xi}_i \, (i = 1, 2, 3)$.*

$$\mathbf{x}(\boldsymbol{\xi}) = \sum_{j=1}^{N^e} \phi_{geo}^j(\boldsymbol{\xi})\mathbf{x}_j = \sum_{j=1}^{N^e} \phi^j(\boldsymbol{\xi})\mathbf{x}_j. \tag{5.23}$$

Herein, $\mathbf{x}(\boldsymbol{\xi})$ is an arbitrary position depending on the local coordinates $\boldsymbol{\xi}$, and $\phi_{geo}^j(\boldsymbol{\xi})$ is the basis function of the geometry transformation. If applying an isoparametric mapping, one can conclude $\phi_{geo}^j = \phi^j$. Such a transformation saves computational effort by unifying the basis/test functions and establishing a local but invariant coordinate system, where the weak formulations, given in Table 5.4 and 5.5, within one element can be reformulated with respect to the local coordinates. For an arbitrary vectorial function $\mathbf{f}(\mathbf{x})$, this yields

$$\int_{\Omega_e} \mathbf{f}(\mathbf{x})\mathrm{d}v = \int_{\Omega_e^\xi} \mathbf{f}(\mathbf{x}(\boldsymbol{\xi}))J_e(\boldsymbol{\xi})\mathrm{d}\,v_{\boldsymbol{\xi}} \quad \text{with} \quad J_e(\boldsymbol{\xi}) = \det\left(\frac{\mathrm{d}\,\mathbf{x}(\boldsymbol{\xi})}{\mathrm{d}\,\boldsymbol{\xi}}\right), \tag{5.24}$$

where $\mathrm{d}\,v_{\boldsymbol{\xi}}$ denotes the incremental volume element of the standard reference element whose *Jacobi*an determinant is known as J_e. Regarding the chosen basis/test functions (polynomial), one benefits further from a reduction of computational effort by exploiting certain integral schemes. The n-point *Gauss-Legendre* quadrature for a line element, for instance, can produce an accurate result up to an order of 2n-1 for polynomial functions within the range of [-1, 1], cf. Stoer & Bulirsch [191]. Thus, for a standard reference element, the limits of the coordinates can be chosen as [-1, 1] and the integral of each element is approximated by a summation of the product between the values at the integration points K_G at fixed local positions $\boldsymbol{\xi}_k$ and its corresponding quadrature weights w_k, viz.:

$$\int_{\Omega_e^{\xi}} \mathbf{f}(\mathbf{x}(\boldsymbol{\xi})) J_e(\boldsymbol{\xi}) \mathrm{d}\,v_{\boldsymbol{\xi}} = \sum_{k=1}^{K_G} \mathbf{f}(\mathbf{x}(\boldsymbol{\xi})) J_e(\boldsymbol{\xi}) w_k. \tag{5.25}$$

To summarise, the integral over the whole domain results in

$$\int_{\Omega} \mathbf{f}(\mathbf{x}) \mathrm{d}\,\mathbf{x} = \int_{\Omega^h} \mathbf{f}(\mathbf{x}) \mathrm{d}\,\mathbf{x} = \sum_{e=1}^{N_e} \int_{\Omega_e^h} \mathbf{f}(\mathbf{x}) \mathrm{d}\,\mathbf{x} \approx \sum_{e=1}^{N_e} \sum_{k=1}^{K_G} \mathbf{f}(\boldsymbol{\xi}_k) J_e(\boldsymbol{\xi}_k) w_k. \tag{5.26}$$

After the spatial discretisation, the time-derivative term in the governing equation also needs to be approximated. For this purpose, a finite difference scheme is applied here, where the numerical solution only depends on the previous time-step. Note that the current differential-algebraic equations (DAE) are of a first-order system, the implicit *Euler* time-integration method is chosen from the available *Runge*[7]-*Kutta*[8] class in the PANDAS solver. Proceeding from *Taylor*'s expansion, this method computes the time derivative at time t_n based on its value $\boldsymbol{y}_{t_n}$ at the current time t_n and that $\boldsymbol{y}_{t_{n-1}}$ at the time instance t_{n-1},

$$[(\boldsymbol{y})'_S]_{t_n} = \frac{1}{t_n - t_{n-1}}(\boldsymbol{y}_{t_n} - \boldsymbol{y}_{t_{n-1}}) = \frac{1}{\Delta t_n}(\boldsymbol{y}_{t_n} - \boldsymbol{y}_{t_{n-1}}), \tag{5.27}$$

where $\boldsymbol{y}$ includes the complete set of primary variables. Besides, an adaptive time stepping is applied such that the time-step size is adaptively controlled by the truncation error within one time step. The algorithm for this adaptive time stepping is also included in the FEM-solver PANDAS. Thanks to the introduction of the solid displacement-velocity relation, the governing functions can be simply expressed as a set of functions depending on the primary variables $\boldsymbol{y}$, their first-order time derivatives with respect to the solid

---

[7]*Carl David Tolmé Runge* (1856-1927): German mathematician, physicist and spectroscopist.
[8]*Martin Wilhelm Kutta* (1867-1944): German mathematician.

deformation $(\boldsymbol{y})'_S$, and the time t, viz.:

$$
\boldsymbol{\mathcal{F}}(\boldsymbol{y}, (\boldsymbol{y})'_S, t) =
\left\{
\begin{array}{c}
(\mathbf{u}_S)'_S - \mathbf{v}_S \\[2ex]
\dfrac{\partial}{\partial \delta \mathbf{v}_S} \boldsymbol{\mathcal{G}}_{\mathbf{v}_S} \\[2ex]
\dfrac{\partial}{\partial \delta \mathbf{v}_F} \boldsymbol{\mathcal{G}}_{\mathbf{v}_F} \\[2ex]
\dfrac{\partial}{\partial \delta p} \mathcal{G}_p \\[2ex]
\dfrac{\partial}{\partial \delta \phi^S} \mathcal{G}_{\phi^S}
\end{array}
\right\}
\stackrel{!}{=} \mathbf{0}
\quad \text{with} \quad
\boldsymbol{y} :=
\left\{
\begin{array}{c}
\mathbf{u}_S \\[2ex]
\mathbf{v}_S \\[2ex]
\mathbf{v}_F \\[2ex]
p \\[2ex]
\phi^S
\end{array}
\right\}
\quad \text{and} \quad
(\boldsymbol{y})'_S =
\left\{
\begin{array}{c}
\mathbf{v}_S \\[2ex]
\mathbf{a}_S \\[2ex]
(\mathbf{v}_F)'_S \\[2ex]
(p)'_S \\[2ex]
(\phi^S)'_S
\end{array}
\right\}
$$

Up to now, a group of nonlinear algebraic equations with $\mathcal{N}$ DOF is derived. In the next step, the values satisfying these equilibriums need to be determined. A proper computation method needs to be chosen carefully as it highly influences the results and computational efficiency. Herein, a monolithic scheme that derives all solutions simultaneously is applied. In general, it is also possible to solve the equations by a staggered scheme, which, in certain circumstance, offers a robust algorithm, cf. Miehe et al. [155] and Markert et al. [147]. Nevertheless, regarding the numerical consistency and stability, a monolithic method, together with the aforementioned Taylor-Hood elements and a backward *Euler* time integration method, provides an unconditionally stable solution, cf. Ehlers et al. [71]. This conclusion is guaranteed by fulfilling the *Layzhenskaya*[9]-*Babuška*[10]-*Brezzi*[11] condition (LBB condition), often known as the inf-sup condition, cf. Markert et al. [147]. In addition, compared to the monolithic scheme, the computational efficiency gained by the partitioned strategy is not guaranteed for the case that the differential equations are coupled through production terms throughout the whole domain, compare, e. g. , Felippa & Park [86].

5.3   Computation of the Consistent Tangent

When solving the non-linear system, an iteration scheme, for example, the *Newton-Raphson*[12] scheme is usually applied. This scheme is inspired by the *Taylor*-series expansion with respect to the variables $\boldsymbol{y}$ and $(\boldsymbol{y})'_S$, which is expressed, e. g. based on (5.2.2),

$$
\underbrace{\boldsymbol{\mathcal{F}}^{i_{m+1}}_{t_n}}_{\boldsymbol{\mathcal{R}}^{i_{m+1}}} = \underbrace{\boldsymbol{\mathcal{F}}^{i_m}_{t_n}}_{\boldsymbol{\mathcal{R}}^{i_m}} + \underbrace{\left.\frac{\partial \boldsymbol{\mathcal{F}}}{\partial \boldsymbol{y}}\right|^{i_m}_{t_n}}_{\boldsymbol{\mathcal{K}}^{i_m}} \underbrace{(\boldsymbol{y}^{i_{m+1}}_{t_n} - \boldsymbol{y}^{i_m}_{t_n})}_{\Delta \boldsymbol{y}^{i_m}} + \underbrace{\left.\frac{\partial \boldsymbol{\mathcal{F}}}{\partial (\boldsymbol{y})'_S}\right|^{i_m}_{t_n}}_{\boldsymbol{\mathcal{M}}^{i_m}} \underbrace{([(\boldsymbol{y})'_S]^{i_{m+1}}_{t_n} - [(\boldsymbol{y})'_S]^{i_m}_{t_n})}_{[\Delta (\boldsymbol{y})']^{i_m}}, \qquad (5.28)
$$

---

[9] *Olga Aleksandrovna Ldayzhenskaya* (1922-2004): Russian mathematician.
[10] *Ivo M. Babuška* (1926-): Czech American mathematician.
[11] *Franco Brezzi* (1945-): Italian mathematician.
[12] *Joseph Raphson* (1648-1715): English mathematician.

where the subscript t_n denotes the time instance, while the superscript i_m is the iteration index in two consecutive time instances, progressing from m to $m+1$. Assuming that the differences between the solutions are very small, the higher-order terms are negligible. As the residual terms $\boldsymbol{\mathcal{R}}$ should approach zero, the following equation holds,

$$\boldsymbol{\mathcal{R}}^{i_{m+1}} = \boldsymbol{\mathcal{R}}^{i_m} + \boldsymbol{\mathcal{K}}^{i_m}\Delta\boldsymbol{y}^{i_m} + \boldsymbol{\mathcal{M}}^{i_m}[\Delta(\boldsymbol{y})'_S]^{i_m} = 0, \tag{5.29}$$

where the stiffness matrix $\boldsymbol{\mathcal{K}}$ and the mass matrix $\boldsymbol{\mathcal{M}}$ are both denoted as consistent tangents. For the interpretation of the material time derivatives $(\boldsymbol{y})'_S$, the backward *Euler* difference scheme is applied. Taking notice of (5.27), one obtains the increment by solving the equation

$$\underbrace{(\boldsymbol{\mathcal{K}}^{i_m} + \frac{1}{\Delta t_{n+1}}\boldsymbol{\mathcal{M}}^{i_m})}_{D\boldsymbol{\mathcal{F}}_{t_n}^{i_m}}\Delta\boldsymbol{y}^{i_m} = -\boldsymbol{\mathcal{R}}^{i_m} + \frac{1}{\Delta t_{n+1}}\boldsymbol{\mathcal{M}}^{i_m}\Delta\boldsymbol{y}^{i_{m-1}}. \tag{5.30}$$

Then the solution is updated via

$$\boldsymbol{y}^{i_{m+1}} = \boldsymbol{y}^{i_m} + \Delta\boldsymbol{y}^{i_m} \tag{5.31}$$

Insertion of these values into the governing equations yields the new residual vector $\boldsymbol{\mathcal{R}}_{t_n}^{i_{m+1}}$. In order to evaluate the convergence of the solution, the norm of the residual vector is computed as the error and compared to a predefined tolerance ϵ_{tol} until the criterion,

$$||\boldsymbol{\mathcal{R}}_{t_n}^{i_{m+1}}|| \leq \epsilon_{\text{tol}}, \tag{5.32}$$

is fulfilled. Considering the decomposition the solid strain tensor, (4.51), two mapping tensors are defined as the partial derivatives of the solid positive/negative strain tensors with respect to the solid strain,

$$\overset{4}{\mathbf{G}}{}^+ := \frac{\boldsymbol{\varepsilon}_S^+}{\boldsymbol{\varepsilon}_S} \quad \text{and} \quad \overset{4}{\mathbf{G}}{}^- := \frac{\boldsymbol{\varepsilon}_S^-}{\boldsymbol{\varepsilon}_S}. \tag{5.33}$$

The summation of these two mapping tensors yields the fourth-order eigentensor,

$$\overset{4}{\mathbf{G}}{}^+ + \overset{4}{\mathbf{G}}{}^- = (\mathbf{I} \otimes \mathbf{I}) =: \overset{4}{\mathbf{I}}, \tag{5.34}$$

where $\overset{4}{\mathbf{I}}$ is the fourth-order identity tensor. With the aforementioned equations at hand, the consistent tangent $\overset{4}{\mathbf{B}}_S$ takes the form of

$$\overset{4}{\mathbf{B}}_S := \frac{\partial\boldsymbol{\sigma}_E^S}{\partial\boldsymbol{\varepsilon}_S} = \rho_0^S\frac{\partial^2\psi^S}{\partial\boldsymbol{\varepsilon}_S \otimes \partial\boldsymbol{\varepsilon}_S} = \left[(1-\phi^S)^2 + \eta_r^S\right]\left\{2\,\mu^S\,\overset{4}{\mathbf{G}}{}^+ + \lambda^S\,\text{sgn}[(\text{tr}\,\boldsymbol{\varepsilon}_S)^+]\,\mathbf{I}\otimes\mathbf{I}\right\} +$$

$$+ 2\,\mu^S\,\overset{4}{\mathbf{G}}{}^- - \lambda^S\,\text{sgn}[(\text{tr}\,\boldsymbol{\varepsilon}_S)^-]\,\mathbf{I}\otimes\mathbf{I}, \tag{5.35}$$

where the sign function $\text{sgn}(x)$ is defined as

$$\text{sgn}(x) := \begin{cases} -1, & \text{if } x < 0, \\ 0, & \text{if } x = 0, \\ 1, & \text{if } x > 0. \end{cases} \tag{5.36}$$

Nevertheless, the temporal and spatial discretisations are introduced for the present model in a rather brief way. For more details, the interested reader is referred to, e. g. Ammann [8], Ellsiepen [78] and Rempler et al. [177].

Chapter 6:
Numerical Examples

In order to demonstrate the capability and advantage of the material model proposed in Chapter 4 and the numerical scheme presented in Chapter 5, representative numerical simulations are carried out, and the results are discussed in this chapter. The first example focuses on the transition of the flow state by examining the fluid profile in the closed fracture, the open crack, and the unbroken region. Subsequently, a two-dimensional hydraulic fracturing process is simulated, where a fracture in solid is triggered by a fluid injection. Furthermore, three main material parameters are studied for their influences on the fracturing process. The third example is concerned with a pre-fractured case, where two pre-cracks with different orientations are considered. By applying different boundary conditions to the model, the new cracks are found to propagate in distinct ways. At last, a model describing a fracking process in a three-dimensional cylindrical block is provided to demonstrate the feasibility of the developed model in practical problems.

6.1   Fluid Profile in 2 Dimensions

In order to examine the capacity of the proposed model in describing the flow transition regarding open cracks, a fluid-saturated rectangular block is set up, cf. Figure 6.1. Under plane-strain conditions, the length and width of the block are both 0.5 m. Moreover, the left and right sides are fully permeable while the top and bottom are impermeable.

According to the investigation of Hofacker [115] who studied a pure solid fracture case with linear quadrilateral elements, the minimum element size should be smaller than the length-scale parameter. In the following numerical examples, this conclusion is adopted as the criterion of the spatial discretisation. Moreover, an additional study regarding the influence of different length-scale parameters ϵ within this fluid-solid model and quadrilateral elements will later be discussed in the second example. In this model, the crack zone is divided into eight elements along the crack width, yielding a minimum element size of 1.25×10^{-3}m, which helps to exhibit the fluid profile therein more detailedly. After choosing the required material parameters as listed in Table 6.1, a horizontal pre-fractured zone with a width of 0.01 m at $x_2 = 0$ is generated as an initial crack. The complete loading process is given as follows:

STEP 1: From 0 s to 10 s, an initial pseudo-elastic energy $\mathcal{H}_0$ is applied to the predefined area, which is located precisely between $-0.25 \leq x_1 \leq 0.25$ m and $-0.005 \leq x_2 \leq 0.005$ m.

STEP 2: From 10 s to 20 s, the top edge moves upwards for 10 s with a velocity of 5×10^{-6} m/s, and thus a total vertical displacement of 5×10^{-5} m is achieved.
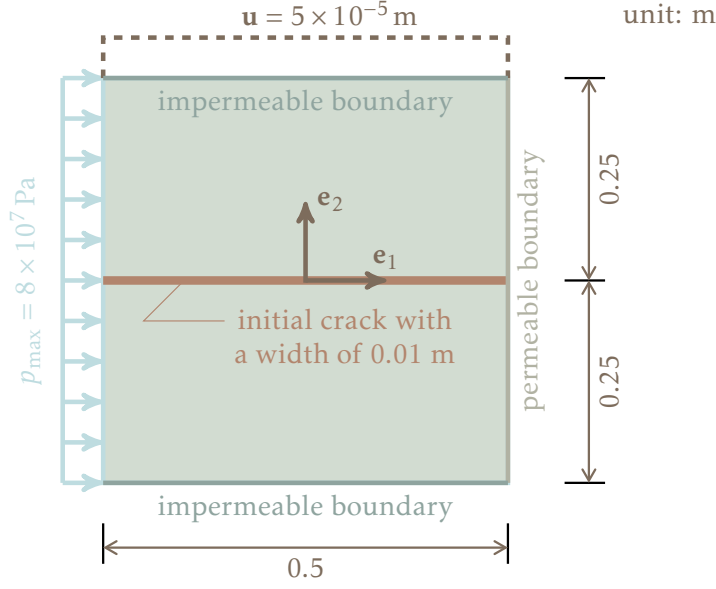
Figure 6.1: *Geometry and boundary conditions of a two-dimensional fluid-saturated porous block.*

Table 6.1: *Material parameters for the model in Section 6.1*

μ^S :	8.077×10^{10} Pa	λ^S :	12.115×10^{10} Pa	G_c :	2.7×10^3 N/m
ϵ :	1×10^{-2} m	η_r^S :	1×10^{-3}	M :	3×10^{-6} Pa $\cdot$ s
μ^{FR} :	1.002×10^3 Pa $\cdot$ s	n_0^S :	0.8	k^F :	1×10^{-8} m/s
ρ_0^{SR} :	3×10^3 kg/m^3	ρ^{FR} :	1×10^3 kg/m^3		

STEP 3: From 20 s to 100 s, the fluid is injected on the left edge under an increasing pressure with the value of $p = (t - 20) \times 10^6$ Pa. The maximum of the pressure is 8×10^7 Pa.

If (5.8) is taken into account, the pseudo-elastic energy in STEP 1 takes a value of

$$\mathcal{H}_0 = \frac{G_c}{4\,\epsilon\,(1 - \phi^S)} = 6.75 \times 10^7 \text{ J/m}^3, \tag{6.1}$$

where the material parameters of Table 6.1 have been considered, and ϕ^S has been set to 0.999. In addition, the triggering strain energy Υ_t^S is set to zero in this model and the others in this Chapter as it is not of main interest here. In STEP 2, a dilation over the whole domain is achieved under the given displacement and boundary conditions. Consequently, the COI will yield one over the whole model, allowing for a possibility of crack opening. Nevertheless, in reality, due to the vanishing resistance in the pre-cracked zone, most of the displacement occurs in that region leading to a crack opening. This opening in the proposed model is detected by a combination of the COI and the phase variable. In the last step, a fluid injection is applied to the left side of the model under an external fluid pressure that increases towards the maximum value $p_{\max}$. Regarding the
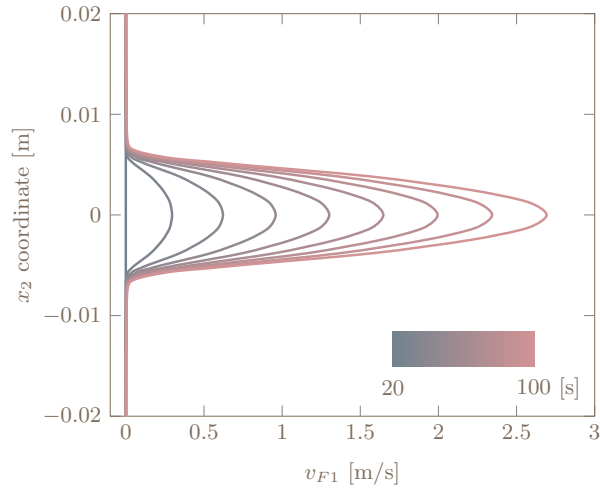
Figure 6.2: *Temporal development of the fluid velocity in the fractured region.*

boundary condition of the fluid, a horizontal layer flow is then obtained and the temporal evolution of the horizontal fluid velocity along the cross-section $x_1 = 0.01\,\mathrm{m}$ between $x_2 = -0.02\,\mathrm{m}$ and $x_2 = 0.02\,\mathrm{m}$ is shown in Fig. 6.2. It is seen that the fluid velocity is constant over the cross-section at the beginning. With an increasing pressure, the velocity profile with respect to x_2 becomes convex and the curve can be divided into three parts, corresponding to a *Darcy*-type filter flow with a rather small velocity magnitude in the region $|x_2| > 0.01\,\mathrm{m}$, a transition zone for $0.01\,\mathrm{m} > |x_2| > 0.005\,\mathrm{m}$, and a free flow in the pre-fractured zone where $|x_2| < 0.005\,\mathrm{m}$, respectively. In comparison to the *Darcy*-type flow, the free flow has a much higher velocity, indicating a transition from a *Darcy*-type flow to the *Navier-Stokes* flow. In addition, the difference becomes larger when a higher pressure is applied.

After the maximum fluid pressure is reached, the flow profile can be computed in a quasi-static setting, which is described by

$$
\begin{aligned}
v_{F1} &= -\frac{k^F}{n^F \gamma^{FR}} \frac{\partial p}{\partial x_1} \quad \text{(for the intact porous media)}, \\[2mm]
\frac{\partial^2 v_{F1}}{\partial x_2^2} &= \frac{1}{\mu^{FR}} \frac{\partial p}{\partial x_1} \qquad \text{(for the crack-opening region)},
\end{aligned}
\tag{6.2}
$$

where the vertical body force is neglected. $(6.2)_1$ is a simple expression for a *Darcy*-type flow, suggesting that the fluid velocity is proportional to the pressure gradient. In a quasi-static setting, this gradient for the present model is assumed to be constant in the $\mathbf{e}_1$ direction and yields the value of $\partial p/\partial x_1 = \Delta p/\Delta x_1 = -1.6 \times 10^8$ Pa/m after time $t > 100\,\mathrm{s}$. Correspondingly, the *Darcy*-type flow has a velocity of $v_{F1} = 8.15 \times 10^{-4}$ m/s when the parameters of Table 6.1 are used, together with $g = |\mathbf{g}| = 10$ m/s^2. In the fully fractured zone -0.005 m $\leq x_2 \leq 0.005$ m with $\phi^S = 1$, the *Navier-Stokes* flow is reduced to a Poiseuille flow with a permeable boundary condition, which describes the flow of a *Newton*ian fluid in a pipe. Considering the symmetric setting of the model, the integration of $(6.2)_2$ over the fully fractured zone provides a distribution of the fluid
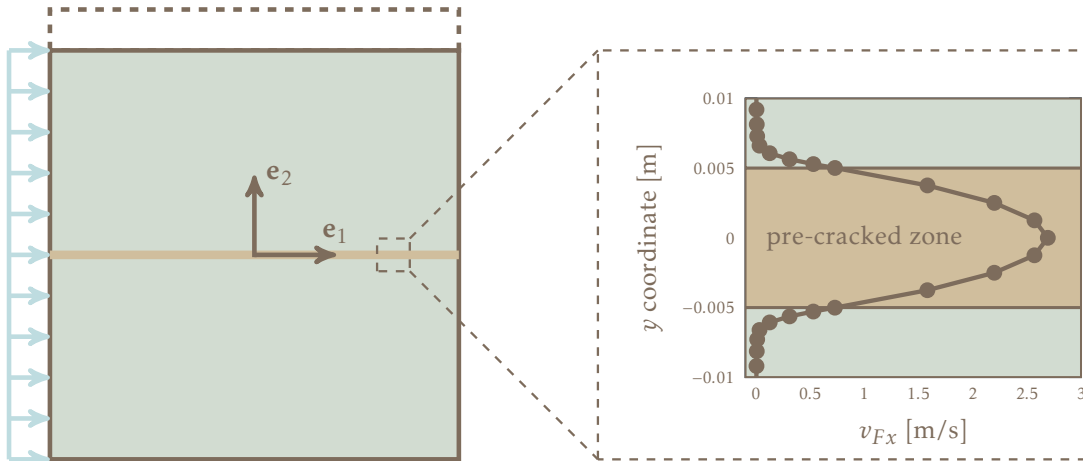
Figure 6.3: *Pore-fluid velocity profile ranging from the Darcy type to the Navier-Stokes type.*

velocity as

$$v_{F1} = -0.5 \frac{\Delta p}{\Delta x_1}(x_2)^2 + v_0 \,. \tag{6.3}$$

In order to determine the value of v_0, one may either choose the velocity at the slippery boundary $v_{F1}(x_2 = 0.005\,\text{m})$ or takes the velocity at $x_2 = 0\,\text{m}$ from the direct numerical result. As the slippery boundary is usually defined via experiments, the latter value is chosen here such that the relative distribution of the fluid velocity in the numerical result can be compared to this theoretical one.

In both Figure 6.3 and 6.4 (right), the brown solid line indicates the results from the present Finite-Element Analysis (FEA) with the dots indicating the nodal solution, while the beige solid line in Figure 6.4 represents the referential solution (Poiseuille flow) from Beavers & Joseph [18], who experimentally investigated the boundary conditions of a free flow between an impermeable top layer with a no-slip boundary condition and a naturally permeable wall. It is observed that the simulation result is in a good agreement with the referential one, thus validating that the transition of the fluid regarding the crack opening is successfully described by the proposed model.

6.2   Hydraulic Fracturing in 2 Dimensions

The second example demonstrates the capability of the developed model in describing the crack initiation and propagation in a hydraulic-fracturing process. A fluid-saturated square specimen is simulated. The geometry and boundary conditions are shown in Figure 6.5, while the material parameters remain identical to the first example, cf. 6.1. It needs to be mentioned that two loading conditions with different pressure $p(t)$ and fluid influx $\bar{v}(t)$ are studied here, respectively.

Considering the symmetric geometry and boundary conditions for the axises $x_1 = 0\,\text{m}$ and $x_2 = 0\,\text{m}$, the computation is only conducted with the top-right quarter for efficiency. The quarter is discretised into 792 quadrilateral Taylor-Hood elements, which results in a minimum element size of $h^e \approx 4 \times 10^{-3}\,\text{m}$. In the first case, a uniform fluid pressure
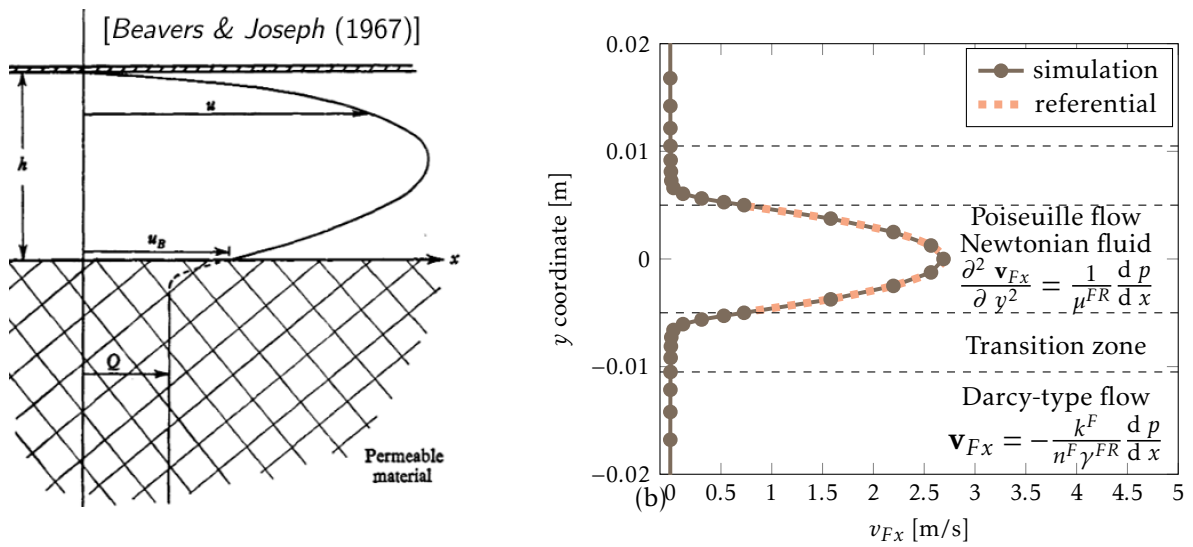
Figure 6.4: *Pore-fluid velocity profile in the fractured zone compared to the experimental study of Beavers & Joseph [18].*

with an increasing rate of $\bar{p} = 5.5 \times 10^4\,t\,\mathrm{Pa}$ is applied to the notch located at $x_2 = 0$ between $x_1 = 0\,\mathrm{m}$ and $x_1 = 0.1\,\mathrm{m}$. In Figure 6.6, the normalised principal shear stresses, computed by

$$\tau^* = \frac{\max\tau}{(\max\tau)^*} \tag{6.4}$$

where $\max\tau$ is the largest principal shear stress and $(\max\tau)^*$ the largest principal shear stress in the domain, at time $t = 2,331\,\mathrm{s}$, is demonstrated and found to be in line with the analytical solution by Sneddon [188], where the stresses around a Griffith crack in an elastic medium were investigated.

$$v^* = \log_{10}\Big(\frac{|\mathbf{v}_F|}{\min|\mathbf{v}_F|}\Big). \tag{6.5}$$
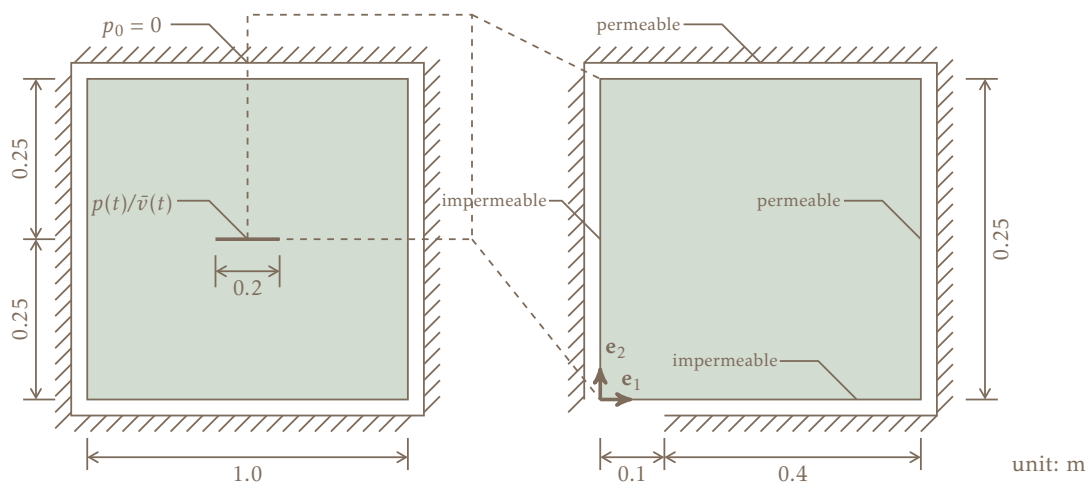

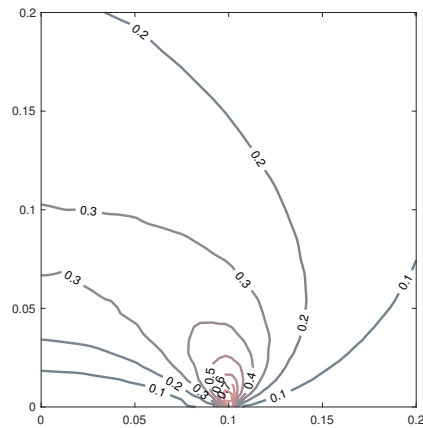**Figure 6.5:** *Geometry and boundary conditions for a two-dimensional hydraulic fracturing problem.*

Figure 6.6: *Contours of scaled principal shear stresses τ^* at $t = 2{,}331\,s$ in the vicinity of the notch.*

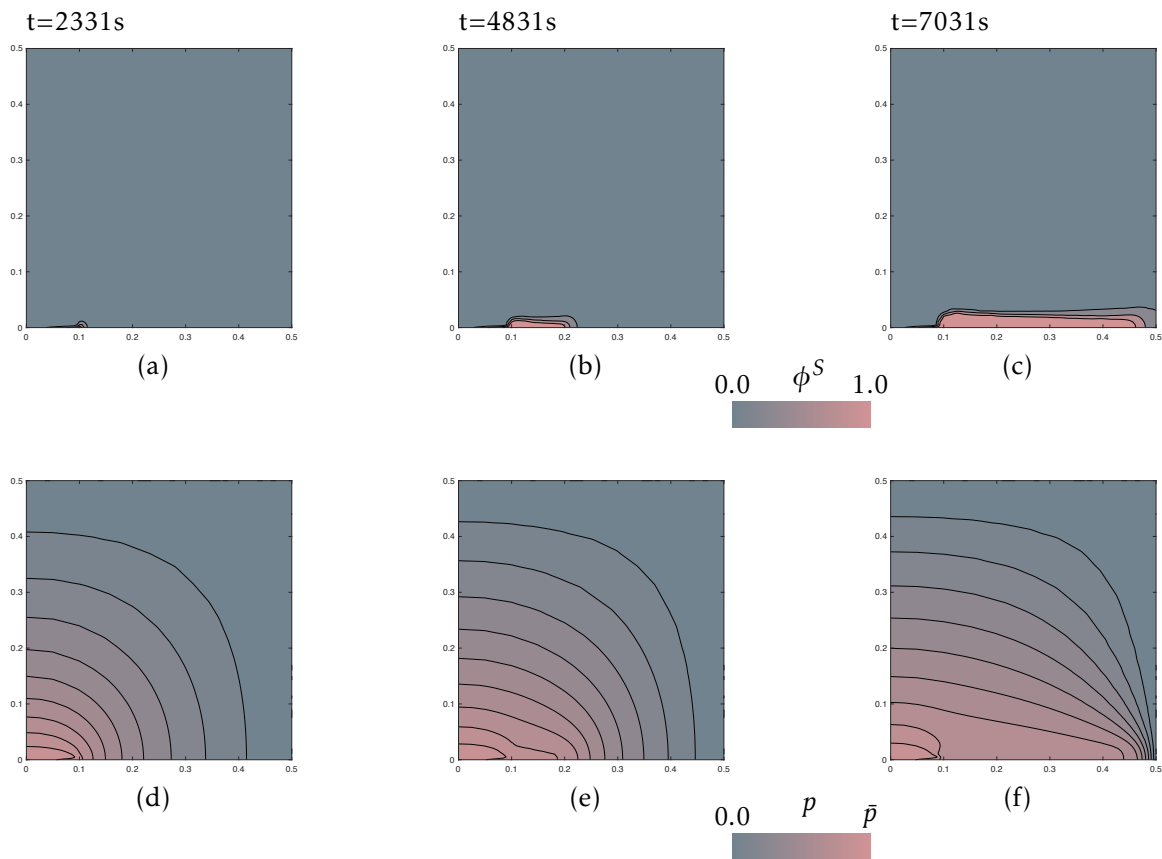**Figure 6.7:** *(a)-(c) phase variable ϕ^S (d)-(f) pore-fluid pressure p at different time steps*

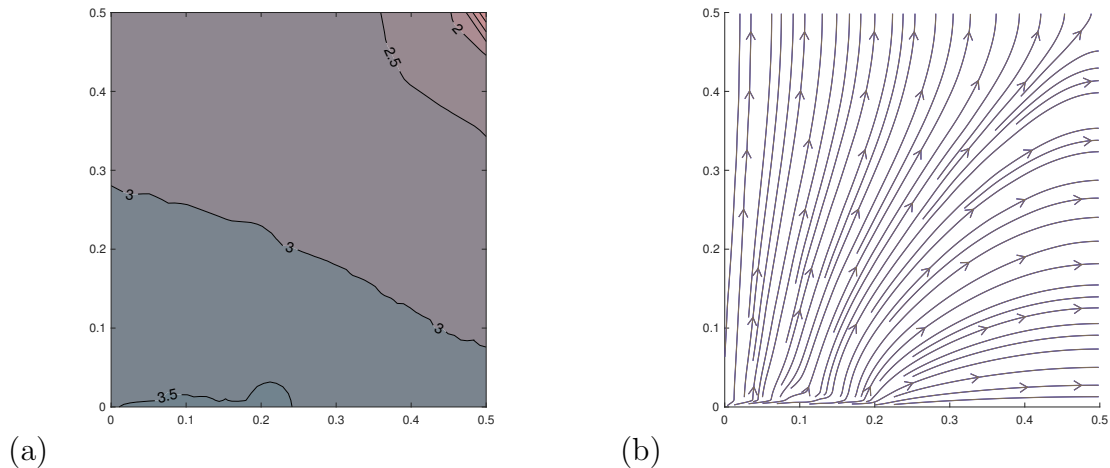(a)   (b)

Figure 6.8: *(a) contours of the scaled velocity norm v^*; (b) streamlines of the pore-fluid flow, both taken at $t = 4,831\,s$*

With an increasing pressure, the notch starts to open, and a crack is initiated at the right end of the notch. Subsequently, this crack propagates towards the right end horizontally, cf. Figure 6.7 contouring the phase variable ϕ^S in (a)-(c), and the corresponding pore pressure in (d)-(f). Immediately after applying the pore pressure, the pressure is distributed roughly radially around the notch. Owing to that the crack has not been generated yet, the fluid moves still as a *Darcy*-type filter flow, following the direction perpendicular to the pressure isolines towards the permeable boundaries. With an evolving phase field, one observes that the fluid pressure is re-distributed and the pressure within the fully fractured zone (where $\phi^S = 1$) drops much less slowly compared to the other regions, which directly results from a disappearing resistance of the solid skeleton there. This phenomenon is easily understood if one recalls the fluid momentum balance in Table 5.2 with the corresponding constitutive equations (4.59, 4.60) that describe a shrinking momentum production $\hat{\mathbf{p}}_E^F$, and in the meantime, a rising friction term div $\mathbf{T}_E^F$ regarding an increasing phase variable ϕ^S. It should be mentioned that the viscosity of the fluid is rather small here, which thus results in almost constant fluid velocity along the crack. The influence of the viscosity will be further investigated in the next example. As the fluid velocity varies within a rather big range, a scaled velocity for a clear understanding of the variation is preferred. The scaled norm is defined via (6.5). Note that $\min|\mathbf{v}_F|$ is the minimum of the norm of the fluid velocity for each time step. At time $t = 4,831\,$s, the scaled velocity, together with the streamlines, is illustrated in Figure 6.8 (a). It is seen that around the crack zone, v^* is around 3.5 and the corresponding fluid velocity is $10^{3.5} \approx 3162$ times of the minimum value 1, located at the upright corner. From Figure 6.8 (b), one discovers that the fluid flows in two main directions. It moves along the crack until reaching the joint region, then turns perpendicular to the crack and eventually approaches the permeable boundaries. Along the axis $x_2 = 0\,$m, the turning points coincide with the crack tip, as shown in Figure 6.8(b) near the bottom of the block, around $x_1 \approx 0.2\,$m.

When increasing the fluid pressure until the crack penetrates the right end, one contradiction will come to notice. As the pressure drop in the crack zone is rather small, the

fluid pressure on the right end should be more or less in the same order of the loading pressure $\bar{p}$. However, the pressure is predefined as a *Dirichlet* boundary condition, which results in a rather large pressure gradient in the vicinity. In Figure 6.10 (a), the sudden drop of the solid force at the top around time $t = 7,000\,\mathrm{s}$ is caused by this singularity issue. In this regard, another attempt is made by defining the fluid injection on the notch instead of the fluid pressure. The rate of the injection is set to $\bar{v} = 2.5^{-3}\,\mathrm{m^3/(m^2 s)}$, and the corresponding fluid pressure distribution is demonstrated in Figure 6.9.

For a pressure-driven crack propagation, additional attention has to be paid to the time instant when the crack approaches the permeable surface. Here, one problem occurs that the pressure drop in the cracked zone is rather small, meaning that p is approximately in the order of the loading pressure $\bar{p}$, while the boundary is stress-free. As a result, the computation tends towards a singularity in the pressure field, when the crack approaches
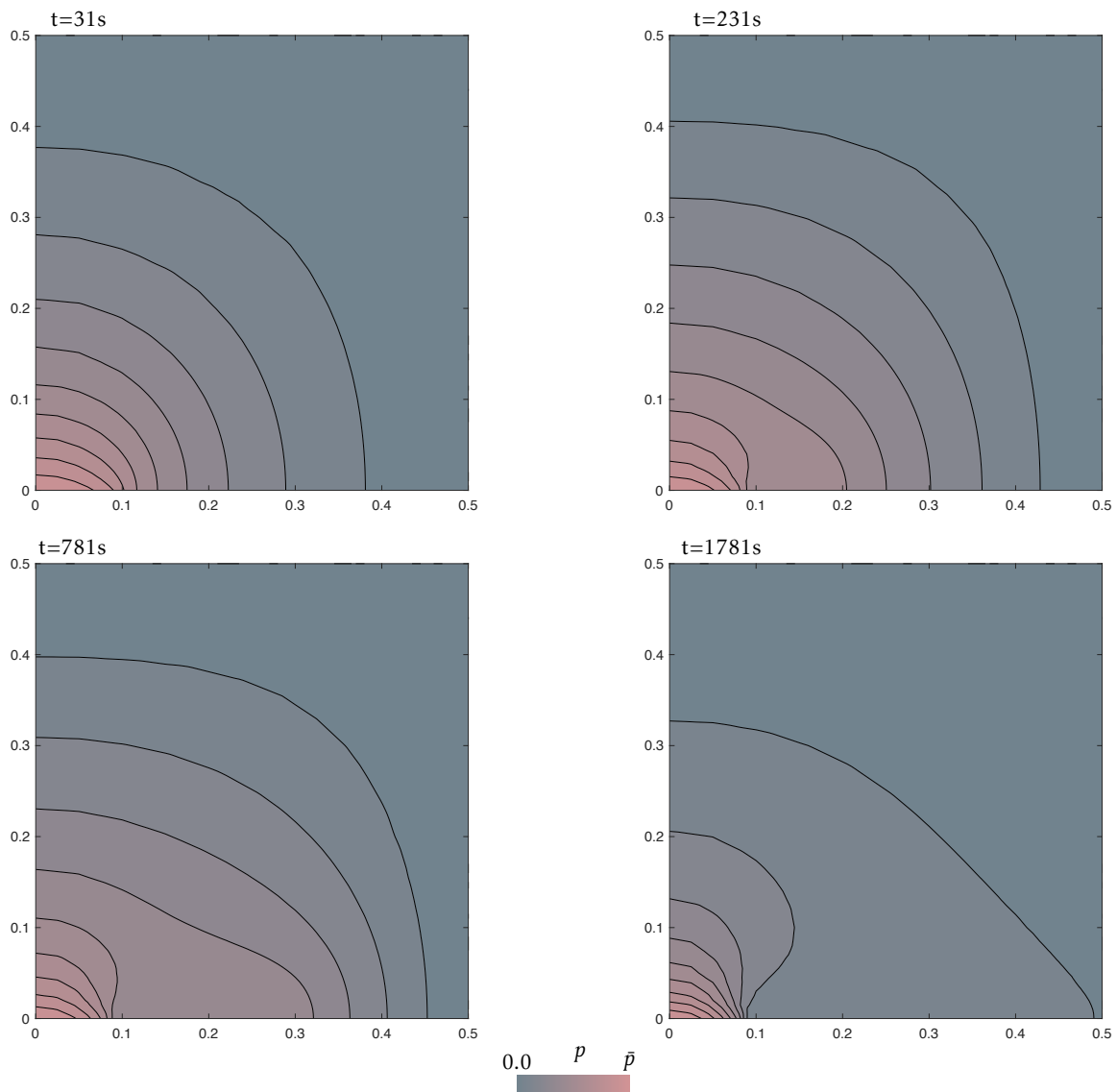

Figure 6.9: *Pressure distribution under a constant fluid influx at different time steps*

the boundary. In this regard, Figure 6.10 (a) reveals a sudden drop of the resultant solid force at the top bearing at approximately $t = 7,000$ s after having started the loading by $\bar{p}$. Consequently, the crack propagates only very slowly due to this convergence problem. In order too overcome this difficulty, the loading has been changed from pressure-driven to influx-driven by an amount of $\bar{v} = 2.5^{-3}$ m³/(m²s). This change leads to the pressure contours of Figure 6.9. Although the same boundary condition $p = 0$ is set on the right side, the convergence is achieved by reducing the fluid pressure on the notch after the crack propagates across the entire bottom. Based on this model, a few parameter studies are performed, cf. Figure 6.10. As implied in (4.60), a higher hydraulic conductivity k^F will result in a larger effective coupling term $\hat{\mathbf{p}}_E^F$ between the solid skeleton and the pore fluid in the intact saturated solid. For a fracking process, this leads to a higher maximum vertical solid force, cf. Figure 6.10 (b). In contrast, the effective dynamic viscosity of the fluid influences the coupling terms in a very limited range, compare Figure 6.10 (c). This weak correlation is due to that only after the crack is initiated, the friction term will rise, and even so, it is rather small compared to the momentum production. Besides, as a measurement of the smear crack width, the length scale parameter ϵ is the most important quantity for the solution of the problem because it governs the mean permeability of the crack zone. In other words, a greater value of ϵ corresponds to a higher permeability and a smaller solid resistance, hence resulting in a smaller vertical solid force. Vice versa, decreasing ϵ yields a higher pore pressure when pumping the same amount of water into the model. Through the momentum production, the increased fluid pressure is loaded to the solid skeleton, and a larger solid reaction force is observed, cf. Figure 6.10 (d).

6.3 Hydraulic Fracturing in 2 Dimensions with Pre-cracks under Pre-stresses

The third example is inspired by the work of Blanton [24], which investigated the hydraulic fracturing of a pre-cracked block under different settings of confined fluid pressures, cf. Figure 6.11. For the sake of simplification, a two-dimensional model under a plane-strain condition is set up here. The model is rectangular with dimensions of 1.0 m × 0.5 m. Two pre-cracks, one horizontal of 0.15 m length at the middle of the left edge and one vertical of 0.4 m length located in the middle of the block are considered. Note that the pre-cracks are both 0.01 m wide and generated by the pseudo-elastic energy of $\mathcal{H}_0 = 6.75 \times 10^7$ J/m³, the same as in the first example. For the whole computation process, the left side of the block is assumed impermeable in the meantime all other boundaries are permeable. Also, the required material parameters are again from Table 6.1, and the loading process is divided into three steps, cf. Figure 6.11, detailed as follows,

STEP 1. As in the example described in Subsection 5.1.3, a pseudo-elastic energy $\mathcal{H}_0 = 6.75 \times 10^7$ J/m³ is applied between 0 s to 10 s in the zones indicated as pre-fractured with a width of 0.01 m.

STEP 2. From 10 s to 20 s, vertical and horizontal displacements Δu_1 and Δu_2 are enforced by the application of confining pre-stresses $(\sigma_E^S)_{11}$ and $(\sigma_E^S)_{22}$ onto the
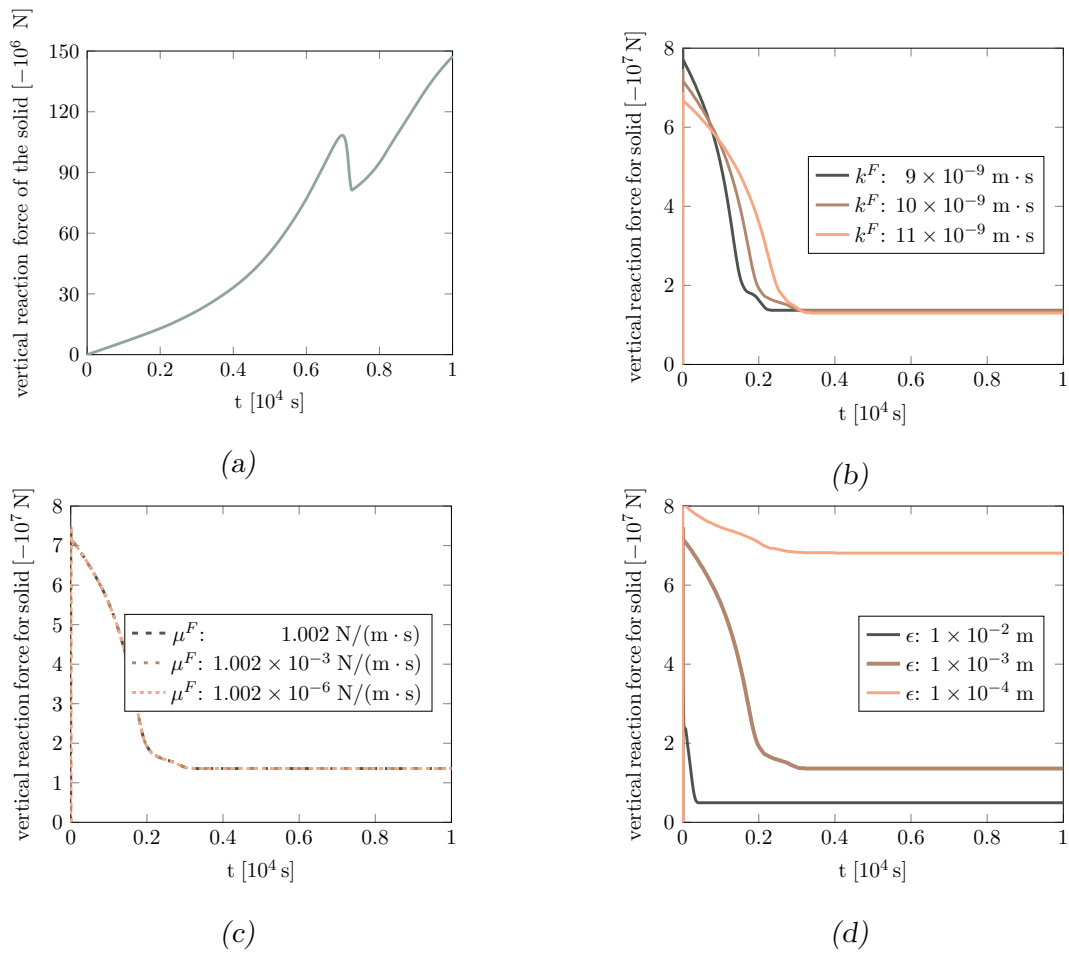
Figure 6.10: *Vertical resultant solid reaction force at the top bearing versus time: (a) under a pressure-driven loading (b)-(d) under a volume-injection-driven loading with different parameter settings*
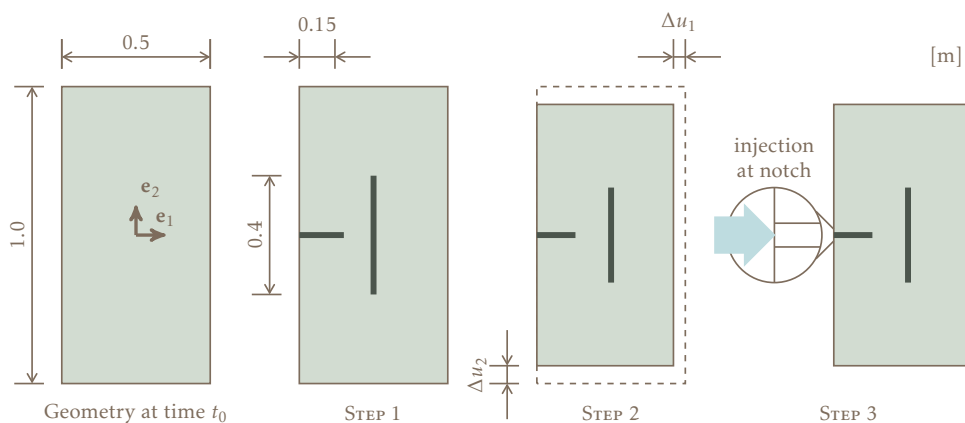

Figure 6.11: *Geometry and boundary conditions for a 2-dimensional pre-fractured model.*

solid skeleton.

STEP 3. From 20 s on, a linearly increasing fluid flux is injected at the left end of the horizontal fracture at a rate of $\bar{v} = 1 \times 10^{-3}(t - 20)$ m/s, thus initialising the hydraulic fracturing process.

Unlike a geometrical crack, for example, the notch in the second example, the pre-cracks in Step 1 are modelled by a diffusive phase-field crack. The advantage of this approach is to avoid an additional problem, i.e., the contact of the boundaries, which requires an additional numerical treatment to prevent the boundaries in a FEM model from penetration. In particular, owing to the existence of the confining stresses, the pre-cracks are usually closed and compressing normal stresses are found on both contact surfaces. Thanks to the COI, the proposed model is able to distinguish a closed crack and tackle the corresponding inverse transition from a *Navier-Stokes* flow to a *Darcy*-type without any numerical difficulty.

In Step 2, two different horizontal displacements (case 1: $\delta u_1 = 1 \times 10^{-4}$ m versus case 2: $\delta u_1 = 5 \times 10^{-4}$ m) are assumed at time $t = 20$ s while both cases have the same vertical displacements $\delta u_2 = 4 \times 10^{-5}$ m. Correspondingly, two sets of confining stresses are achieved, cf. Table 6.2, yielding a ratio $(\sigma_E^S)_{11}/(\sigma_E^S)_{22}$ with values of either 1.4 or 2.0. According to the given boundary conditions, the fluid is squeezed out from the

Table 6.2: *Vertical and horizontal displacements and pre-stresses for cases 1 and 2.*

Case No.	$\Delta u_1 / \Delta u_2$	$(\sigma_E^S)_{11}/(\sigma_E^S)_{22}$
1	2.5	1.4
2	12.5	2.0

impermeable boundary (the left side) to the permeable boundaries (the other three sides), cf. Figure 6.12, exemplarily displaying the Darcian streamlines over the whole domain for case 1 at $t = 20$ s. At the same time instant, in case 2, qualitatively similar results of the primary quantities, e. g. , streamlines, strains and stresses, are found like those in case 1 despite some quantitative differences in specific values, for example, a larger horizontal compression stress of the solid compared to that in case 1. Besides, Figure 6.12 demonstrates the evolution of the phase variable, as well as the fluid pressure ranging from low (grey-blue) to high (dusty pink).

In Step 3, with an increasing fluid injection rate, completely different hydraulic fracturing patterns are obtained at $t = 100$ s for these two cases, cf. Figure 6.13. For case 1 with a lower stress ratio, the fluid at first flows into the horizontal pre-fractured zone. Subsequently, the hydraulic fracturing is initiated at the right end of that pre-crack and propagates further rightwards until it reaches the vertical pre-crack. Afterwards, the fluid mainly flows along this vertical pre-cracked zone, and at both ends, two wing-like hydraulic fractures are formed up. In the meanwhile, the rest fluid seeps out in the direction perpendicular to the fracture isolines through the fluid-saturated porous solid towards the permeable boundaries. During the whole process, the streamlines, the turning point of which is consistent with the tip of the newly generated crack, always corresponds the hydraulic fracture propagation.
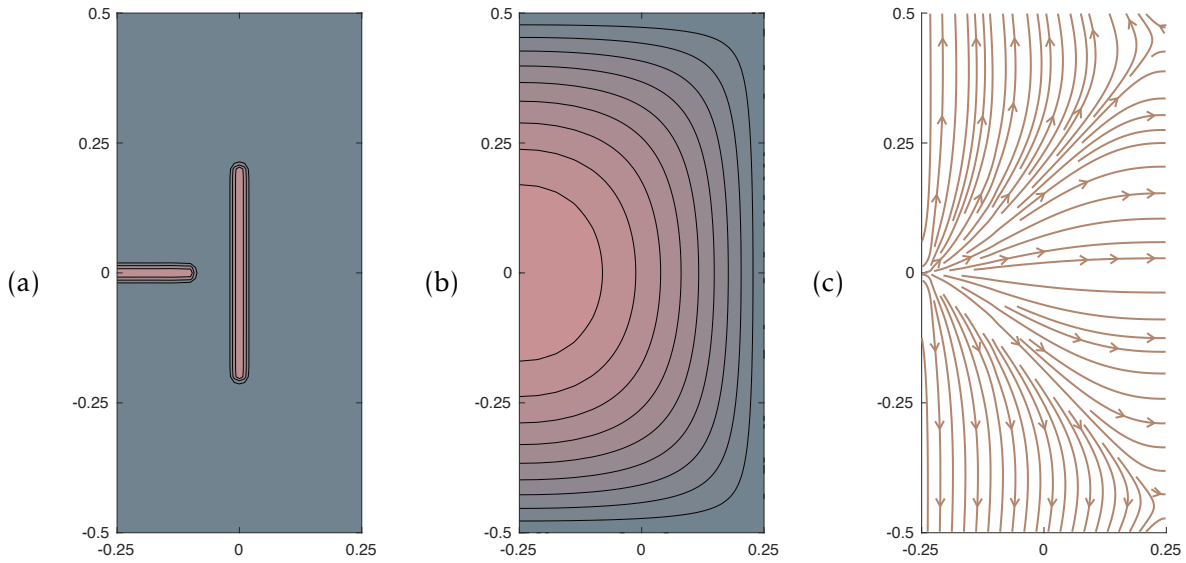
Figure 6.12: *(a) pre-crack patterns (b) pore-fluid pressure (c) streamlines of the fluid flow at*
t = 20 s (case 1).

In contrast, case 2 exhibits a different fracturing pattern where the hydraulic fracture
propagates directly across the model along the axis $x_2 = 0$, which usually occurs for the
completely intact model. It is also observed that the streamlines mainly diverge into two
directions, one along the hydraulic fracture and the other perpendicular to that crack,
similar to the result in the second example.

These two patterns are also observed experimentally by Blanton [24], who investigated
the propagation of hydraulic fracturing in pre-fractured shale blocks. In his research, he
concluded that the hydraulic fracture tends to cross the pre-crack only when the horizontal
stress is much higher than the vertical one. Contrariwise, the hydraulic fracture will
be "arrested" by the open pre-cracks. With reference to the experimental results, the
effect of the confining-stress conditions on the numerical results can be interpreted by
examining the streamlines and the fluid pressure contours in Figure 6.13. In case 1,
the fluid pressure in the vertical pre-fractured zone is almost the same as the one at
the injection point, indicating that the fluid flows without any resistance from the solid
skeleton. This occurrence is only possible if the cracks on this routine, including the
horizontal and the vertical pre-cracks and the adherent hydraulic fractures, are all open.
In opposition, case 2 displays an even fluid pressure only along the horizontal and hydraulic
fracturing. The pressure gradient in the vertical pre-fractured zone is consistent to the
one of its neighbour, suggesting that the fluid pressure there drops as an unbroken porous
medium and the vertical pre-crack is closed in this model.

The results confirm that the present model is in a good agreement with the experimen-
tal observations. Thus, this example illustrates the capacity of the developed model in
tackling the hydraulic fracturing problem under pre-cracks and pre-stresses conditions.
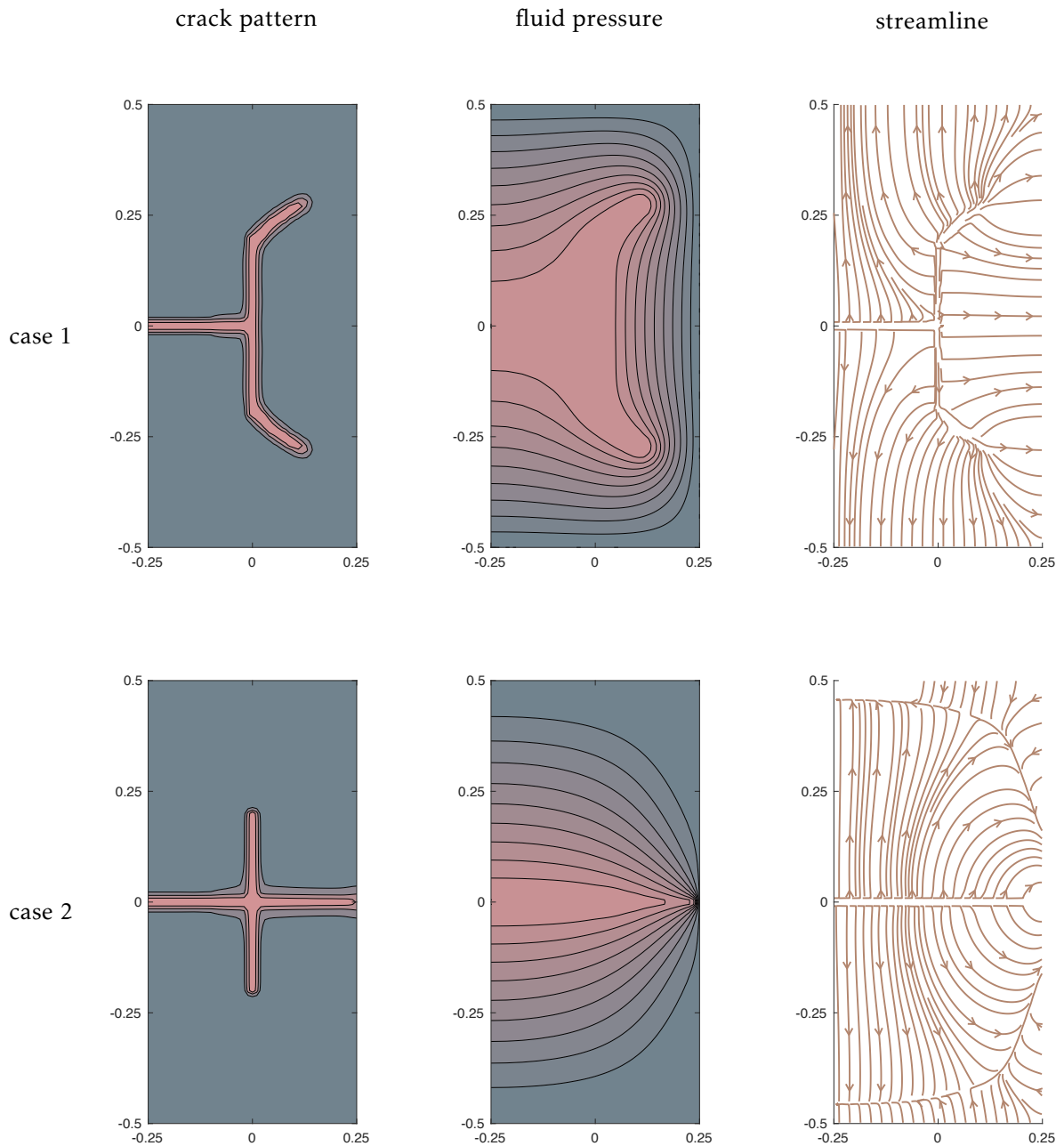
Figure 6.13: *Comparisons of the hydraulic-crack patterns, the fluid pressure and the streamlines of the fluid flow between case 1 and case 2.*

6.4 Hydraulic Fracturing in 3 Dimensions

The last example aims to show the performance of the proposed model in handling full-dimensional fracking problems. Regarding this, a fully three-dimensional example of a fluid-saturated cylindrical specimen with an outer radius $R_1 = 1\,\mathrm{m}$ and a height $H_1 = 1\,\mathrm{m}$ is under consideration, see Figure 6.14. The specimen is fixed at the top and bottom

surfaces but freely expandable in the middle. Moreover, the fracking fluid is injected through a rigid borehole, located at the middle of the top surface and drilled downwards with a radius $R_0 = 0.1$ m and a depth $H_0 = 0.5$ m, and enters into the specimen by the bottom of the borehole with an injection rate of 5×10^{-2} m^3/(m^2 s). All the surfaces except the bottom of the borehole and the bottom of the cylinder are assumed impermeable. The bottom of the cylinder allows the fluid to pass by freely under a zero ambient pressure $p = 0$ Pa. Note that both the geometry and the boundary conditions are axial-symmetric. Thus, in order to simplify the numerical model, only a quarter of the complete structure is simulated with an appropriate BC setting on the cross-sections. The quarter model is discretised into 2350 quadrilateral Taylor-Hood elements, resulting in 11,118 nodes and 105,636 degrees of freedom. The minimum mesh size is around 0.01 m, $h^e \approx 0.01$ m, which is located in the vicinity of the potential crack zone. The material parameters are consistent with the previous numerical examples, as shown in Table 6.1.
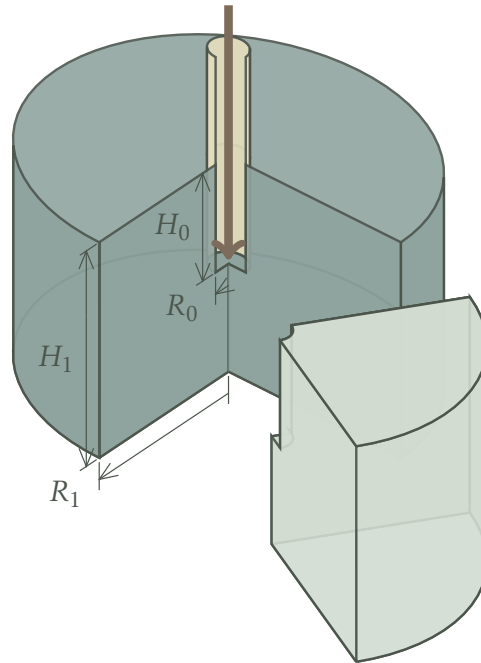

Figure 6.14: *Geometry of a three-dimensional fracturing model.*

In order to distinctly exhibit the transition of the fluid type with the evolution of the phase-field variable, the cracked zone with $\phi^S > 0.9$, denoted by a pastel pink surface, together with the streamlines of the cross-sections, is shown from an anterolateral view, cf. Figure 6.15. It is observed that the fluid within the crack zone flows along the crack surface, depart from which the rest flows towards the permeable boundaries. For example, the streamlines starting from the bottom the borehole, proceed directly downwards to the bottom boundary while the part of the fluid in the crack leaves the crack surface upwards at first and then bends downwards in a parabolic way, approaching the side and bottom boundaries. Furthermore, a volumetric dilation is noticed as a direct result of the injected fluid.
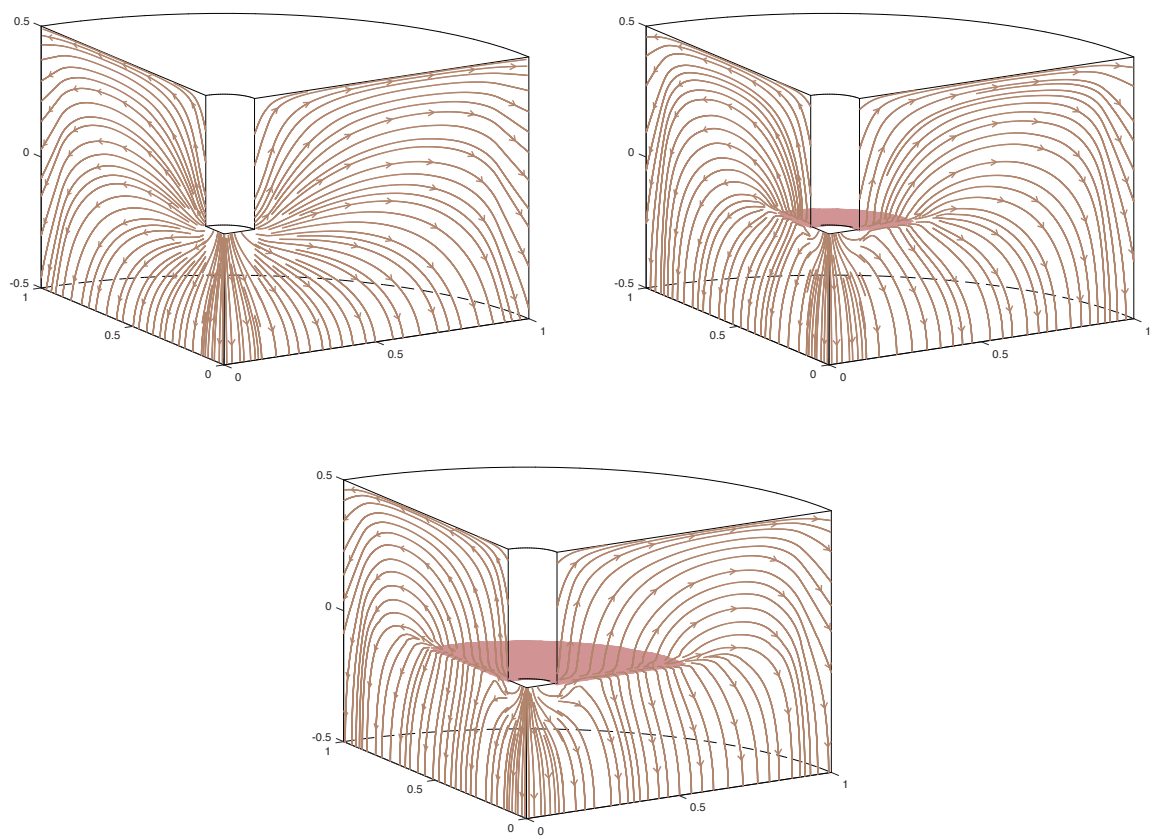
Figure 6.15: *Propagation of the crack surface together with the streamlines.*

Chapter 7:
Summary and Outlook

7.1   Summary

This monograph presents a thermodynamically consistent model for describing dynamic brittle fracture in porous media. This model has been achieved by embedding the phase-field approach into the well-established TPM. The derived model has been further implemented in the in-house FE-software (PANDAS) and applied to hydraulic fracturing problems. Numerical results of two- and three-dimensional examples have demonstrated the capacity and effectiveness of the developed model.

Proceeding from the TPM, each constituent owns its independent balance equations which are related to each other by the production terms accounting for the mutual effects between them. After applying several reasonable and necessary assumptions such as the absence of thermal effects, the entropy inequality guaranteeing the thermodynamical consistency is derived. Furthermore, an overview of the state-of-the-art fracture modelling in solid mechanics was carried out where the phase-field fracture approach stood out owing to its capacity in the description of complex crack phenomena and the ease in numerical implementation. Thus, the remaining work is to introduce the phase variable into the TPM while maintaining the thermodynamic consistency. Herein, a biphasic material composed of solid and fluid was focused on the model formulation. Before proposing suitable constitutive equations, two essential ingredients of phase-field modelling of fracturing solids were discussed and accommodated to porous media problems, including (i) the decomposition of the solid strain tensor to ensure that the material fractures only owing to the accumulation of the energy induced by tensile stresses and the resistance degrades only in the directions where tension occurs; and (ii) the introduction of the history variable recording the maximum over-threshold energy in the evolution equations of the phase field. More important is that the evolution equation of the phase field was considered to be solely dependent on the solid stored strain energy since cracks only occur in solid and the fluid-induced pressure can be regarded as an external load of the solid skeleton and has already been taken into account by the production term. Subsequently, the fluid in the generated cracks was treated. Owing to the lack of solid resistance, the fluid in the crack zone flows as a free flow in a pipe. If assuming a *Newton*ian fluid, the flow can be described as a Poiseuille flow. In this regard, the phase variable was also introduced into the constitutive equations for the fluid momentum production and effective fluid stress such that the momentum production disappears in the crack zone while the effective fluid stress arises. In the meantime, the fluid momentum balance is transformed from a standard form of *Darcy*'s law into the *Navier-Stokes* equation.

Further addressed were the issues concerning applying the developed model to more realistic hydraulic fracturing problems. The nature of a phase-field crack is to substitute a real crack by a material with zero or very little resistance in that region. Although this

approach preserves the structure and corresponding mesh, one of the main drawbacks is the loss of the geometry of cracks, especially, of crack surfaces. As crack is interpreted as a material state (cracked) indicated by the phase variable and the evolution of this phase variable is monotonic, the missing geometrical information may lead to inconsistency in complex cases, for example, the re-closing of the pre-existing cracks under confining stresses. This inconsistency is because when cracks close after opening, the phase variable stays for a cracked material and the fluid momentum production remains vanishing. Based on this finding, a new concept, the Crack-Opening Indicator was defined. Thus, besides the phase variable characterising the intact and cracked material, the indicator additionally distinguishes the cracked material from two states, namely closed and open cracks. Afterwards, the constitutive equations for the fluid were redefined such that the production terms vanish and the effective fluid stress comes into play only when there is a crack and this crack is open.

With all those ingredients, the proposed model has been made capable of describing the most important phenomena of hydraulic fracturing, which involves not only the monotonic crack generation in the solid but also the bidirectional transition of the fluid states between a *Navier-Stokes* bulk flow and a *Darcy*-type filter flow. The derived strongly coupled partial differential equations were then solved under a standard FEM procedure. After yielding the weak form of the governing equations, a spatial discretisation with mixed finite elements and an implicit *Euler* time integration scheme are applied. Subsequently, a monolithic solution was achieved by the in-house FE-software PANDAS. Numerical simulations were performed to demonstrate the capacity of the proposed model in describing typical hydraulic fracturing processes with either pressure-driven or volume-driven loadings. In these cases, the solid stress state around the crack tip has been found in good agreement with the theoretical deduction while the fluid profiles in the open crack zone are consistent to the findings based on Poiseuille flow. In addition, complex scenarios involving pre-existing fractures and pre-stressed situations were also investigated. For two models with identical geometries and materials under the same loading cases, different crack patterns were obtained with respect to two combinations of horizontal and vertical confined stresses. These phenomena were also discovered by experiments in the 1980s.

7.2 Outlook

Although the present monograph proves that a phase-field model embedded in the TPM is capable of solving complex hydraulic fracturing problem, the potential of this combination has not been fully exploited. Considering the attempts of Aldakheel [3] and Ambati et al. [5] in setting up a phase-field model to ductile fracture, it will not be astonishing to further extend the current model to ductile hydraulic fracturing, which is suitable to describe many geomechanical phenomena, for example, the landslide. Recently, a study of replacing the fracking fluid with supercritical CO_2 has become attractive due to the great benefit compared to the traditional fracking fluid involving only the decrease of environmental pollution but also the increase of the gas production, cf. Middleton [152]. In this regard, an extension from a biphasic model towards a tri-phasic material is desirable. Since the temperature plays a significant role for the gas and the viscosity

of the fracking fluid and its sand-carrying capability are very temperature-sensitive, a thermodynamical TPM model has to be considered. The largest challenge comes from the phase transition of the gas owing to the in-situ high-pressure high-temperature condition of the underground hydraulic fracturing region. During the injection process, the liquid carbon dioxide begins to vaporise after reaching the supercritical temperature with the increasing temperature, thereby forming a carbon dioxide foam with the water-based fracking fluid. The supercritical CO2 has similar behaviour of the gas and will return to the ground in a gaseous form with the decreasing pressure. As the phase-field model was successfully applied to the phase-transition problem, it is possible to define two phase variables describing the crack phenomena in the solid and the vaporisation of the CO2, respectively.

Apart from the diversity in the material model, improvement is also expected in the numerical methods. As the mesh size is always controlled by the length-scale parameter and this parameter is usually rather small compared to the size of the model, a very fine mesh at least around the crack tip is thus always required. However, the crack tip moves as the crack propagates, which causes a fine mesh along the predicted crack path by a standard FEM. An adaptive mesh refinement will considerably reduce the number of the elements and the resulting degrees of freedom if the fine mesh follows the movement of the crack tip, especially for three-dimensional problems.

Appendix A:
Selected Relations of Tensor Calculus

This appendix complements the monograph by providing the fundamental rules and relations that are necessary and frequently recalled in this main context. Those supplements are provided in the form of "handbook", and hence, a detailed derivation is unfortunately neglected. For a comprehensive introduction, the interested reader is referred to the textbook of de Boer [25], whose notation is followed here. The full mathematical deduction can be found in Marsden & Hughes [149]. Additionally, a compact summary is also available in the online lecture notes of the Institute of Applied Mechanics (Chair of Continuum Mechanics) at the University of Stuttgart, cf. Ehlers [76], which involves the following content.

A.1 Tensor Algebra

As a conventional notation, set $\{\alpha, \beta\} \in R$ to be arbitrary rational scalar quantities, $\{\mathbf{a}, \mathbf{b}, \mathbf{c}, \mathbf{d}\} \in \mathcal{V}^3$ be arbitrary vectors of the proper *Euclid*ean[1] 3D vector space $\mathcal{V}^3$, and $\{\mathbf{A}, \mathbf{B}, \mathbf{C}, \mathbf{D} \in \mathcal{V}^3 \otimes \mathcal{V}^3\}$ be arbitrary second-order tensors of the corresponding dyadic product space.

A.1.1 Selected rules for second-order tensors

Products of tensors with scalars or vectors:

$$\alpha(\beta)\mathbf{A} = (\alpha\beta)\mathbf{A} \qquad \text{: associate law}$$

$$\mathbf{A}(\alpha\,\mathbf{a}) = \alpha(\mathbf{A}\mathbf{a}) = (\alpha\mathbf{A})\mathbf{a} \qquad \text{: associate law}$$

$$(\alpha + \beta)\mathbf{A} = \alpha\mathbf{A} + \beta\mathbf{A} \qquad \text{: distributive law}$$

$$\alpha(\mathbf{A} + \mathbf{B}) = \alpha\mathbf{A} + \alpha\mathbf{B} \qquad \text{: distributive law}$$

$$\mathbf{A}(\mathbf{a} + \mathbf{b}) = \mathbf{A}\mathbf{a} + \mathbf{A}\mathbf{b} \qquad \text{: distributive law}$$

$$(\mathbf{A} + \mathbf{B})\mathbf{a} = \mathbf{A}\mathbf{a} + \mathbf{B}\mathbf{a} \qquad \text{: distributive law}$$

$$\alpha\mathbf{A} = \mathbf{A}\alpha \qquad \text{: commutative law}$$

$$\mathbf{a} = \mathbf{A}\mathbf{b} \qquad \text{: linear mapping}$$

$$\mathbf{I}\mathbf{a} = \mathbf{a} \qquad \mathbf{I}\text{: second-order identity tenor}$$

$$\mathbf{0}\mathbf{a} = \mathbf{0} \qquad \mathbf{0}\text{: zero tensor}$$

---

[1] *Euclid of Alexandria* (Mid-4th century BC - Mid-3th century BC): Greek mathematician, often regarded as the "founder of geometry".

Scalar (Inner) product of tensors:

$$(\alpha \mathbf{A}) \cdot \mathbf{B} = \mathbf{A} \cdot (\alpha \mathbf{B}) = \alpha (\mathbf{A} \cdot \mathbf{B}) \quad : \text{associate law}$$
$$\mathbf{A} \cdot (\mathbf{B} + \mathbf{C}) = \mathbf{A} \cdot \mathbf{B} + \mathbf{A} \cdot \mathbf{C} \quad : \text{distributive law}$$
$$\mathbf{A} \cdot \mathbf{B} = \mathbf{B} \cdot \mathbf{A} \quad : \text{commutative law}$$
$$\mathbf{A} \cdot \mathbf{B} = 0 \quad \forall \mathbf{A}, \text{ if } \mathbf{B} \equiv \mathbf{0}$$
$$\mathbf{A} \cdot \mathbf{A} > 0 \quad \forall \mathbf{A} \neq \mathbf{0}$$
$$\mathbf{A} \cdot (\mathbf{a} \otimes \mathbf{b}) = \mathbf{a} \cdot (\mathbf{A}\mathbf{b})$$

Tensor product of tensors:

$$\alpha(\mathbf{A}\mathbf{B}) = (\alpha \mathbf{A})\mathbf{B} = \mathbf{A}(\alpha \mathbf{B}) \quad : \text{associate law}$$
$$(\mathbf{A}\mathbf{B})\mathbf{a} = \mathbf{A}(\mathbf{B}\mathbf{a}) \quad : \text{associate law}$$
$$(\mathbf{A}\mathbf{B})\mathbf{C} = \mathbf{A}(\mathbf{B}\mathbf{C}) \quad : \text{associate law}$$
$$\mathbf{A}(\mathbf{B} + \mathbf{C}) = \mathbf{A}\mathbf{B} + \mathbf{A}\mathbf{C} \quad : \text{distributive law}$$
$$(\mathbf{A} + \mathbf{B})\mathbf{C} = \mathbf{A}\mathbf{C} + \mathbf{B}\mathbf{C} \quad : \text{distributive law}$$
$$\mathbf{A}\mathbf{B} \neq \mathbf{B}\mathbf{A} \quad : \textbf{non}\text{-commutative law}$$
$$\mathbf{I}\mathbf{A} = \mathbf{A} \quad \mathbf{I}: \text{second-order identity tensor}$$
$$\mathbf{0}\mathbf{A} = \mathbf{0} \quad \mathbf{0}: \text{zero tensor}$$

Transposed tensor:

$$(\mathbf{a} \otimes \mathbf{b})^T = (\mathbf{b} \otimes \mathbf{a}) \qquad (\alpha \mathbf{A})^T = \alpha \mathbf{A}^T$$
$$(\mathbf{A}\mathbf{B})^T = \mathbf{B}^T \mathbf{A}^T \qquad \mathbf{a} \cdot (\mathbf{A}\mathbf{b}) = (\mathbf{A}^T \mathbf{a}) \cdot \mathbf{b}$$
$$\mathbf{A} \cdot (\mathbf{B}\mathbf{C}) = (\mathbf{B}^T \mathbf{A}) \cdot \mathbf{C} \qquad (\mathbf{A} + \mathbf{B})^T = \mathbf{A}^T + \mathbf{B}^T$$

Definition of determinant and cofactor:

$$\det \mathbf{A} = \frac{1}{6}(\mathbf{A} \ast\!\!\ast \mathbf{A}) \cdot \mathbf{A} = \frac{1}{6}(\operatorname{tr} \mathbf{A})^3 - \frac{1}{2}(\operatorname{tr} \mathbf{A})(\mathbf{A}^T \cdot \mathbf{A}) + \frac{1}{3}(\mathbf{A}\mathbf{A})^T \cdot \mathbf{A}$$

$$\operatorname{cof} \mathbf{A} = \frac{1}{2}\mathbf{A} \ast\!\!\ast \mathbf{A}, \text{ where } \operatorname{cof} \mathbf{A} = \frac{1}{2}(a_{ik}a_{no}e_{inj}e_{kop})(\mathbf{e}_j \otimes \mathbf{e}_p) := \overset{+}{a}_{jp}(\mathbf{e}_j \otimes \mathbf{e}_p)$$

Inverse tensor:

$$\mathbf{A}^{-1} = (\det \mathbf{A})^{-1}\operatorname{adj} \mathbf{A} = (\det \mathbf{A})^{-1}(\operatorname{cof} \mathbf{A})^T \to \mathbf{A}^{-1} \text{ exists if } \det \mathbf{A} \neq 0$$
$$\mathbf{A}\mathbf{A}^{-1} = \mathbf{A}^{-1}\mathbf{A} = \mathbf{I}$$
$$(\mathbf{A}^{-1})^T = (\mathbf{A}^T)^{-1} =: \mathbf{A}^{T-1} = \mathbf{A}^{-T}$$
$$(\mathbf{A}\mathbf{B})^{-1} = \mathbf{B}^{-1}\mathbf{A}^{-1}$$

Trace operator:

$$\begin{aligned}
\operatorname{tr}\mathbf{A} &= \mathbf{A}\cdot\mathbf{I} \\
\operatorname{tr}(\alpha\mathbf{A}) &= \alpha\operatorname{tr}\mathbf{A} \\
\operatorname{tr}(\mathbf{a}\otimes\mathbf{b}) &= \mathbf{a}\cdot\mathbf{b} \\
\operatorname{tr}\mathbf{A} &= \operatorname{tr}\mathbf{A}^T \\
\operatorname{tr}(\mathbf{A}\mathbf{B}) &= \operatorname{tr}(\mathbf{B}\mathbf{A}) = \mathbf{A}\cdot\mathbf{B} = \mathbf{B}\cdot\mathbf{A} \\
\operatorname{tr}(\mathbf{A}\mathbf{B}\mathbf{C}) &= \operatorname{tr}(\mathbf{B}\mathbf{C}\mathbf{A}) = \operatorname{tr}(\mathbf{C}\mathbf{A}\mathbf{B})
\end{aligned}$$

Determinant operator:

$$\begin{aligned}
\det\mathbf{A}^T &= \det\mathbf{A} & \det\mathbf{A}^{-1} &= (\det\mathbf{A})^{-1} \\
\det(\mathbf{A}\mathbf{B}) &= \det\mathbf{A}\,\det\mathbf{B} & \det(\alpha\mathbf{A}) &= \alpha^3\det\mathbf{A} \\
\det\mathbf{I} &= 1 & \det(\mathbf{A}+\mathbf{B}) &= \det\mathbf{A} + (\operatorname{cof}\mathbf{A})\cdot\mathbf{B}+ \\
& & & \quad +\mathbf{A}\cdot(\operatorname{cof}\mathbf{B}) + \det\mathbf{B}
\end{aligned}$$

A.1.2   Selected rules for higher-order tensors

Third-order fundamental ($Ricci^2$) tensor:

$$\overset{3}{\mathbf{E}} = e_{ijk}\mathbf{e}_1\otimes\mathbf{e}_2\otimes\mathbf{e}_3 \quad \text{with the "permutation symbol" } \mathbf{e}_{ijk}$$

$$\mathbf{e}_{ijk} = \begin{cases} 1 & : \text{ even permutation} \quad, \text{e. g. } e_{123}=e_{231}=e_{312}=1 \\ -1 & : \text{ odd permutation} \quad, \text{e. g. } e_{321}=e_{213}=e_{132}=-1 \\ 0 & : \text{ double index} \end{cases}$$

Cross product:

$$\begin{aligned}
\mathbf{a}\times\mathbf{b} &= \overset{3}{\mathbf{E}}(\mathbf{a}\otimes\mathbf{b}) \\
\mathbf{a}\times\mathbf{B} &= [\overset{3}{\mathbf{E}}(\mathbf{a}\otimes\mathbf{B})]^{\underline{2}} \\
\mathbf{A}\times\mathbf{B} &= \overset{3}{\mathbf{E}}(\mathbf{A}\mathbf{B}^T) \\
\mathbf{I}\times\mathbf{A} &= \overset{3}{\mathbf{E}}\mathbf{A}^T = 2\overset{A}{\mathbf{a}} \quad \text{with } \overset{A}{\mathbf{a}} := \tfrac{1}{2}\overset{3}{\mathbf{E}}\mathbf{A}^T \quad (\overset{A}{\mathbf{a}} \text{ is the axial vector of } \mathbf{A})
\end{aligned}$$

Fourth-order fundamental tensors:

$$\begin{aligned}
\overset{4}{\mathbf{I}} := (\mathbf{I}\otimes\mathbf{I})^{\overset{23}{T}} &\rightarrow (\mathbf{I}\otimes\mathbf{I})^{\overset{23}{T}}\mathbf{A} = \mathbf{A} & &: \text{identical map} \\
(\mathbf{I}\otimes\mathbf{I})^{\overset{24}{T}} &\rightarrow (\mathbf{I}\otimes\mathbf{I})^{\overset{24}{T}}\mathbf{A} = \mathbf{A}^T & &: \text{transposing map} \\
\mathbf{I}\otimes\mathbf{I} &\rightarrow (\mathbf{I}\otimes\mathbf{I})\mathbf{A} = (\mathbf{A}\cdot\mathbf{I})\mathbf{I} & &: \text{tracing map}
\end{aligned}$$

---

[2] *Gregorio Ricci-Curbastro* (1853-1925): Italian mathematician.

Note that the transposition operator $(\,\cdot\,)^{\overset{ij}{T}}$ exchanges the positions of the i-th and j-th basis vectors. Moreover, the transpose of a fourth-order tensor is defined as

$$\overset{4}{\mathbf{A}}{}^{T} = (\overset{4}{\mathbf{A}}{}^{\overset{13}{T}})^{\overset{24}{T}}$$

Properties of **simple** fourth-order tensors:

$$(\mathbf{A} \otimes \mathbf{B})^{\overset{23}{T}} = (\mathbf{B}^T \otimes \mathbf{A}^T)^{\overset{14}{T}}$$

$$[(\mathbf{A} \otimes \mathbf{B})^{\overset{23}{T}}]^T = (\mathbf{A}^T \otimes \mathbf{B}^T)^{\overset{23}{T}}$$

$$[(\mathbf{A} \otimes \mathbf{B})^{\overset{23}{T}}]^{-1} = (\mathbf{A}^{-1} \otimes \mathbf{B}^{-1})^{\overset{23}{T}}$$

$$((\mathbf{A} \otimes (\mathbf{B})^{\overset{24}{T}} = [((\mathbf{B} \otimes (\mathbf{A})^{\overset{13}{T}}]^T$$

$$[((\mathbf{A} \otimes (\mathbf{B})^{\overset{24}{T}}]^T = ((\mathbf{B} \otimes (\mathbf{A})^{\overset{24}{T}}$$

$$[((\mathbf{A} \otimes (\mathbf{B})^{\overset{24}{T}}]^{-1} = ((\mathbf{B}^{T-1} \otimes (\mathbf{A}^{T-1})^{\overset{24}{T}}$$

Other related rules:

$$(\mathbf{A} \otimes \mathbf{B})^{\overset{23}{T}}(\mathbf{C} \otimes \mathbf{D})^{\overset{23}{T}} = (\mathbf{AC} \otimes \mathbf{BD})^{\overset{23}{T}}$$

$$(\mathbf{A} \otimes \mathbf{B})^{\overset{23}{T}}(\mathbf{C} \otimes \mathbf{D}) = (\mathbf{ACB}^T \otimes \mathbf{D})$$

$$(\mathbf{A} \otimes \mathbf{B})(\mathbf{C} \otimes \mathbf{D})^{\overset{23}{T}} = (\mathbf{A} \otimes \mathbf{C}^T\mathbf{BD})$$

$$(\mathbf{A} \otimes \mathbf{B})^{\overset{23}{T}}\mathbf{C} = \mathbf{ACB}^T$$

$$(\mathbf{A} \otimes \mathbf{B})^{\overset{23}{T}}\mathbf{a} = [\mathbf{A} \otimes (\mathbf{Ba})]^{\overset{23}{T}}$$

$$(\mathbf{A} \otimes \mathbf{B})^{\overset{24}{T}}(\mathbf{C} \otimes \mathbf{D})^{\overset{24}{T}} = (\mathbf{AD}^T \otimes \mathbf{B}^T\mathbf{C})^{\overset{23}{T}}$$

$$(\mathbf{A} \otimes \mathbf{B})^{\overset{23}{T}}(\mathbf{C} \otimes \mathbf{D})^{\overset{24}{T}} = (\mathbf{AC} \otimes \mathbf{DB}^T)^{\overset{24}{T}}$$

$$(\mathbf{A} \otimes \mathbf{B})^{\overset{24}{T}}(\mathbf{C} \otimes \mathbf{D})^{\overset{23}{T}} = (\mathbf{AD} \otimes \mathbf{C}^T\mathbf{B})^{\overset{24}{T}}$$

$$(\mathbf{A} \otimes \mathbf{B})^{\overset{24}{T}}(\mathbf{C} \otimes \mathbf{D}) = (\mathbf{AC}^T\mathbf{B} \otimes \mathbf{D})$$

$$(\mathbf{A} \otimes \mathbf{B})(\mathbf{C} \otimes \mathbf{D})^{\overset{24}{T}} = (\mathbf{A} \otimes \mathbf{DB}^T\mathbf{C})$$

$$(\mathbf{A} \otimes \mathbf{B})^{\overset{24}{T}}\mathbf{C} = \mathbf{AC}^T\mathbf{B}$$

A.2   Tensor Analysis

Derivative of products of functions:

$$(\mathbf{a} \otimes \mathbf{b})' = \mathbf{a}' \otimes \mathbf{b} + \mathbf{a} \otimes \mathbf{b}' \quad \text{and} \quad (\mathbf{AB})' = \mathbf{A}'\mathbf{B} + \mathbf{AB}'$$

Selected derivatives of tensors and their invariants:

$$\frac{\partial \mathbf{A}}{\partial \mathbf{A}} = (\mathbf{I} \otimes \mathbf{I})^{\overset{23}{T}} = \overset{4}{\mathbf{I}} \qquad\qquad \frac{\partial \mathrm{tr}\,\mathbf{A}}{\partial \mathbf{A}} = \mathbf{I}$$

$$\frac{\partial \mathbf{A}^T}{\partial \mathbf{A}} = (\mathbf{I} \otimes \mathbf{I})^{\overset{24}{T}} \qquad\qquad \frac{\det \mathbf{A}}{\mathbf{A}} = \mathrm{cof}\,\mathbf{A} = (\det \mathbf{A})\mathbf{A}^{T-1}$$

$$\frac{\partial \mathbf{A}^{-1}}{\partial \mathbf{A}} = -(\mathbf{A}^{-1} \otimes \mathbf{A}^{-1})^{\overset{23}{T}} \qquad\qquad \frac{\partial \mathrm{cof}\,\mathbf{A}}{\partial \mathbf{A}} = \det\,[(\mathbf{A}^{T-1} \otimes \mathbf{A}^{T-1}) -$$

$$-(\mathbf{A}^{T-1} \otimes \mathbf{A}^{T-1})^{\overset{24}{T}}]$$

Selected rules related to the gradient and divergence operators:

$$\mathrm{grad}\,(\alpha\beta) = \alpha\,\mathrm{grad}\,\beta + \beta\,\mathrm{grad}\,\alpha \qquad \mathrm{div}\,(\mathbf{a} \otimes \mathbf{b}) = \mathbf{a}\,\mathrm{div}\,\mathbf{b} + (\mathrm{grad}\,\mathbf{a})\mathbf{b}$$

$$\mathrm{grad}\,(\alpha\mathbf{b}) = \mathbf{b} \otimes \mathrm{grad}\,\alpha + \alpha\,\mathrm{grad}\,\mathbf{b} \qquad \mathrm{div}\,(\alpha\mathbf{B}) = \mathbf{B}\,\mathrm{grad}\,\alpha + \alpha\,\mathrm{div}\,\mathbf{B}$$

$$\mathrm{grad}\,(\alpha\mathbf{B}) = \mathbf{B} \otimes \mathrm{grad}\,\alpha + \alpha\,\mathrm{grad}\,\mathbf{B} \qquad \mathrm{div}\,(\mathbf{A}\mathbf{b}) = (\mathrm{div}\,\mathbf{A}^T) \cdot b + \mathbf{A}^T \cdot \mathrm{grad}\,\mathbf{b}$$

$$\mathrm{div}\,(\alpha\mathbf{b}) = \mathbf{b} \cdot \mathrm{grad}\,\alpha + \alpha\,\mathrm{div}\,\mathbf{b} \qquad \mathrm{div}\,\left(\frac{\mathbf{b}}{\alpha}\right) = \frac{1}{\alpha}\mathrm{div}\,\mathbf{b} - \frac{1}{\alpha^2}\mathbf{b} \cdot \mathrm{grad}\,\alpha$$

Appendix B:
Solution of a Cubic Equation

In order to tackle the characteristic polynomial (4.44), the possible algorithms to solve a cubic equation are detailed here. The most famous general solution to this question refers to *Cardano*'s[1] method. In the first step, a cubic equation expressed as

$$ax^3 + bx^2 + cx + d = 0 \quad \text{with} \quad a \neq 0,$$

is regularised such that the coefficient of the third-order term is unit, as

$$x^3 + \bar{b}x^2 + \bar{c}x + \bar{d} = 0,$$

where $\bar{b} = b/a$, $\bar{c} = c/a$ and $\bar{d} = d/a$. The second step is to eliminate the second-order term by substituting x with $y - \bar{b}/3$. The corresponding equation is also called as a depressed cubic and written as,

$$y^3 + py + q = 0,$$

where the coefficients take the form of

$$p = \bar{c} - \frac{\bar{b}^2}{3} \quad \text{and} \quad q = \frac{2\bar{b}^3}{27} - \frac{\bar{b}\bar{c}}{3} + \bar{d}.$$

In the third step, the unknown y is assumed to be a sum of another two variables u and v, namely

$$y = u + v.$$

As the number of the unknowns is extended from one (only y) to two (u and v), another constraint can be added as

$$3uv + p = 0.$$

Inserting $y = u + v$ into the modified cubic equation yields

$$(u^3 + v^3 + q) + (u + v)(3uv + p) = 0.$$

As the constraint eliminates the second term, this equation is valid if

$$u^3 + v^3 + q = 0.$$

Set $U = u^3$ and $V = v^3$, this equation is transformed into

$$U + V + q = 0.$$

Recalling the constraint yields another relation between U and V as $UV = -\dfrac{p^3}{27}$. If neither U nor V is zero (this is guaranteed by $p \neq 0$), U can be computed via

$$U = -\frac{p^3}{27V}.$$

---

[1] *Gerolamo Cardano* (1501-1576): Italian polymath.

Substituting U in the equation $U + V + q = 0$ and multiplying this equation with V yields a quadratic function

$$V^2 + qV - \frac{p^3}{27} = 0.$$

This second-order equation has different sets of roots classified by the discriminant, which is defined as

$$\Delta = q^2 + \frac{4p^3}{27} = -\frac{(bc - 9ad)^2 - 4(b^2 - 3ac)(c^2 - 3bd)}{81a^4} = -\frac{B^2 - 4AC}{81a^4},$$

where $A = b^2 - 3ac$, $B = bc - 9ad$ and $C = c^2 - 3bd$. It is well known that regarding the value of Δ, different sets of roots will be derived. They are two identical real roots, two different real roots and two non-real roots that are complex conjugates. The solution of u and v can be obtained afterwards as cubic root of U and V. It should be noticed that in a complex space, there are three cube roots for a real number. For example, the cubic roots of 1 are 1, $\frac{-1+\sqrt{3}i}{2}$ and $\frac{-1-\sqrt{3}i}{2}$, respectively. Then the sum of u and v gives y and eventually the solution of x is found from y. Although the basic idea of Cardano's method is straightforward, its algebraic solution related to the complex space is complicated and lengthy. An elegant expression is derived if one recalls the Euler formula

$$e^{ix} = \cos x + i\sin x,$$

which relates the complex exponential function to the trigonometric functions. For the depressed cubic equation $y^3 + py + q = 0$, its corresponding roots can be written as

$$y_i = 2\sqrt{-\frac{p}{3}} \cos\left[\frac{1}{3}\arccos\left(\frac{3q}{2p}\sqrt{\frac{-3}{p}}\right) - \frac{2\pi i}{3}\right] \quad \text{for} \quad i = 0, 1, 2.$$

This expression is also known as *Viète's*[2] formula. However, this analytical solution encounters numerical difficulty when two or three of the cubic roots are identical or nearly identical, see Hartmann [107]. In order to avoid the instability induced by the multiple roots, one may refer to *Shengjin's*[3] formula, see Fan [85]. There are three sub-discriminants A, B and C, defined as

$$A = b^2 - 3ac, \quad B = bc - 9ad, \quad C = c^2 - 3bd$$

and the main discriminant is

$$\Delta_S = B^2 - 4AC.$$

For the case $A = B = 0$, the solutions are

$$x_1 = x_2 = x_3 = \frac{-b}{3a} = \frac{-c}{b} = \frac{-3d}{c} \quad \text{for} \quad b \neq 0, \, c \neq 0.$$

---

[2] *François Viète* (1540-1603): French mathematician

[3] *Shengjin Fan* (1955-2018): Chinese mathematician, who developed a new method to compute the cubic roots when he was a mathematics teacher at a high school. His method is adorable not only because of its simple expression but also due to the similar structure of the discriminant as the one of a quadratic equation.

For the case $\Delta_S = 0$, $A \neq 0$, $B \neq 0$, there are three real roots and two of them are identical,

$$x_1 = -\frac{b}{a} + \frac{B}{A}, \; x_2 = x_3 = -\frac{B}{2A}.$$

For the case $\Delta_S < 0$, there are three different real roots,

$$x_1 = \frac{-b - 2\sqrt{A}\cos\frac{\theta}{3}}{3a}, \; x_{2,3} = \frac{-b + \sqrt{A}(\cos\frac{\theta}{3} \pm \sqrt{\sin\frac{\theta}{3}})}{3a},$$

where

$$\theta = \arccos\frac{2Ab - 3aB}{2A\sqrt{A}}.$$

For the rest cases, there are always non-real roots and hence no more discussion is continued. Note that it is proven that for $\Delta_S < 0$, A must be greater than zero. Hence,

$$-1 < \frac{2Ab - 3aB}{2A\sqrt{A}} < 1$$

must hold and θ exists. The drawback of *Shengjin*'s formula is that it is only valid when all the coefficients of the cubic function are real numbers. Despite this, it provides a simple way to check whether there are multiple roots. The algorithm is given in Table B.1.

In addition to the aforementioned analytical solutions, it is also possible to compute the eigenvalues by iterative algorithms, to name but only a few, *Arnoldi* iteration, *Givens* rotations, and *Householder* transformations. The basic idea behind is to transform the target matrix to a diagonal matrix that has the same eigenvalues. As the strain tensor is a symmetric tensor and all the coefficients are real numbers, it is suitable to compute its eigenvalues by combing the *QL*-decomposition to a *Householder* transformation, cf. Markert [146]. The *Householder* transformation reflects an arbitrary matrix with a plane (or a hyper plane) containing the origin and reduces this matrix to a tridiagonal form. For a 3×3 symmetric matrix,

$$\mathbf{A} = \begin{bmatrix} a_{11} & a_{12} & a_{13} \\ a_{12} & a_{22} & a_{23} \\ a_{13} & a_{23} & a_{33} \end{bmatrix}$$

if $a_{13} = 0$, then A has already been a tridiagonal matrix. If $a_{13} \neq 0$, the corresponding tridiagonal matrix B after *Householder* transformation is

$$\mathbf{B} = \begin{bmatrix} a_{11} & l & 0 \\ l & a_{22} + vw & a_{23} - uw \\ 0 & a_{23} - uw & a_{33} - vw \end{bmatrix}$$

with $l = \sqrt{a_{12}^2 + a_{13}^2}$, $u = \frac{a_{12}}{l}$, $v = \frac{a_{13}}{l}$, $w = 2a_{23}u + (a_{33} - a_{22})v$ and the transformation matrix

$$\mathbf{Q}_H = \begin{bmatrix} 1 & 0 & 0 \\ 0 & u & v \\ 0 & v & -u \end{bmatrix}.$$

The matrices $\mathbf{A}$ and $\mathbf{B}$ are related to each other by $\mathbf{B} = \mathbf{Q}_H^T \, \mathbf{A} \, \mathbf{Q}_H$. After the tridiag-onalisation is accomplished, the *Givens* rotation is applied such that the derived matrix $\mathbf{B}$ is decomposed to an orthogonal matrix $\mathbf{Q}_G$ and a lower triangular matrix $\mathbf{L}$ such that $\mathbf{B} = \mathbf{Q}_G \mathbf{L}$. The diagonal entries of $\mathbf{L}$ are the eigenvalues of $\mathbf{A}$. For the details of the QL decomposition routine, one may refer to Press et al. [170].

Table B.1: *Algorithm for Shengjin's formula*

- $I_{\boldsymbol{\varepsilon}_S} = \mathbf{I} \cdot \boldsymbol{\varepsilon}_S$, $II_{\boldsymbol{\varepsilon}_S} = I_{\boldsymbol{\varepsilon}_S}^2 - \boldsymbol{\varepsilon}_S \cdot \boldsymbol{\varepsilon}_S$, $III_{\boldsymbol{\varepsilon}_S} = \det \boldsymbol{\varepsilon}_S$

- $a = -1$, $b = I_{\boldsymbol{\varepsilon}_S}$, $c = II_{\boldsymbol{\varepsilon}_S}$, $d = III_{\boldsymbol{\varepsilon}_S}$

- $A = b^2 - 3ac$, $B = bc - 9ad$, $C = c^2 - 3bd$

- IF $A = 0$ and $B = 0$,
$$\lambda_1 = \lambda_2 = \lambda_3 = -\frac{b}{3a},$$

  ELSE
$$\Delta_S = B^2 - 4AC$$

  IF $|\Delta_S| = 0$),
$$\lambda_1 = -\frac{b}{a} + \frac{B}{A}, \quad \lambda_2 = \lambda_3 = -\frac{B}{2A},$$

  ELSE
$$\theta = \arccos \frac{2Ab - 3aB}{2A\sqrt{A}}$$
$$\lambda_1 = \frac{-b - 2\sqrt{A}\cos\frac{\theta}{3}}{3a}, \quad \lambda_{2,3} = \frac{-b + \sqrt{A}(\cos\frac{\theta}{3} \pm \sqrt{\sin\frac{\theta}{3}})}{3a}.$$

  END
  END

Appendix C:
Applied Colour Scheme

No matter whether the importance of the colour scheme is realised in presenting the numerical results, the colour does influence the feeling of the observers about the output information of the figure. It should be emphasised that most default colour schemes are highly perceptually nonuniform, which results in the consequence that small changes in data values may lead to significant changes in the appearance or vice versa. Such nonlinearity makes the interpretation of the data more difficult and also may cause false boundaries. There is an example based on the most common colour scheme, cf. Figure C.1 (from https://bids.github.io/colormap/). Even without knowing the exact meaning
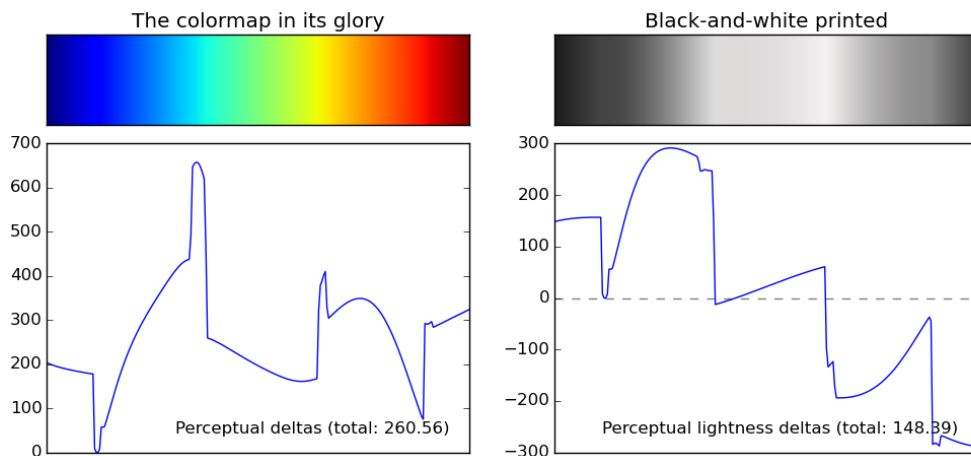

Figure C.1: *(top left) the colour scheme (top right) grayscale version (bottom left) perceptual deltas (bottom right) perceptual lightness deltas.*

of the perceptual deltas, one may observe that the colour scheme has two regions where the colour changes rapidly. One is between the blue and green while the other is between green and red. By plotting this colour scheme in black and white, it is easy to find two brighter narrow areas therein. When representing the colour with the RGB (red, green, blue), the Euclidean distance between two colours is defined by

$$d = \sqrt{(R_2 - R_1)^2 + (G_2 - G_1)^2 + (B_2 - B_1)^2}. \qquad (C.1)$$

In order to produce a uniformly distributed colour scheme, the most straightforward way is to choose two colours and interpolate a linear space between them. This approach guarantees a constant gradient in the corresponding colour scheme.

People also find that colour might change the appearance of the object. For example, a ball in white looks bigger than another of the same size but in black. Besides, colour also transmits emotion. It is commonly accepted that warm colours like red and orange, evoke

emotions while cool colours like blue recall calm. In order to provide the readers with a neutral feeling when reading this dissertation, the author has chosen the colours and the corresponding colour schemes inspired by *Giorgio Morandi* [1], which mainly comes from Figure C.2.

Figure C.2: *Painting by Giorgio Morandi.*

---

[1] *Giorgio Morandi*: (1890-1964) an Italian painter and printmaker who specialised in still life.

Bibliography

[1] Acartürk, A.: *Simulation of Changed Hydrated Porous Media.* Dissertation, Report No. II-18, Institute of Applied Mechanics (CE), University of Stuttgart 2009.

[2] Adachi, J.; Siebrits, E. & Desroches J.: Computer simulation of hydraulic fractures. *International Journal of Rock Mechanics and Mining Sciences* **44** (2007), 739-757.

[3] Aldakheel, F.: *Mechanics of Nonlocal Dissipative Solids: Gradient Plasticity and Phase Field Modeling of Ductile Fracture.* Dissertation, Report No. I-34, Institute of Applied Mechanics (CE), University of Stuttgart 2016.

[4] Ambati, M.; Gerasimov, T. & De Lorenzis, L.: A review on phase-field of brittle fracture and a new fast hybrid formulation. *Computational Mechanics* **55** (2015), 383-405.

[5] Ambati, M.; Gerasimov, T. & De Lorenzis, L.: Phase-field modeling of ductile fracture. *Computational Mechanics* **55** (2015), 1017-1040.

[6] Ambrosio, L. & Tortorelli, V. M.: Approximation of functionals depending on jumps by elliptic functionals via Γ-convergence. *Communications on Pure and Applied Mathematics* **43** (1990), 999-1036.

[7] Ambrosio, L; Fusco, N. & Pallara, D: *Functions of Bounded Variation and Free Discontinuity Problems.* Oxford University Press, New York 2000.

[8] Ammann, M.: *Parallel Finite Element Simulations of Localization Phenomena in Porous Media.* Dissertation, Report No. II-11, Institute of Applied Mechanics (CE), University of Stuttgart 2005.

[9] Amor, H.; Marigo, J.-J. & Maurini, C.: Regularized formulation of the variational brittle fracture with unilateral contact: Numerical experiments. *Journal of the Mechanics and Physics of Solids* **57** (2009), 1209-1229.

[10] Anderson, T. L.: *Fracture Mechanics: Fundamentals and Applications.* CRC Press, 2017.

[11] Aranson, I. S.;Kalatsky, V. A. & Vinokur, V. M. : Continuum field description of crack propagation. *Physical Review Letters* **85(1)** (2000), 118.

[12] Armero, F. & Linder, C.: Numerical simulation of dynamic fracture using finite elements with embedded discontinuities. *International Journal of Fracture* **160** (2009), 119141.

[13] Avci, O.: *Coupled Deformation and Flow Processes of Partial Saturated Soil: Experiments, Model Validation and Numerical Investigations.* Dissertation, Report No. II-26, Institute of Applied Mechanics (CE), University of Stuttgart 2013.

[14] Barenblatt, G. I.: The mathematical theory of equilibrium cracks in brittle fracture. *Advances in Applied Mechanics* **7** (1962), 55-129.

[15] Bathe, K. J.: *Finite-Element- Methoden.* Springer-Verlag, Berlin 1990.

[16] Batra, R. C. & Jin, X. S.: Analysis of dynamic shear bands in porous thermally softening viscoplastic materials. *Archives of Mechanics* **46** (1994), 1336.

[17] Bažant, Z. P.; Salviato, M.; Chau, V. T.; Viswanathan H. & Zubelewicz, A.: Why fracking works. *Journal of Applied Mechanics* **81** (2014), 101010.

[18] Beavers, G. S. & Joseph, D. D.: Boundary conditions at a natural permeable wall. *Journal of Fluid Mechanics* **30** (1967), 197-207.

[19] Belytschko, T. & Black, T.: Elastic crack growth in finite elements with minimal remeshing. *International Journal for Numerical Methods in Engineering* **45** (1999), 601-620.

[20] Belytschko, T.; Chen, H.; Xu, J. & Zi, G.: Dynamic crack propagation based on loss of hyperbolicity and a new discontinuous enrichment. *International Journal for Numerical Methods in Engineering* **58** (2003), 18731905.

[21] Biot, M. A.: General theory of three dimensional consolidation. *Journal of Applied Physics* **12** (1941), 155–164.

[22] Biot, M. A.: Theory of propagation of elastic waves in a fluid-saturated porous solid, I. Low frequency range,. *Journal of Acoustical Society of America* **28** (1956), 168–178.

[23] Biot, M. A.: Theory of propagation of elastic waves in a fluid-saturated porous solid, I. Higher frequency range,. *Journal of Acoustical Society of America* **28** (1956), 179-191.

[24] Blanton T. L.: An experimental study of interaction between hydraulically induced and pre-existing fractures. In SPE Unconventional Gas Recovery Symposium, *Society of Petroleum Engineering* (1982), document ID SPE-10847-MS.

[25] de Boer, R.: *Vektor- und Tensorrechnung für Ingenieure.* Springer-Verlag, Berlin 1982.

[26] de Boer, R. & Ehlers, W.: Theorie der Mehrkomponentenkontinua mit Anwendungen auf bodenmechanische Probleme. Forschungsberichte aus dem Fachbereich Bauwesen, Heft 40, Universität-GH-Essen 1986.

[27] de Boer, R. & Ehlers, W.: The development of the concept of effective stresses. *Acta Mechanica* **83** (1990), 77-92.

[28] de Boer, R.: Highlights in the historical development o f the porous media theory: Toward a consistent macroscopic theory. *Applied Mechanics Reviews* **49** (1996), 201-262.

[29] de Boer, R.: *Theory of Porous Media: Highlights in Historical Development and Current State.* Springer-Verlag, Berlin, 2000.

[30] Bohloli, B. & de Pater, C.: Experimental study on hydraulic fracturing of soft rocks: Influence of fluid rheology and confining stress. *Journal of Petroleum Science and Engineering* **53** (2006), 1-12.

[31] Boone, T. J. & Ingraffea, A. R.: A numerical procedure for simulation of hydraulically-driven fracture propagation in poroelastic media. *International Journal of Numerical and Analytical Methods in Geomechanics* **14** (1990), 27-47.

[32] Boone, T. J. & Detournay, E.:Response of a vertical hydraulic fracture intersecting a poroelastic formation bounded by semi-infinite impermeable elastic layers. *International Journal of Rock Mechanics and Mining Sciences & Geomechanics Abstracts* **27** (1990), 189-197.

[33] Borden, M. J.; Verhoosel, C. V.; Scott, M. A.; Hughes, T. J. R. & Landis C. M.: A phase-field description of dynamic brittle fracture. *Computer Methods in Applied Mechanics and Engineering* **217** (2012), 77-95.

[34] Bourdin, B.; Francfort, G. A. & Marigo, J.-J.: Numerical experiments in revisited brittle fracture. *Journal of the Mechanics and Physics of Solids* **48** (2000), 797-826.

[35] Bourdin, B.: Numerical implementation of the variational formulation for quasi-static brittle fracture. *Interfaces and Free Boundaries* **9** (2007), 411-430.

[36] Bourdin, B.; Francfort, G. A. & Marigo, J.-J.: Special invited exposition: The variational approach to fracture. *Journal of Elasticity* **91** (2008), 5-148.

[37] Bourdin, B; Larsen, C. & Richardson, C. L: A time-discrete model for dynamic fracture based on crack regularization. *International Journal of Fracture* **168** (2011), 133-143.

[38] Bourdin, B.; Chukwudozie, C. P. & Yoshioka, K.: A variational approach to the numerical simulation of hydraulic fracturing, in: SPE Annual Technical Conference and Exhibition. *Society of Petroleum Engineers*, 2012.

[39] Bowen, R. M. & Wiese, J. C.: Diffusion in Mixtures of elastic material. *International Journal of Engineering Science* **7** (1969), 689-722.

[40] Bowen, R. M.: Theory of mixtures, in: Eringen, A.C.(Ed.). *Continuum Physics*, Vol. III. Academic Press, New York 1976, pp. 1-127.

[41] Bowen, R. M.: Incompressible porous media models by use of the theory of mixtures. *International Journal of Engineering Science* **18** (1980), 1129-1148.

[42] Bowen, R. M.: Compressible porous media models by use of the theory of mixtures. *International Journal of Engineering Science* **20** (1982), 697-735.

[43] Braides, D. P.: *Approximation of Free Discontinuity Problems.* Springer-Verlag, Berlin 1998.

[44] Braides, D. P.: Γ-*Convergence for beginners.* Oxford University Press, New York 1999.

[45] Braess. D.: *Finite elements: Theory, fast solvers, and application in solid mechanics.* Springer-Verlag, Berlin 1997.

[46] Buliga, M.: Energy minimizing brittle crack propagation. *Journal of Elasticity* **52** (1999), 201-238.

[47] Camacho, G. T. & Ortiz, M.: Computational modelling of impact damage in brittle materials. *International Journal of Solids and Structures* **33** (1996), 28992938.

[48] Capriz, G.: *Continua with Microstructure.* Springer, 1989.

[49] Chadwick, P.: *Continuum Mechanics: Concise Theory and Problems.* Dover Publications, Mineola (NY) 1999.

[50] Cosserat, E. & Cosserat, F.: Sur la mécanique générale. *Comptes Rendus de l'Académie des Sciences* **145** (1907), 1139-1142.

[51] Cosserat, E. & Cosserat, F.: *Théorie des Corps Déformables.* A. Hermann & Fils, Paris (1909).

[52] Cottrell, A. H.: *Tewksbury Symposium on Fracture.* University of Melbourne, 1963.

[53] Dal Maso, G: *An Introduction to* Γ-*convergence.* Birkhäuser, Boston 1993.

[54] Dal Maso, G. & Toader, R.: quasi-statice and approximation results. *Archive for Rational Mechanics and Analysis* **163** (2002), 101-135.

[55] Detournay, E.: Propagation regimes of fluid-driven fractures in impermeable rocks. *International Journal of Geomechanics* **4** (2004), 35-45.

[56] Diebels, S. & Ehlers, W.: Dynamic analysis of a fully saturated porous medium accounting for geometrical and material non-linearities. *International Journal for Numerical Methods in Engineering* **39** (1996), 81-97.

[57] Diebels, S. & Ehlers, W.: On fundamental concepts of multiphase micropolar materials. *Technische Mechanik* **16** (1996), 77-88.

[58] Diebels, S.: *Mikropolare Zweiphasenmodelle: Formulierung auf der Basis der Theorie Poröser Medien.* Habilitation, Bericht Nr. II-4 aus dem Institut für Mechanik (Bauwesen), Universität Stuttgart 2000.

[59] Dugdale, D.: Yielding of steel sheets containing slits. *Journal of the Mechanics and Physics of Solids* **8** (1960), 100-104.

[60] Eastgate, L. O.; Sethna, J. P.; Rauscher, M. & Cretegny, T.: Fracture in mode I using a conserved phase-field model. *Physical Review E* **65** (2002), 036117.

[61] Ehlers, W.: On thermodynamics of elasto-plastic porous media. *Archives of Mechanics* **41** (1989), 73-93.

[62] Ehlers, W.: Constitutive equations for granular materials in geomechanical context, in: Hutter, K.(Ed.).:*Continuum Mechanics in Environmental Sciences and Geophysics*, CISM Courses and Lectures No. 337. Springer-Verlag, Wien 1993, pp. 313-402.

[63] Ehlers, W.: Grundlegende Konzepte in der Theorie Poröser Medien. *Technische Mechanik* **16** (1996), 63-76.

[64] Ehlers, W. & Volk, W.: On shear band localization phenomena of liquid-saturated granular elasto-plastic porous solid materials accounting for fluid viscosity and micropolar solid rotations. *Mechanics of Cohesive-frictional Materials* **2** (1997), 301-320.

[65] Ehlers, W. & Volk, W.: On theoretical and numerical methods in the Theory of Porous Media based on polar and non-polar elasto-plastic solid materials. *International Journal of Solid and Structures* **35** (1998), 4597-4617.

[66] Ehlers, W.; Ellsiepen, P.; Blome, P.; Mahnkopf, D. & Markert, B.: *Theoretische und numerische Studien zur Lösung von Rand- und Anfangswertproblemen in der Theorie Poröser Medien.* Abschlußbericht zum DFG-Forschungsvorhaben Eh 107/6-2, Bericht aus dem Institut für Mechanik (Bauwesen), Nr. 99-II-1, Universität Stuttgart, 1999.

[67] Ehlers, W. & Markert, B.: A linear viscoelastic biphasic model for soft tissues based on the Theory of Porous Media. *Journal of Biomechanical Engineering* **123** (2001), 418-424.

[68] Ehlers, W.: Foundations of multiphasic and porous materials. In Ehlers, W. & Bluhm. J. (Eds.): *Porous Media: Theory, Experiments and Numerical Applications.* Springer-Verlag, Berlin 2002, pp. 3-86.

[69] Ehlers, W.; Graf, T. & Ammann, M.: Deformation and localization analysis of partially saturated soil. *Computer Methods in Applied Mechanics and Engineering* **193** (2004), 2885-2910.

[70] Ehlers, W.: *Poröse Medien - ein kontinuumsmechanishes Modell auf der Basis der Mischungstheorie* . Institute of Applied Mechanics (Civil Engineering), University of Stuttgart 2012, Nachdruck der Habilitationsschrift aus dem Jahre 1989 (Forschungsbericht aus dem Fachbereich Bauwesen der Universität-GH-Eseen, 47, Essen 1989).

[71] Ehlers, W.; Zinatbakhsh, S. & Markert. B.: Stability analysis of finite difference scheme revisited: A study of decoupled solution strategies for coupled multifield

problems. *International Journal of Numerical Methods in Engineering* **94** (2013), 758-786.

[72] Ehlers, W.: Porous media in the light of history, in: Stein, E. (Ed.), The History of Theoretical, Material and Computational Mechanics - Mathematics Meets Mechanics and Engineering, in: *Lecture Notes in Applied Mathematics and Mechanics*, vol. 1 Springer, Heidelberg, 2014, pp. 211-227.

[73] Ehlers, W. & Luo, C.: A phase-field approach embedded in the theory of porous media for the description of dynamic hydraulic fracturing. *Computer Methods in Applied Mechanics and Engineering* **315** (2017), 348-368.

[74] Ehlers, W. & Luo, C.: A phase-field approach embedded in the Theory of Porous Media for the description of dynamic hydraulic fracturing,Part II: The crack-opening indicator. *Computer Methods in Applied Mechanics and Engineering* **341** (2018), 429-442.

[75] Ehlers, W.: Effective stresses in multiphasic porous media: A thermodynamic investigation of a fully non-linear model with compressible and incompressible constituents. *Geomechanics for Energy and the Environment* **15** (2018), 35-46.

[76] Ehlers, W.: *Vector and Tensor Calculus: An Introduction.* Lecture Notes, Institute of Applied Mechanics (CE), University of Stuttgart 1995-2018, URL http://www.mechbau.uni-stuttgart.de/ls2/Downloads/Downloads.html.

[77] Eipper, G.: *Theorie und Numerik finiter elastischer Deformationen in fluidgesättigten porösen Festkörpern.* Dissertation, Bericht Nr. II-1, Institut für Mechanik (Bauwesen), Universität Stuttgart 1998.

[78] Ellsiepen, P.: *Zeit- und orsadaptive Verfahren angewandt auf Mehrphasenprobleme poröser Medien.* Dissertation Bericht Nr. II-3 aus dem Institut für Mechanik (Bauwesen), Universität Stuttgart 1999.

[79] Eringen, A. C. & Ingram, J. D.: A continuum theory of chemically reacting media. *International Journal of Engineering Science* **3** (1965), 197-212.

[80] Eriksson, K.: Decomposition of Eshelby's energy momentum tensor and application to path and domain independent integrals for the crack extension force of a plane circular crack in Mode III loading. *International Journal of Fracture* **144** (2007), 215-255.

[81] Eshelby, J. D.: The force on an elastic singularity. *Philosophical Transactions of the Royal Society London A* **244** (1951), 87-112.

[82] Eshelby, J. D.: The elastic energy-momentum tensor. *Journal of Elasticity* **5** (1975), 321-335.

[83] Eshelby, J. D.: Energy relations and the energy-momentum tensor in continuum mechanics. In Ball, J.M.; Kinderlehrer, D; Podio-Guidugli, P & Slemrod M. (Ed.) :*Fundamental Contributions to the Continuum Theory of Evolving Phase Interfaces in Solids*. Springer, Berlin 1999, pp. 82-119.

[84] Fagerström, M.; Larsson, R.: Theory and numerics for finite deformation fracture modelling using strong discontinuities. *International Journal for Numerical Methods in Engineering* **66** (2006), 911948.

[85] Fan, S: A new extracting formula and a new distinguishing means on the one variable cubic equation. *Natural Science Journal of Hainan Teachers College* **2.2** (1989), 91-98.

[86] Felippa, C. A. & Park K. C.: Synthesis tools for structural dynamics and partitioned analysis of coupled system. In Ibrahimbegovic, A. & Brank, B. (eds): *Engineering Structures Under Extreme Conditions: Multi-Physics and Multi-Scale Computer Models in Non-Linear Analysis and Optimal Design.* IOS Press, Amsterdam 2005, pp. 50-110.

[87] Fosdick, R. & Truskinovsky, L.: About Clapeyron's theorem in linear elasticity. *Journal of Elasticity* **72** (2003), 145-172.

[88] Francfort, G. A. & Marigo J.-J.: Revisiting brittle fracture as an energy minimization problem. *Journal of the Mechanics and Physics of Solids* **46** (1998), 1319-1342.

[89] Frémond, M. & Nedjar, B.: Damage, gradient of damage, and principle of virtual power. *International Journal of Solids and Structures* **33** (1996), 10831103.

[90] Frémond, M.: *Non-Smooth Thermomechanics*. Springer, 2002.

[91] Freund, L. B.: *Dynamic Fracture Mechanics*. Cambridge University Press, 1998.

[92] Gasser, T. C. & Holzapfel, G. A.: Geometrically non-linear and consistently linearized embedded strong discontinuity models for 3D problems with an application to the dissection analysis of soft biological tissues. *Computer Methods in Applied Mechanics and Engineering* **192** (2003), 5059-5098.

[93] Geissler, G.; Netzker, C. & Kaliske, M.: Discrete crack path prediction by an adaptive cohesive crack model. *Engineering Fracture Mechanics* **77** (2010), 3541-3557.

[94] Graf, T.: *Multiphasic Flow Processes in Deformable Porous Media under Consideration of Fluid Phase Transitions.* Dissertation, Report No. II-17, Institute of Applied Mechanics (CE), University of Stuttgart 2008.

[95] Green, A. E. & Naghdi, P. M.: A dynamical theory of interacting continua. *International Journal of Engineering Science* **3** (1965), 231-241.

[96] Griffith, A. A.: The phenomena of rupture and flow in solids. *Philosophical transactions of the Royal Society of London A* **221** (1921), 163-198.

[97] Griffith, A. A.: The Theory of Rupture. In Biezeno, C.B. & Burgers, J.M. (Ed.): *Proceedings of the First International Congress for Applied Mechanics.* Delft 1924, pp. 55-63.

[98] Gross, D. & Seelig, T.: Bruchmechanik. Springer-Verlag, Berlin 1996.

[99] Gross, D. & Seelig, T.: *Fracture Mechanics with an Introduction to Micromechanics.* 2nd Ed., Springer-Verlag, Berlin, 2011.

[100] Gürses, E.: *Aspects of Energy Minimization in Solid Mechanics: Evolution of Inelastic Microstructures and Crack Propagation.* Dissertation, Bericht Nr. I-19 aus dem Institut für Mechanik (Bauwesen), Universität Stuttgart 2007.

[101] Gürses, E. & Miehe, C.: A computational framework of three dimensional configurational force driven brittle crack propagation. *Computer Methods in Applied Mechanics and Engineering* **198** (2009), 14131428.

[102] Gurtin, M. E.: *An Introduction to Continuum Mechanics.* Academic Press, Boston 1981.

[103] Gurtin, M. E.: Generalized Ginzburg-Landau and Cahn-Hilliard equations based on a microforce balance. *Physica* **D 92** (1996), 178-192.

[104] Häberle, K.: *Fluid-Phase Transitions in a Multiphasic Model of CO_2 Sequestration into Deep Aquifers: A Fully Coupled Analysis of Transport Phenomena and Solid Deformation.* Dissertation, Report No. II-34, Institute of Applied Mechanics (CE), University of Stuttgart 2017.

[105] Hahn, H. G.: Bruchmechanik. B.G. Teugner, Stuttgart 1976.

[106] Hakim, V. & Karma, A.: Laws of crack motion and phase-field models of fracture. *Journal of the Mechanics and Physics of Solids* **57** (2009), 342-368.

[107] Hartmann, S.: Computational aspects of the symmetric eigenvalue problems of second order tensors. *Technische Mechanik* **23** (2003), 283-294.

[108] Hassanizadeh, S. M. & Gray, W. G.: General conservation equations for multi-phase systems: 1. Averaging procedure. *Advances in Water Resources* **2** (1979), 131-144.

[109] Hattori, G.; Trevelyan, J.; Augarde, C. E.; Coombs, W. M. & Aplin, A. C.: Numerical simulation of fracking in shale rocks: current state and future approaches. *Archives of Computational Methods in Engineering* (2016), 1-37.

[110] Haupt, P.: Foundation of continuum mechanics. In Hutter, K. (Ed.): *Continuum Mechanics in Environmental Sciences and Geophysics.* Springer-Verlag, Wien 1993, CISM Courses and Lectures No. 337, pp. 1-77.

[111] Haupt, P.: *Continuum Mechanics and Theory of Materials.* 2nd Ed., Springer-Verlag, Berlin 2002.

[112] Heider, Y.: *Saturated Porous Media Dynamics with Application to Earthquake Engineering.* Dissertation, Report No. II-25, Institute of Applied Mechanics (CE), University of Stuttgart 2012.

[113] Heider, Y. & Markert, B.: A phase-field modeling approach of hydraulic fracture in saturated porous media. *Mechanics Research Communications* **80** (2017), 38-46.

[114] Henry, H & Levine, H: Dynamic instabilities of fracture under biaxial strain using a phase field model. *Physical review letters* **93(10)** (2004), 105504.

[115] Hofacker, M.: *A Thermodynamically Consistent Phase Field Approach to Fracture.* Dissertation, Report No.I-29, Institute of Applied mechanics (CE), University of Stuttgart 2014.

[116] Huber, O.; Nickel, J. & Kuhn, G.: On the decomposition of the J-integral for 3D crack problems. *International Journal of Fracture* **64** (1993), 339-348.

[117] Hughes, T. J. R.: *The Finite Element Method: Linear Static and Dynamic Finite Element Analysis.* Dover Publications, New York 2012.

[118] Inglis, C. E.: Stresses in a plate due to the presence of cracks and sharp corners. *Transactions of the Royal Institution of Naval Architects* **55** (1913), 219-230.

[119] Irwin, G. R.: Analysis of stresses and strains near the end of a crack traversing a plate. *Journal of Applied Mechanics* **24** (1957), 361-364.

[120] Irwin, G. R.: Fracture. In Flügge, S. (Ed.): *Encyclopedia of Physics*, **6**. Elasticity and Plasticity, Springer, 1958, pp. 551-590.

[121] Irwin, G. R.; Kies, J. A. & Smith, H. L.: Fracture strength relative to the onset and arrest of crack propagation. *Proc ASTM* **58** (1958), 640-657.

[122] Jirásek, M.: Nonlocal theories in continuum mechanics. *Acta Polytechnica* **44** (2004), 16-34.

[123] Kachanov, L. M.: Rupture times under creep conditions. *International Journal of Fracture* **97** (1958), 26-31.

[124] Kachanov, L. M.: *Introduction to Continuum Damage Mechanics.* Maritinus Nijhoff Publishers, 1986.

[125] Kaliske, M.; Dal, H.; Fleischhauer, R.; Jenkel, C. & Netzker, C.:Characterization of fracture processes by continuum and discrete modelling. *Computational Mechanics* **50** (2012), 303320.

[126] Kalthoff, J. F. & Winkler, S.: *Impact Loading and Dynamic Behaviour of Materials*, Chapter Failure mode transition at high rates of shear loading. DGM Informationsgesellschaft 1987, pp. 185-195.

[127] Kalthoff, J. F.: Modes of dynamic shear failure in solids. *International Journal of Fracture* **101** (2000), 1-31.

[128] Kanninen, M. F. & Popelar, C. H.: *Advanced Fracture Mechanics.* Oxford University Press, New York 1985.

[129] Karajan, N.: *An Extended Biphasic Description of the Inhomogeneous and Anisotropic Intervertebral Disc.* Dissertation, Report No. II-19, Institute of Applied Mechanics (CE), University of Stuttgart 2009.

[130] Karajan, N.: Multiphasic intervertebral disc mechanics: Theory and application. *Archives of Computational Methods in Engineering* **19** (2012), 261-339.

[131] Karma, A.; Kessler, D. A. & Levine, H.: Phase-field model of mode III dynamic fracture. *Physical Review Letters* **87** (2001), 045501/1-045501/4.

[132] Koch, D.: *Thermomechanical modelling of non-isothermal porous materials with application to enhanced geothermal systems.* Dissertation, Report No. II-31, Institute of Applied Mechanics (CE), University of Stuttgart 2016.

[133] Krafft, J. M.; Sullivan, A & Boyle, R.: Effect of dimensions on fast fracture instability of notched sheets. *Proceedings of the Crack-Propagation Symposium* **1** (1961), 8-28.

[134] Krause, R. F.: *Growth, Modelling and Remodelling of Biological Tissue.* Dissertation, Report No. II-29, Institute of Applied Mechanics (CE), University of Stuttgart 2014.

[135] Kuhn, C. & Müller, R.: A continuum phase field model for fracture. *Engineering Fracture Mechanics* **77** (2010), 3625-3634.

[136] Kuhn, C. & Müller, R.: A new finite element technique for a phase field model of brittle fracture. *Journal of Theoretical and Applied Mechanics* **49** (2011), 4: 1115-1133.

[137] Lemaitre, J.: *A Course on Damage Mechanics.* Springer-Verlage, Berlin, 1996.

[138] Lambrecht, M.: *Theorie und Numerik von Materialinstabilitäten elastoplastischer Festkörper auf der Grundlage inkrementeller Variationsformulierungen.* Dissertation, Bericht Nr. I-8 aus dem Institut für Mechanik (Bauwesen), Universität Stuttgart 2002.

[139] Li, S.; Liu, W. K.; Rosakis, A. J.; Belytschko, T. & Hao, W.: Mesh-free Galerkin simulations of dynamic shear band propagation and failure mode transition. *International Journal of Solids and Structures* **39** (2002), 12131240.

[140] Linder, C. & Armero, F.: Finite elements with embedded branching. *Finite Elements in Analysis and Design* **45** (2009), 280293.

[141] Luo, C. & Ehlers, W.: Hydraulic fracturing based on the Theory of Porous Media. *PAMM* **15** (2015), 401-402.

[142] Luo, C. & Ehlers, W.: A three-dimensional model of hydraulic fracturing. *PAMM* **16** (2016), 465-466.

[143] Mabuma, J.: *Multi-Field Modelling and Simulation of the Human Hip Joint.* Dissertation, Report No. II-28, Institute of Applied Mechanics (CE), University of Stuttgart 2014.

[144] Malvern, L. E.: *Introduction to the Mechanics of a Continuous Medium.* Prentice-Hall, Englewood Cliffs (NJ) 1969.

[145] Mariano, P. M.: Multifield theories in mechanics of solids. *Advances in Applied Mechanics* **38** (2001), 193.

[146] Markert, B.: *Porous media viscoelasticity with application to polymeric foams.* Dissertation, Report No. II-12, Institute of Applied Mechanics (CE), University of Stuttgart 2005.

[147] Markert, B.; Heider, Y. & Ehlers, W.: Comparison of monolithic and splitting solution schemes for dynamic porous media problems. *International Journal for Numerical Methods in Engineering* **82** (2010), 1341-1383.

[148] Markert, B. & Heider, Y.: Coupled multi-field continuum methods for porous media fracture, in: Mehl, M., Bischoff, M. & Schäfer, M.(Eds.), Recent Trends in Computational Engineering - CE2014. *Lecture Notes in Computational Science and Engineering* **105** (2015), 167–180.

[149] Marsden, J. E. & Hughes, T. J. R.: *Mathematical Foundations of Elasticity.* Dover Publications, New York 1983.

[150] Maugin, G. A. & Trimarco, C.: Pseudomomentum and material forces in nonlinear elasticity: Variational formulations and application to brittle fracture. *Acta Mechanica* **94** (1992), 1-28.

[151] Maugin, G. A.: *The Thermomechanics of Plasticity and Fracture.* Cambridge University Press, Cambridge 1992.

[152] Middleton, R.; Viswanathan, H.; Currier, R. & Gupta, R.: CO2 as a fracturing fluid: Potential for commercial scale shale gas production and CO2 sequestration. *Energy Procedia* **63** (2014), 7780-7784.

[153] Miehe, C. & Lambrecht, M.: Algorithms for computation of stresses and elasticity moduli in terms of Seth-Hills family of generalized strain tensors. *Communications in Numerical Methods in Engineering* **17** (2001), 337-353.

[154] Miehe, C. & Gürses, E.: A robust algorithm for configurational-force-driven brittle crack propagation with R-adaptive mesh alignment. *International Journal for Numerical Methods in Engineering* **72** (2007), 127-155.

[155] Miehe C.; Hofacker M. & Welschinger F.: A phase field model for rate-independent crack propagation: Robust algorithmic implementation based on operator splits. *Computer Methods in Applied Mechanics and Engineering* **199** (2010), 2765-2778.

[156] Miehe, C.; Welschinger, F. & Hofacker M.: Thermodynamically consistent phase-field models of fractures: Variational principles and multi-field FE implementations. *International Journal of Numerical Methods in Engineering* **83** (2010), 1273-1311.

[157] Miehe, C.; Mauthe, S. & Teichtmeister, S.: Minimization principles for the coupled problem of Darcy-Biot-type fluid transport in porous media linked to phase field modeling of fracture. *Journal of the Mechanics and Physics of Solids* **82** (2015), 186-217.

[158] Miehe, C. & Mauthe, S.: Phase field modeling of fracture in multi-physics problems. Part III. Crack driving forces in hydro-poro-elasticity and hydraulic fracturing of fluid-saturated porous media. *Computer Methods in Applied Mechanics and Engineering* **304** (2016), 619–655.

[159] Mikelić, A.; Wheeler, M. F. & Wick, T.: A quasi-static phase-field approach to pressurized fractures. *Nonlinearity* **28** (2015), 1371.

[160] Mikelić, A.; Wheeler, M. F. & Wick, T.: A phase-field method for propagating fluid-filled fractures coupled to a surrounding porous medium. *Multiscale Modeling & Simulation* **13** (2015), 367–398.

[161] Moës, N.; Dolbow, J. & Belytschko, T.: A finite element method for crack growth without remeshing. *International Journal of Numerical Methods in Engineering* **46** (1999), 131-150.

[162] Moës, N. & Belytschko, T.: Extended finite element method for cohesive crack growth. *Engineering Fracture Mechanics* **69** (2002), 813-833.

[163] Mumford, D. & Shah, J.: Optimal approximations by piecewise smooth functions and associated variational problems. *Communications on Pure and Applied Mathematics* **42** (1989), 577-685.

[164] Needleman, A. & Tvergaard, V.: An analysis of dynamic, ductile crack growth in a double edge cracked specimen. *International Journal of Fracture* **49** (1991), 4167.

[165] Noll, W.: On the continuity of the fluid and solid states. *Journal of Rational Mechanics and Analysis* **4** (1955), 3-81.

[166] Noll, W.: A mathematical theory of the mechanical behavior of continuous media. *Archive for Rational Mechanics and Analysis* **2** (1958), 197-226.

[167] Oliver, J.; Huespe, A. E.; Samaniego, E. & Chaves, E. W. V.: On strategies for tracking strong discontinuities in computational failure mechanics. In *Proceedings of the Fifth World Congress on computational Mechanics (WCCM V)*. 2002, ISBN 3-9501554-0-6.

[168] Oliver, J.; Huespe, A. E.; Samaniego, E. & Chaves, E. W. V.: Continuum approach to the numerical simulation of material failure in concrete. *International Journal for Numerical and Analytical Methods in Geomechanics* **28** (2004), 609-632.

[169] Pandolfi, A. & Ortiz, M.: An efficient adaptive procedure for three-dimensional fragmentation simulations. *Engineering with Computers* **18** (2002), 148159.

[170] Press, W. H.; Teukolsky, S. A.; Vetterling, W. T. & Flannery, B. P.: *Numerical Recipes in C.* Cambridge University Press 1999, 2nd Ed., corrected reprint of 1992.

[171] Ramulu, M. & Kobayashi, A: Mechanics of crack curving and branching - a dynamic fracture analysis. *International Journal of Fracture Mechanics* **27** (1985), 187-201.

[172] Ravi-Chandar, K. & Knauss, W.: An experimental investigation into dynamic fracture: I. Crack initiation and arrest. *International Journal of Fracture* **25** (1984), 247-262.

[173] Ravi-Chandar, K. & Knauss, W.: An experimental investigation into dynamic fracture: II. Microstructral aspects. *International Journal of Fracture* **26** (1984), 65-80.

[174] Ravi-Chandar, K. & Knauss, W.: An experimental investigation into dynamic fracture: III. On steady-state crack propagation and crack branching. *International Journal of Fracture* **26** (1984), 141-154.

[175] Ravi-Chandar, K. & Knauss, W.: An experimental investigation into dynamic fracture: IV. On the interaction of stress waves with propagation cracks. *International Journal of Fracture* **26** (1984), 189-200.

[176] Ravi-Chandar, K.: On the failure mode transition in polycarbonate dynamic mixed-mode loading. *International Journal of Solids and Structures* **32** (1995), 925-938.

[177] Rempler, H.-U.; Wieners, C. & Ehlers, W.: Efficiency comparison of an augmented finite element formulation with standard return mapping algorithms for elastic-inelastic materials. *Computational Mechanics* **48** (2011), 551-562.

[178] Rempler, H.-U.: *Damage in Multi-Phasic Materials Computed with the Extended Finite-Element Method.* Dissertation, Report No. II-23, Institute of Applied Mechanics (CE), University of Stuttgart 2012.

[179] Rice, J. R.: A path independent integral and the approximate analysis of strain concentration by notches and cracks. *Journal of Applied Mechanics* **35** (1968), 379386.

[180] Rice, J. R. & Cleary, M. P.: Some basic stress diffusion solutions for fluid-saturated elastic porous media with compressible constituents. *Review of Geophysics and Space Physics* **14** (1976), 227-241.

[181] Rooke, D. P. & Cartwright, D. J.: *Compendium of stress intensity factors.* H.M.S.O. 1976.

[182] Rubin, M.: Experimental study of hydraulic fracturing in an impermeable material. *Journal of Energy Resources Technology* **105** (1983), 116-124.

[183] Salje, E. K; Soto-Parra, D. E.; Planes, A.; Vives, E.; Reinecker, M. & Schranz, W.: Failure mechanism in porous materials under compression: crackling noise in mesoporous SiO2. *Philosophical Magazine Letters* **91(8)** (2011), 554-560.

[184] Schenke, M.: *Parallel Simulation of Volume-coupled Multi-field Problems with Special Application to Soil Dynamics.* Dissertation, Report No. II-32, Institute of Applied Mechanics (CE), University of Stuttgart 2017.

[185] Schlüter, A.; Willenbücher, A.; Kuhn, C. & Müller, R.: Phase field approximation of dynamic brittle fracture. *Computational Mechanics* **54** (2014), 1141-1161.

[186] Scholz. B.: *Application of a Micropolar Model to the Localization Phenomena in Granular Materials: General Model, Sensitivity Analysis and Parameter Optimization.* Dissertation, Report No. II-15, Institute of Applied Mechanics (CE), University of Stuttgart 2007.

[187] Simo, J. C.; Oliver, J. & Armero, F.: An analysis of strong discontinuities induced by strain-softening in rate-independent inelastic solids. *Computational Mechanics* **12** (1993), 277-296.

[188] Sneddon I. N.: The distribution of stress in the neighbourhood of a crack in an elastic solid. *Proceedings of the Royal Society A* **87** (1946), 229-260.

[189] Song, J.-H.; Areias, P. & Belytschko, T.: A method for dynamic crack and shear band propagation with phantom nodes. *International Journal for Numerical Methods in Engineering* **67** (2006), 868893.

[190] Song, J.-H. & Belytschko, T.: Cracking node method for dynamic fracture with finite elements. *International Journal for Numerical Methods in Engineering* **77** (2009), 360385.

[191] Stoer, J. & Bulirsch, R.: *Introduction to Numerical Analysis.* Springer-Verlag, Berlin 2013.

[192] Stumpf, J. & Le, K. C.: Variational principles of nonlinear fracture mechanics. *Acta Mechanica* **83** (1990), 25-37.

[193] Taylor, C. & Hood, P.: A numerical solution of the Navier-Stokes equations using the finite element technique. *Computers and Fluids* **1** (1973), 73-100.

[194] Truesdell, C. A.: Sulle basi della termomeccanica. Rendiconti Lincei **22** (1957), 33-38.

[195] Truesdell, C. A. & Toupin, R. A.: The classical field theories, in: Flügge, S.(Ed.). *Handbuch der Physik* Vol. III/1. Springer-Verlage, Berlin 1960, pp. 226-902.

[196] Truesdell, C. A.: *Rational Thermodynamics.* McGraw-Hill , New York (1969).

[197] Warpinski, N. R. & Teufel, L. W.: Influence of geologic discontinuities on hydraulic fracture propagation. *Journal of Petroleum Technology* **39** (1987), 209-220.

[198] Wagner, A.: *Extended Modelling of the Multiphasic Human Brain Tissue with Application to Drug-Infusion Processes.* Dissertation, Report No. II-27, Institute of Applied Mechanics (CE), University of Stuttgart 2014.

[199] Wheeler, M.; Wick, T. & Wollner, W.: An augmented-Lagrangian method for the phase-field approach for pressurized fractures. *Computer Methods in Applied Mechanics and Engineering* **271** (2014), 69-85.

[200] Whitaker, S.: Flow in porous media: A theoretical derivation of Darcy's law. *Transport in Porous Media* **1** (1986), 3-25.

[201] Woltman, R.: *Beyträge zur Hydraulischen Architektur*, Dritter Band, Dietrich, Göttingen (1794).

[202] Wu, X.-R. & Carlsson, A. J.: *Weight Function and Stress Intensity Factor Solutions.* Pergamon Press, Oxford 1991.

[203] Xu, X. P. & Needleman, A.: Numerical simulations of fast crack growth in brittle solids. *Journal of the Mechanics and Physics of Solids* **42** (1994), 1397-1434.

[204] Yarema, S. Y.: On the contribution of G.R. Irwin to fracture mechanics. *Materials Science* **31** (1996), 617-623.

[205] Zhou, M.; Rosakis, A. J. & Ravichandran, G.: Dynamically propagating shear bands in impact-loaded prenotched plates -I. Experimental investigations of temperature signatures and propagation speed. *Journal of the Mechanics and Physics of Solids* **44** (1996), 981-1006.

[206] Zhou, M.; Rosakis, A. J. & Ravichandran, G.: Dynamically propagating shear bands in impact-loaded prenotched plates -II Numerical simulations. *Journal of the Mechanics and Physics of Solids* **44** (1996), 1007-1032.

[207] Zhou, M.; Rosakis, A. J. & Ravichandran, G.: On the growth of shear bands and failure-mode transition in prenotched plates: A comparison of singly and doubly notched specimens. *International Journal of Plasticity* **14** (1998), 435-451.

[208] Zhou, J.; Chen, M.; Jin, Y. & Zhang, G.-Q.: Analysis of fracture propagation behaviour and fracture geometry using a tri-axial fracturing system in naturally fractured reservoirs. *International Journal of Rock Mechanics and Mining Sciences* **45** (2008), 1143-1152.

[209] Zienkiewicz, O. C.; Chan, A. H. C.; Pastor, M.; Schrefler, B.A. & Shiomi, T.: *Computational geomechanics with special reference to earthquake engineering.* Wiley, Chichester 1999.

[210] Zinatbakhsh, S.: *Coupled Problems in the Mechanics of Multi-Physics and Multi-Phase Materials.* Dissertation, Report No. II-30, Institute of Applied Mechanics (CE), University of Stuttgart 2015.

Curriculum Vitae

Personal Data:

Name:	Chenyi Luo
Date of birth:	January 30, 1987
Place of birth:	Shanghai, China
Nationality:	Chinese
Parents:	Haian Luo & Shenglan Chen
Marital status:	Lin Chen
Children:	Yuanqiao (Sven) Chen

Education:

09/1993 – 01/1995	elementary school "Pangu Road Elementary School"
02/1995 – 08/1999	elementary school "No.3 Elementary School of Baolin Road"
09/1999-08/2002	middle school "Songyi Middle School"
09/2002 – 08/2005	middle school "Shanghai Wusong Middle School"
09/2005-08/2009	studies in civil engineering at the 'Tongji University" degree: Bachelor of Engineering
09/2010-10/2012	studies in "Computational Mechanics of Materials and Structures (COMMAS)" (*Honor Roll Student, Rank 1*) degree: Master of Science

Professional Occupation:

05/2012 –10/2012	Intern at Hilti AG, in Schaan, Liechtenstein
08/2013 –	assistant lecturer at the Institute of applied Mechanics (Civil Engineering) at the Universität Stuttgart, Germany

Released Report Series

II-1   Gernot Eipper: *Theorie und Numerik finiter elastischer Deformationen in fluid-gesättigten porösen Festkörpern*, 1998.

II-2   Wolfram Volk: *Untersuchung des Lokalisierungsverhaltens mikropolarer poröser Medien mit Hilfe der Cosserat-Theorie*, 1999.

II-3   Peter Ellsiepen: *Zeit- und ortsadaptive Verfahren angewandt auf Mehrphasenprobleme poröser Medien*, 1999.

II-4   Stefan Diebels: *Mikropolare Zweiphasenmodelle: Formulierung auf der Basis der Theorie Poröser Medien*, 2000.

II-5   Dirk Mahnkopf: *Lokalisierung fluidgesättigter poröser Festkörper bei finiten elasto-plastischen Deformationen*, 2000.

II-6   Heiner Müllerschön: *Spannungs-Verformungsverhalten granularer Materialien am Beispiel von Berliner Sand*, 2000.

II-7   Stefan Diebels (Ed.): *Zur Beschreibung komplexen Materialverhaltens: Beiträge anläßlich des 50. Geburtstages von Herrn Prof. Dr.-Ing. Wolfgang Ehlers*, 2001.

II-8   Jack Widjajakusuma: *Quantitative Prediction of Effective Material Parameters of Heterogeneous Materials*, 2002.

II-9   Alexander Droste: *Beschreibung und Anwendung eines elastisch-plastischen Materialmodells mit Schädigung für hochporöse Metallschäume*, 2002.

II-10   Peter Blome: *Ein Mehrphasen-Stoffmodell für Böden mit Übergang auf Interface-Gesetze*, 2003.

II-11   Martin Ammann: *Parallel Finite Element Simulations of Localization Phenomena in Porous Media*, 2005.

II-12   Bernd Markert: *Porous Media Viscoelasticity with Application to Polymeric Foams*, 2005.

II-13   Saeed Reza Ghadiani: *A Multiphasic Continuum Mechanical Model for Design Investigations of an Effusion-Cooled Rocket Thrust Chamber*, 2005.

II-14   Wolfgang Ehlers & Bernd Markert (Eds.): *Proceedings of the 1st GAMM Seminar on Continuum Biomechanics*, 2005.

II-15   Bernd Scholz: *Application of a Micropolar Model to the Localization Phenomena in Granular Materials: General Model, Sensitivity Analysis and Parameter Optimization*, 2007.

II-16 Wolfgang Ehlers & Nils Karajan (Eds.): *Proceedings of the 2nd GAMM Seminar on Continuum Biomechanics*, 2007.

II-17 Tobias Graf: *Multiphasic Flow Processes in Deformable Porous Media under Consideration of Fluid Phase Transitions*, 2008.

II-18 Ayhan Acartürk: *Simulation of Charged Hydrated Porous Materials*, 2009.

II-19 Nils Karajan: *An Extended Biphasic Description of the Inhomogeneous and Anisotropic Intervertebral Disc*, 2009.

II-20 Bernd Markert: *Weak or Strong - On Coupled Problems In Continuum Mechanics*, 2010.

II-21 Wolfgang Ehlers & Bernd Markert (Eds.): *Proceedings of the 3rd GAMM Seminar on Continuum Biomechanics*, 2012.

II-22 Wolfgang Ehlers: *Poröse Medien – ein kontinuumsmechanisches Modell auf der Basis der Mischungstheorie*, 2012.

II-23 Hans-Uwe Rempler: *Damage in Multi-phasic Materials Computed with the Extended Finite-Element Method*, 2012.

II-24 Irina Komarova: *Carbon-Dioxide Storage in the Subsurface: A Fully Coupled Analysis of Transport Phenomena and Solid Deformation*, 2012.

II-25 Yousef Heider: *Saturated Porous Media Dynamics with Application to Earthquake Engineering*, 2012.

II-26 Okan Avci: *Coupled Deformation and Flow Processes of Partial Saturated Soil: Experiments, Model Validation and Numerical Investigations*, 2013.

II-27 Arndt Wagner: *Extended Modelling of the Multiphasic Human Brain Tissue with Application to Drug-Infusion Processes*, 2014.

II-28 Joffrey Mabuma: *Multi-Field Modelling and Simulation of the Human Hip Joint*, 2014.

II-29 Robert Krause: *Growth, Modelling and Remodelling of Biological Tissue*, 2014.

II-30 Seyedmohammad Zinatbakhsh: *Coupled Problems in the Mechanics of Multi-Physics and Multi-Phase Materials*, 2015.

II-31 David Koch: *Thermomechanical Modelling of Non-isothermal Porous Materials with Application to Enhanced Geothermal Systems*, 2016.

II-32 Maik Schenke: *Parallel Simulation of Volume-coupled Multi-field Problems with Special Application to Soil Dynamics*, 2017.

II-33 Steffen Mauthe: *Variational Multiphysics Modeling of Diffusion in Elastic Solids and Hydraulic Fracturing in Porous Media*, 2017.

II-34 Kai Häberle: *Fluid-Phase Transitions in a Multiphasic Model of CO_2 Sequestration into Deep Aquifers: A fully coupled analysis of transport phenomena and solid deformation*, 2017.